Development of a Variable-Bandwidth Laser Interferometer Gravitatinal Wave Detector

Osamu Miyakawa

THESIS

Department of Physics, Faculty of Science
University of Tokyo

December 2001

Contents

Chapter 1

Introduction

1.1 Gravitational wave detection

In 1916, A.Einstein predicted that space-time ripples that propagate as waves at the speed of light exist as a consequence of the general theory of relativity [1, 2, 3, 4]. These were called 'gravitational waves', but their existence was only theoretical for a long time.

The existence of gravitational waves was confirmed indirectly by J.H.Taylor et al. as a result of the observation of the binary pulsar PSR 1913+16 [5, 6, 7]. They won the Nobel prize for this achievement in 1993. However, gravitational waves have not been detected directly because the interaction between gravitational waves and matters is very small.

The direct detection of gravitational waves would not only verify the general theory of relativity but would also provide a mechanism for studying the structure of neutron stars, Hubble's constant, etc.; The benefits would be invaluable. Direct detection of gravitational waves can bring information from the space, which can not be obtained by conventional astronomy using electromagnetic waves. It has a possibility of establishing a new field — gravitational wave astronomy.

1.2 Interferometers as gravitational wave detectors

With this motivation, and with recent technological progress, international efforts to direct detect of gravitational waves using large-scale laser interferometers have increased. Today huge laser interferometer gravitational wave antennas with arm

length from 300 m to 4 km in various countries around the world are operating or under construction: the 'LIGO' project of the United States, which consists of two 4 km interferometers and a 2km interferometer [8], the 'VIRGO' project, a 3 km interferometer that France and Italy are building jointly [9], the 'GEO600' project with an arm length of 600 m by Germany and the United Kingdom [10], and the 'TAMA' project by Japan, which started in 1995 [11].

TAMA300, which was constructed by the TAMA project, has achieved the worlds-best sensitivity. The best sensitivity was achieved in summer of 2000 [12], and an observation run of 1000 hours was accomplished in 2001. The LIGO group succeeded in the operation of their 2 km interferometer in its full optical configuration. With two or more interferometers being operated simultaneously around the world within several years there is a possibility that gravitational waves could be detected very soon. However, it is necessary to improve the sensitivity of the detectors further in order to improve the detection frequency of gravitational waves, and thus to establish the field of gravitational wave astronomy in the future.

1.3 Development of optical configurations of interferometers

Let us review the historical development of the optical design of an interferometer for gravitational wave detection. The original idea was to use a Michelson interferometer to measure the distortion of space by measuring the distance between two mirrors when each mirror is considered as a free mass [13, 14]. Because the precision of the space distortion measurement using the interferometer is relative, precision improves when the interferometer has a longer base line. For gravitational waves at 100 Hz, the optimal arm length is 750 km, but it isn't realistic to construct such a large interferometer on ground.

Two methods have been invented to increase the effective arm length: a 'delay line (DL)' and a 'Fabry-Perot (FP)' cavity. The DL folds the light path many times [15], it has been proposed [16, 17] and successfully tested [18]. The FP resonates light between two parallel mirrors [19, 20]. Because the DL method has problems from scattered light, the FP has been selected as a standard method.

After that, so-called 'power recycling' was proposed to improve the sensitivity of the interferometers. This is a technique to increase the effective light power by

reflecting the light returning from the interferometer to the light source back to the interferometer [19, 20]. Since the shot noise of an interferometer is reduced as the inverse square root of the laser power, power recycling can improve the shot noise sensitivity. This method was explored by some table top experiments [22, 23, 24, 25, 26] and prototype experiments [27, 28, 29], and most projects including TAMA have adopted this method [8, 9, 11]. The LIGO group has already succeeded in operating a power recycled interferometer.

However, even if it is assumed that gravitational waves can be detected by the power recycled interferometer, it is necessary to improve the detection frequency to establish the gravitational wave astronomy. A possible solution being considered is a variable band-width gravitational wave detector which realizes higher sensitivity in a certain frequency band. This is a technology which processes gravitational wave signals by an additional mirror placed at the signal detection port. Historically, a 'signal recycling (SR)' method to recycle gravitational wave signals in an interferometer was proposed first [30], and then 'Resonant Sideband Extraction (RSE)' method was later proposed [31, 32]. With RSE the signal is extracted from the FP cavity before it can become dephased.

This study aims at the development of an RSE interferometer having excellent features such as immunity to thermal distortion from a high power laser [33, 34, 35]. The principle of RSE was confirmed by G.Heinzel [36], and has been explored in several other experiments around the world [37, 38]. In these experiments the control method of the interferometer was not optimized, so the prospect of incorporating RSE in a large-scale interferometer was not fully established. However, Resonant Sideband Extraction is a technology sure to be required in future gravitational wave detection such as the LCGT [39] or the Advanced LIGO [40], and fundamental research to realize the installation in a large-scale interferometer is very important.

1.4 Overview of this thesis

By this study, we aim to develop a control scheme for the RSE interferometer. We use a single modulation method to extract the control signal of RSE, whereas other experiments use two or more modulations. The multi modulation scheme suffers from problems transmitting the modulation sidebands through a mode cleaner. For installation in an actual interferometer, a configuration that can be controlled with

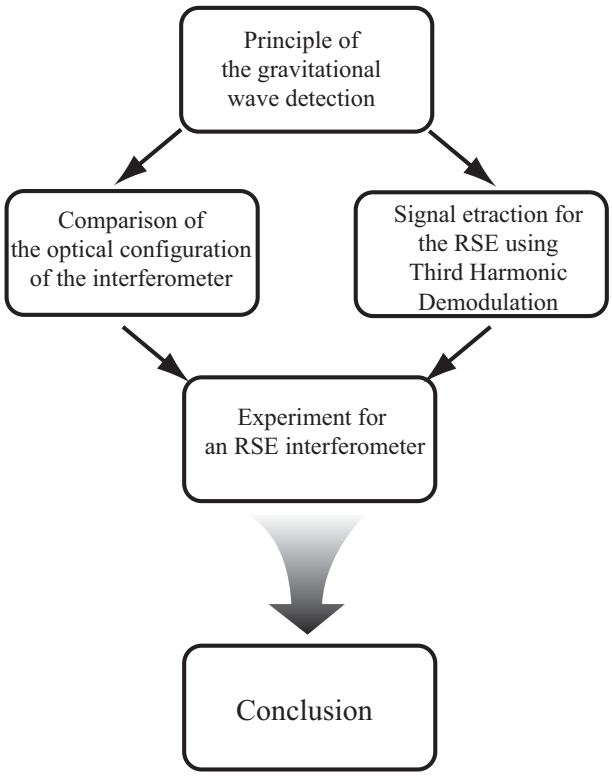

Figure 1.1: Structure of this thesis.

only a single modulation is overwhelmingly advantageous. However, as expected, extracting a control signal with only a single modulation frequency is very difficult. We overcome this by applying Third Harmonic Demodulation (THD) to the control of the Resonant Sideband Extraction.

We constructed an interferometer which has mirrors suspended as pendulums in a vacuum chamber in order to make the experiment situation as close as possible to think of the real detectors. Other groups performed experiments with fixed mirrors in the air [37, 38].

Fig. 1.1 shows the structure of this thesis. At first, in chapter 2, we describe the mechanism of gravitational wave generation and the principles of gravitational wave detection. Then, in chapter 3, the shot noise sensitivity with various optical configurations is discussed, with the result that the Resonant Sideband Extraction is an advantageous configuration. In chapter 4, we describe the signal extraction method using THD for the RSE interferometer. The experimental results will be shown in chapter 5. Finally in chapter 6, conclusions will be presented.

Chapter 2

Detection of Gravitational waves

2.1 Gravitational waves

2.1.1 The Einstein equation

According to Einstein's general theory of relativity [1, 2, 3, 4], local distance ds between different two points of x^μ and $x^\mu + dx^\mu$[1] in four-dimensional space-time is given by

$$ds^2 = g_{\mu\nu} dx^\mu dx^\nu, \tag{2.1}$$

where $g_{\mu\nu}$ is the metric tensor. $g_{\mu\nu}$ is determined by the Einstein equation.

The Einstein equation to express the interaction between the gravity and mass is expressed by

$$G_{\mu\nu} = \frac{8\pi G}{c^4} T_{\mu\nu} \tag{2.2}$$

with Einstein tensor $G_{\mu\nu}$ and energy-momentum tensor $T_{\mu\nu}$. Here, c is the speed of light, and G is the gravitational constant. The Einstein tensor $G_{\mu\nu}$ is defined by

$$G_{\mu\nu} \equiv R_{\mu\nu} - \frac{1}{2} g_{\mu\nu} R, \tag{2.3}$$

where $R_{\mu\nu}$ is defined by

$$R_{\mu\nu} \equiv \Gamma^\alpha{}_{\mu\nu,\alpha} - \Gamma^\alpha{}_{\mu\alpha,\nu} + \Gamma^\beta{}_{\mu\nu}\Gamma^\gamma{}_{\beta\gamma} - \Gamma^\beta{}_{\mu\gamma}\Gamma^\gamma{}_{\nu\beta}, \tag{2.4}$$

$$\Gamma^\mu{}_{\nu\lambda} \equiv \frac{1}{2} g^{\mu\alpha} \left(g_{\alpha\nu,\lambda} + g_{\alpha\lambda,\nu} - g_{\nu\lambda,\alpha} \right). \tag{2.5}$$

$R_{\mu\nu}$ is called the Ricci tensor, and $\Gamma^\mu{}_{\nu\lambda}$, which is called the Christoffel symbol. R and $R_{\mu\nu}$ have a relation:

$$R \equiv g^{\mu\nu} R_{\mu\nu}. \tag{2.6}$$

[1] $x^\mu = (ct, x, y, z)$

R is called the Ricci scalar.

2.1.2 Linear approximation of the Einstein equation

In a flat space-time without gravity called the Minkowski space, the metric tensor is expressed by

$$g_{\mu\nu} = \begin{pmatrix} -1 & 0 & 0 & 0 \\ 0 & 1 & 0 & 0 \\ 0 & 0 & 1 & 0 \\ 0 & 0 & 0 & 1 \end{pmatrix} \tag{2.7}$$

$$\equiv \eta_{\mu\nu}. \tag{2.8}$$

Because the four-dimensional space-time is perturbated from the Minkowski space, when a case of a weak gravitational field is present, the metric tensor can be expressed by the flat space-time metric $\eta_{\mu\nu}$ and the perturbation $h_{\mu\nu}$ from it as follows:

$$g_{\mu\nu} = \eta_{\mu\nu} + h_{\mu\nu}, \tag{2.9}$$

To the first order of $h_{\mu\nu}$, the Eq. (2.5), (2.4), (2.6), (2.3) are given as

$$\Gamma^{\mu}{}_{\nu\lambda} = \frac{1}{2}\eta^{\mu\alpha}\left(h_{\alpha\nu,\lambda} + h_{\alpha\lambda,\nu} - h_{\nu\lambda,\alpha}\right), \tag{2.10}$$

$$R_{\mu\nu} = \frac{1}{2}\left(h_{\alpha\nu}{}^{,\alpha}{}_{,\mu} + h_{\alpha\mu}{}^{,\alpha}{}_{,\nu} - h_{\mu\nu}{}^{,\alpha}{}_{,\alpha} - h_{,\mu\nu}\right), \tag{2.11}$$

$$R = h_{\mu\nu}{}^{,\mu\nu}, \tag{2.12}$$

$$G_{\mu\nu} = \frac{1}{2}h_{\alpha\nu}{}^{,\alpha}{}_{,\mu}\left[+h_{\alpha\mu}{}^{,\alpha}{}_{,\nu} - h_{\mu\nu}{}^{,\alpha}{}_{,\alpha} - h_{,\mu\nu} + \eta_{\mu\nu}\left(h_{\alpha\lambda}{}^{,\alpha\lambda} - h^{,\alpha}{}_{,\alpha}\right)\right], \tag{2.13}$$

where h is the trace of $h_{\mu\nu}$:

$$h \equiv \eta^{\mu\nu}h_{\mu\nu}. \tag{2.14}$$

When the tensor

$$\bar{h} \equiv h_{\mu\nu} - \frac{1}{2}\eta_{\mu\nu}h \tag{2.15}$$

and Eq. (2.2), (2.3) and (2.10)$\sim$(2.13), the Einstein equation can be simplified to

$$\frac{1}{2}\left[\bar{h}_{\alpha\nu}{}^{,\alpha}{}_{,\mu} + \bar{h}_{\alpha\mu}{}^{,\alpha}{}_{,\nu} - \bar{h}_{\mu\nu}{}^{,\alpha}{}_{,\alpha} - h_{,\mu\nu} + \eta_{\mu\nu}\bar{h}_{\alpha\lambda}{}^{,\alpha\lambda}\bar{h}\right] = \frac{8\pi G}{c^4}T_{\mu\nu}. \tag{2.16}$$

When the Lorentz gauge condition

$$\bar{h}^{\mu\nu}{}_{,\nu} = 0 \tag{2.17}$$

is used as a gauge condition, we can obtain a linearized Einstein equation as

$$-\frac{1}{2}\bar{h}_{\mu\nu}{}^{,\alpha}{}_{,\alpha} = \frac{8\pi G}{c^4}T_{\mu\nu}. \tag{2.18}$$

2.1.3 The wave equation

In particular, the vacuum state can be expressed in the Eq. (2.18) as

$$T_{\mu\nu} = 0, \tag{2.19}$$

so the Einstein equation can be given as a wave equation of three dimensions as

$$\Box \bar{h}_{\mu\nu} = 0 \ \ (\Box = -\frac{\partial^2}{c^2 \partial t^2} + \triangle). \tag{2.20}$$

Eq. (2.20) indicates that the perturbations of the Minkowski space propagate at the speed of light. The solutions of this equation are referred to gravitational waves.

2.1.4 Propagation of gravitational waves

We consider a plane wave as the solution of Eq. (2.20) as

$$\bar{h}_{\mu\nu} = A_{\mu\nu} exp\left(ik_\alpha x^\alpha\right). \tag{2.21}$$

If Eq. (2.21) satisfies Eq. (2.17) (2.20), the conditions

$$A^{\mu\alpha} k_\alpha \ = \ 0 \tag{2.22}$$

and

$$k_\alpha k^\alpha \ = \ 0 \tag{2.23}$$

must be imposed on k_α. Eq. (2.22) shows that gravitational waves are transverse waves, and Eq. (2.23) shows that they travel at the speed of light just like electromagnetic waves.

2.1.5 Degree of freedom of gravitational waves

Because the condition of Lorenz gauge of Eq. (2.17) does not uniquely determine the gauge, arbitrariness still remains in the choice of the coordinates. Here, the condition of

$$A_{\alpha\beta} U^\beta \ = \ 0 \tag{2.24}$$

$$A^\alpha_\alpha \ = \ 0 \tag{2.25}$$

is imposed further. U^β is a time unit vector which can be arbitrarily chosen. Eq. (2.22) (2.24), and (2.25) are called Transverse Traceless gauge — TT gauge —.

Eq. (2.22) and (2.24) indicate that there must be a coordinate system where gravitational waves can be observed as transverse waves in a local Lorentz frame when it is seen from an arbitrary observer. On the other hand, Eq. (2.25) indicates that trace of $\bar{h}_{\mu\nu}$ is 0 (traceless) as follows

$$\bar{h}^{TT}\alpha_{\alpha}{}^{\mu} = h^{T}T\alpha_{\alpha}{}^{\mu} = 0. \tag{2.26}$$

Here, Lorentz frame which is constant time unit vector U_{μ} as

$$U^{\mu} = \delta^{\mu}{}_{0} \tag{2.27}$$

is taken for the Minkowski space of the background, and the direction which the gravity wave propagates is taken as z axis, then

$$\bar{h}_{\mu\nu} = A_{\mu\nu}\mathrm{e}^{ik(ct-z)} \tag{2.28}$$

$$A_{\mu\nu} = \begin{pmatrix} 0 & 0 & 0 & 0 \\ 0 & h_{+} & h_{\times} & 0 \\ 0 & h_{\times} & -h_{+} & 0 \\ 0 & 0 & 0 & 0 \end{pmatrix}, \tag{2.29}$$

where h_{+} and $h_{\times}$ are arbitrary functions of $t - z$ and they are expressed from this equation as

$$h_{+} = A_{+}\exp[i\omega(t-z)] \tag{2.30}$$

$$h_{\times} = A_{\times}\exp[i\omega(t-z)]. \tag{2.31}$$

Thus, gravitational waves are transverse waves and have two polarizations.

2.1.6 Effect of gravitational waves on particles

Motion of a free particle which does not receive any force except from gravity is determined by a geodesic equation as follows:

$$\frac{\mathrm{d}}{\mathrm{d}\tau}U_{\alpha} + \Gamma^{\alpha}{}_{\mu\nu}U^{\mu}U^{\nu} = 0, \tag{2.32}$$

where U^{α} is the four velocity of the particle, and τ is the proper time. We consider the Lorenz frame where the particle is stationary first, and the TT gauge is considered for this frame. Then, the acceleration to the particle is

$$\begin{aligned} \left(\frac{\mathrm{d}U^{\alpha}}{\mathrm{d}\tau}\right)_{0} &= -\Gamma^{\alpha}{}_{00} \\ &= -\frac{1}{2}\eta^{\alpha\beta}\left(h_{\beta 0,0} + h_{0\beta,0} - h_{00,\beta}\right) \\ &= 0. \end{aligned} \tag{2.33}$$

Because the particle does not accelerate, the effect of the gravitational wave is not shown in the appearance.

In order to see the effect of gravitational waves, a proper distance between two near particles must be investigated. Coordinates on the TT gauge of two free particles are taken with $(0,0,0)$ and $(\epsilon,0,0)$, where $\epsilon \ll 1$. When gravitational waves exist, the coordinate values are kept unchanged from Eq. (2.33), but the proper distance Δl between two particles is changed to

$$\begin{aligned} \Delta l &\equiv \int |\mathrm{d}s^2|^{\frac{1}{2}} = \int |g_{\mu\nu} dx^\mu dx^\nu|^{\frac{1}{2}} \\ &= \int_0^\epsilon |g_{xx}|^{\frac{1}{2}} \mathrm{d}x \simeq |g_{xx}(x=0)|^{\frac{1}{2}} \epsilon \\ &\simeq \left[1 + \frac{1}{2} h^{TT}{}_{xx}(x=0)\right] \epsilon. \end{aligned} \tag{2.34}$$

From Eq. (2.32), the equation of geodesic deviation is derived as

$$\frac{\mathrm{d}^2}{\mathrm{d}\tau} \xi^i = R^i{}_{\alpha\beta j} U^\alpha U^\alpha \xi^j. \tag{2.35}$$

When the first order of $h^{TT}{}_{\mu\nu}$ is considered, the approximation of

$$U^\alpha \simeq (1,0,0,0) \tag{2.36}$$

$$\tau \simeq ct \tag{2.37}$$

can be taken. Therefore Eq. (2.35) is rewritten as

$$\frac{1}{c^2} \frac{\partial^2}{\partial t^2} \xi^i = -R^i{}_{0j0} \xi^j. \tag{2.38}$$

In addition, because

$$R^i{}_{0j0} = -\frac{1}{2c^2} \frac{\partial^2 h^{TT\,i}{}_j}{\partial t^2} \tag{2.39}$$

holds in the TT gauge, Eq. (2.38) is described as

$$\frac{\partial^2}{\partial t^2} \xi^i = \frac{1}{2} \frac{\partial^2 h^{TT\,i}{}_j}{\partial t^2} \xi^j. \tag{2.40}$$

This indicates that gravitational waves act on particles of mass m like an external force of

$$m \frac{\partial^2}{\partial t^2} \xi^i = \frac{m}{2} \frac{\partial^2 h^{TT\,i}{}_j}{\partial t^2} \xi^j. \tag{2.41}$$

Fig. 2.1 shows the motion of the particles under this condition. The gravitational wave has two modes, + (plus) and $\times$ (cross), they are inclined to each other by 45 degrees.

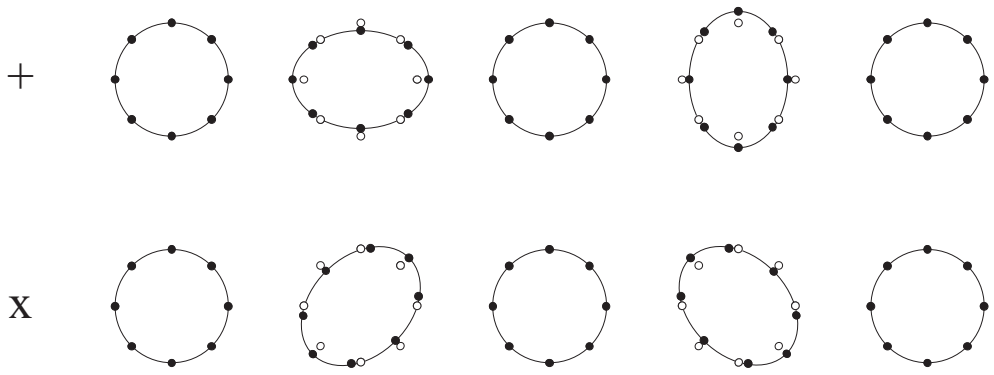

Figure 2.1: Displacement of particles when gravitational waves with a polarization of +mode(upper) and ×mode(lower) exist.

2.2 Sources

Semi-periodic sources such as inspirals of binary neutron stars and burst sources such as supernova explosions are regarded as the main sources of gravitational waves [4].

The binary neutron stars (BNS) radiate gravitational waves by their orbital motion as they approach each other losing energy, and finally coalesce. It is predicted that this process produces strong gravitational waves. The wave form is calculated well from the measured mass and orbital parameters, so the BNS is considered a main target of the detection using interferometers.

Additionally, it is thought that a strong burst of gravitational waves is generated when a supernova (SN) explodes. However, the waveform is not predicted because the collapse process is not well understood.

In recent years the possibility of gravitational waves produced by the black hole-black hole binaries (black hole MACHO) has been proposed by Nakamura [41]. If these exist, it is shown that the gravitational wave from the MACHO black hole coalescence can be detected by TAMA with the current sensitivity once every 20 years.

2.3 Resonant bar detectors

The history of the gravitational wave detection dates back to Joseph Weber in the 1960's [42, 43]. Originally the name "resonant mass type gravitational wave detector" comes from that a detector is excited by the oscillation of the gravitational wave

Source	Frequency	Amplitude(h)	Ratio
BNS coalescence (200 Mpc)	10 Hz$\sim$1 kHz	10^{-22}	$\sim$ several/year
SN explosion (our galaxy)	$\sim$ 1 kHz	10^{-18}	1/hundred years
SN explosion (Virgo cluster)	$\sim$ 1 kHz	10^{-21}	several/year
MACHO	$\sim$ 500 Hz	10^{-18}	1/ten years
Black hole generation	$\sim$ 1mHz	10^{-17}	1/year
Pulsar	10Hz $\sim$ 1kHz	10^{-25}	continuous
Space string	10^{-7}Hz	10^{-15}	back ground

Table 2.1: Sources of gravitational waves

at the resonant frequency of the elastic body. Detection of gravitational waves is realized by measuring displacement of the expansion and contraction at the resonant frequency.

Weber's detector used the elastic resonance of a column of aluminum 66 cm in diameter, 1.5 m in length, and 1.4tons in weight at room temperature. Weber once announced that he succeeded in the direct measurement of a gravitational wave, but today, by later verification, what Weber observed is thought to be noise. The strain sensitivity at that time was about $h = 6 \times 10^{-17}$.

Various improvement were later added to the detector. The second generation detectors, cooled to liquid helium temperature, include EXPLORER of CERN [44] and ALLEGRO of LSU (Louisiana State University) [45]. The third generation detectors which use a dilution freezing container to lower the temperature to dozens of mK now operating include AURIGA of Frascati [46] and NAUTILUS of INFN [47]. Moreover, some ball-shaped detectors that have various resonant frequencies, to survey a wide band are being developed: GRAIL of Dutch [48] and TIGA of LSU [49, 50].

2.4 Interferometer for gravitational wave detection

2.4.1 Detection Principles

A Michelson laser interferometer with suspended mirrors is used to detect gravitational waves. As shown in Fig. 2.2, when gravitational waves with an appropriate polarization passes the interferometer vertically, the lengths of the two arms are differentially modulated. It results in changes in the intensity of the interfering light,

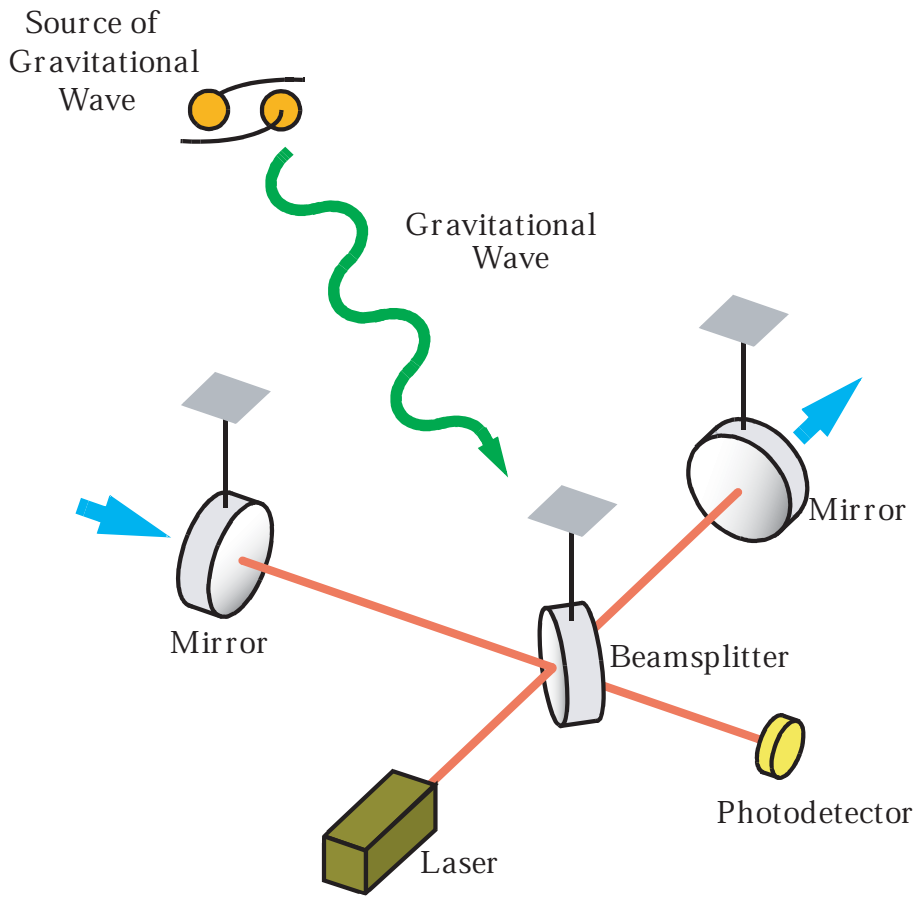

Figure 2.2: Michelson Interferometer with suspended mirrors for detecting gravitational waves

which is detected by a photodetector. In the actual interferometer the intensity of the light at the detector port will be kept dark by controlling the arm length. Therefore the feedback signal to the mirrors should contain gravitational wave signals. The beamsplitter and mirrors should be suspended so that they can free-fall horizontally at frequencies well above their pendulum frequencies.

It should be noted that the length change caused by gravitational waves can be regarded either as the consequence of the force applied to the end mirrors or that of the variation of the apparent speed of light, depending on the coordinate system considered. In the proper reference frame of an observer, where the apparent speed of light is constant, the force is applied to masses by gravitational waves with the amplitude of the force proportional to the mass's coordinate position. Therefore the end mirrors are shaken back and forth by the force, whereas the beamsplitter is

sitting at rest. On the other hand, in the TT coordinate system, where any freely-falling mass with no initial velocity does not change its position, the apparent speed of light is modulated by gravitational waves. As a result the optical path difference, measured by such modulated light, is altered. Naturally, the amount of changes in the intensity of the interfering light does not depend on a coordinate system to be considered. It should be also noted that the proper reference frame is only valid when the size of the interferometer is relatively small; when the arm length is larger, the TT coordinate system should be used.

Laser interferometers are ideally suited for detecting gravitational waves, because the length change caused by gravitational waves can be increased by simply scaling up the arm length. Therefore the larger interferometer will provide better sensitivity to gravitational waves. However, the signal would be cancelled if the arm length is too long. For example if the arm length is equal to a half the wavelength of the gravitational wave to be detected, in the TT coordinate system the light experiences modulation of the apparent speed of light positively for half the time of its stay in the arm and negatively for the rest of the time, resulting in a complete cancellation of the total phase change of the modulated light. It can be derived that the optimum arm length is a quarter of the wavelength of the gravitational wave. For example an arm length of 750km is optimal for the 100Hz gravitational wave.

2.4.2 Noise Sources

Noise sources existing in the interferometer can be classified into two categories: sensor noise and displacement noise. The sensor noise comes in during the sensing process, that includes frequency/intensity/geometrical noise of the light and shot noise. The displacement noise is the result of directly shaken mirrors, such as seismic noise and thermal noise. Among those noise sources, shot noise, seismic noise and thermal noise are regarded as three dominant fundamental noise sources existing in the interferometer, while the other noise sources are considered to be technical noise.

Shot Noise

Shot noise exists because a photon has finite energy. Statistical fluctuations in the photon number in the detection process result in shot noise. In order to reduce the shot noise level, the interferometer should be operated in such a way that the

intensity of the light at the detection port is dark. This is because the fluctuations in the photon number are smaller when the intensity of the light at the photodetector is lower.

In addition to this fringe control, it is desirable to have higher incident laser power to reduce the shot noise level by the following reason. Assuming that the interferometer is controlled with a dark fringe at the detection port, the intensity change at the photodetector caused by gravitational waves is proportional to the incident laser power, while the intensity fluctuations caused by shot noise is proportional to square root of the incident laser power; thus the signal to shot noise ratio is improved by square root of the incident laser power. However, note that radiation pressure noise caused by quantum fluctuations of the intensity of the light hitting the mirrors could exceed the sensing shot noise effect if the laser power is too high.

Seismic Noise

Seismic noise can be reduced by isolating the mirrors from the ground motion. Suspending the mirrors to make the freely falling masses also plays a role of isolating the mirrors from the ground motion. The isolation factor increases as the inverse square of the frequency above the pendulum frequency of the suspension system. More isolation can be obtained by using a multi-stage pendulum. It should be emphasized that the vertical isolation is crucial, especially when the multi-stage pendulum is used. The pendulum is, in principle, only effective for isolation of the horizontal motion. The vertical motion of the mirrors, which is not strongly isolated by the pendulum system, could be turned into length change of the arm cavity, coupling with the deviation of the beam axis from the local horizontal line or mechanical cross-coupling from the vertical motion to the horizontal motion.

In addition to the isolation by pendulum, stacks consisting of several metal plates and elastomers on which the suspension system is placed are often used. The stack system is easy to use and has a stable performance, although it is difficult to have a significant isolation below 10Hz.

Thermal Noise

No mass can be exempted from Brownian motion. According to thermodynamics, any mode of a system immersed in another system with a finite temperature is given energy determined by the temperature of the outer system as a result of the energy

exchange between the two systems. There are two important modes relevant to the suspended mirrors: the pendulum mode and internal mode. The pendulum frequency is usually much lower than the interesting frequency range of gravitational waves, and the internal mode resonant frequencies are much higher. In any cases, thermal noise at the relevant frequencies can be reduced by making the quality factor of the modes higher. Since a mode with a higher quality factor has more energy concentrated around the resonances, lower thermal motion is present off the resonant frequencies. This is because the root-mean-square thermal motion integrated over the frequency should be constant. Therefore our endeavor to reduce thermal noise is usually focused on increasing of the quality factor of the suspended mirrors. It can be realized by reducing any mechanical losses involved in the system.

2.5 Current status

2.5.1 TAMA300

TAMA is a Japanese project to construct and operate an interferometric gravitational-wave detector on the Mitaka campus of the National Astronomical Observatory in Tokyo (3540N, 13932E) [11]. The aim of this project is to develop techniques necessary for future large-scale interferometers and, moreover, to detect gravitational waves generated within our local group of galaxies. The target strain sensitivity of TAMA is $hrms = 3 \times 10^{21}$ at 300 Hz with a bandwidth of 300 Hz, which corresponds to $h = 2 \times 10^{-22}1/\mathrm{Hz}$ in linear power spectrum density.

With this sensitivity, the TAMA detector would be able to detect gravitational waves from supernova explosions, and coalescence of compact binary systems within our local group of galaxies. Fig. 2.3 shows the target sensitivities of the TAMA300 interferometer, achieved noise curves, and the expected gravitational-wave sources. In the first observation phase (Phase I), the TAMA interferometer is operated without power recycling, with a sensitivity of $h = 2 \times 10^{-21}1/\mathrm{Hz}$. The final sensitivity of $h = 2 \times 10^{-22}1/\mathrm{Hz}$ will be achieved in the second observation phase (Phase II) with the power recycling and other improvements.

Data taking 6

In the summer of 2001 (August 1 to September 20), a 50-day data-taking run called DT6 was carried out. The objective of this run was to collect 1000 hours of obser-

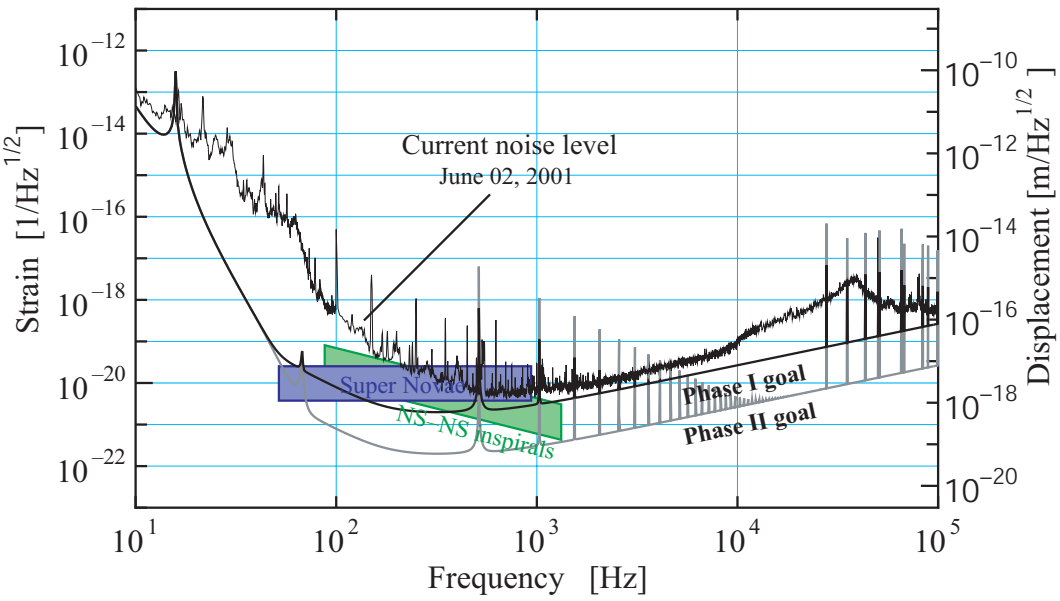

Figure 2.3: Sensitivity curves of the TAMA300 interferometer in units of $1/\sqrt{Hz}$ (left vertical axis) and $m/\sqrt{Hz}$ (right one). The target sensitivities in Phase I and Phase II, the achieved sensitivity curves, and the expected gravitational wave sources (in our galaxy) are shown together.

vation data. Most of the TAMA collaborators participated in this run: 65 people in shifts and several support staffs. Fig. 2.4 is the operation summary during DT6. The detector was operated stably most of the time except when there was some trouble with the laser source and excitations by constructions and typhoons. In DT6, the interferometer was operated for 1107 hours. Rejecting the data during the interferometer adjustment, we collected 1038 hours of observation data; the target observation data length was achieved. The averaged continuous-locking time was about 3.3 hours. Loads to shift members were much reduced in DT6 compared with previous data-taking runs. The interferometer was re-locked automatically in a few minutes. Though most of the control loops are made up of analog circuits in TAMA, these switches and servo gains are controlled by a digital system. In addition to this automatic relock system, a detector monitor system was upgraded in DT6. The collected data by HDAQ, MDAQ, and EPICS systems were processed immediately and sent to the monitor room via networks. Shift members checked detector status (detector noise level, control feedback signals, seismic level, etc.) at a monitor room. If necessary, they entered the center room of the interferometer to make adjustments.

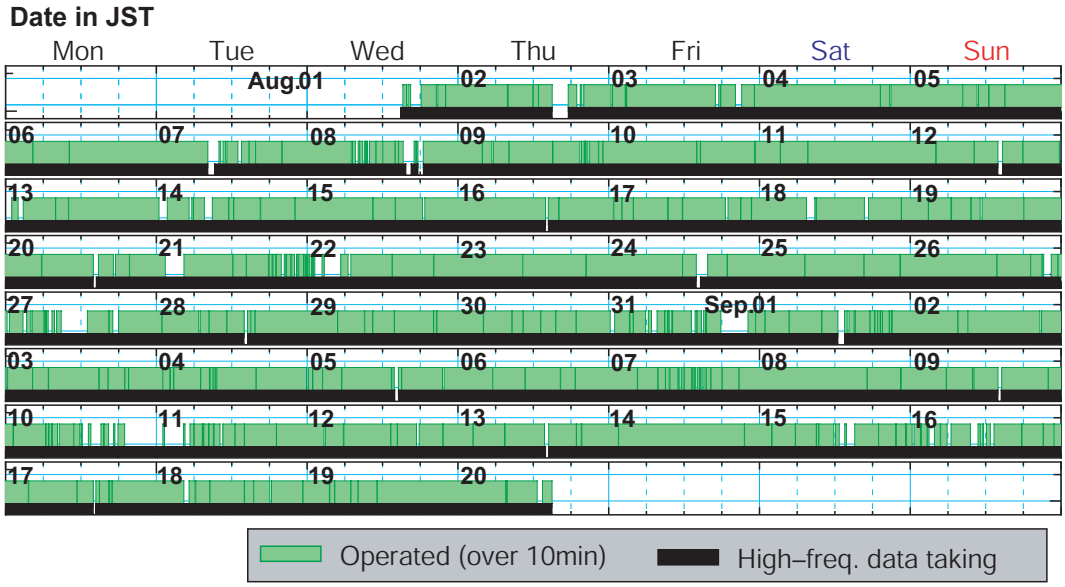

Figure 2.4: Observation summary of data taking 6 (DT6). The interferometer was operated for 1107 hours in 1200 hour data run (92.3% duty circle). The averaged continuous locking time was about 3.3 hours.

Adjustments were required every several hours in typical cases.

The TAMA300 interferometer was operated stably for over 24 hours without loss of lock in the best case (3.3 hours in average). The noise-equivalent sensitivity is $h = 5 \times 10^{-21} 1/\mathrm{Hz}$ at the floor level. With this sensitivity and stability, TAMA has the ability to detect GW events within our galaxy, though such events are expected to be very rare. In order to increase the detection probability for GW events farther away from our galaxy, we are improving the detector sensitivity and stability further. Almost all of the noise sources which limit the detector sensitivity have been identified, and will be reduced. In the data taking 4, we collected about 160 hours of data, which have been analyzed few several points of view. In addition, we have just finished data taking 6, collecting 1038 hours of data. After DT6, we are going to the next step of Phase II, by installing a power-recycling mirror by the end of 2001.

2.5.2 LCGT

Even if TAMA achieves its final goal sensitivity, the detection rate of GW events would be extraordinarily small. Therefore, the LCGT project is planned to expand the basis of TAMA to a large scale interferometer using a cryogenic mirror tech-

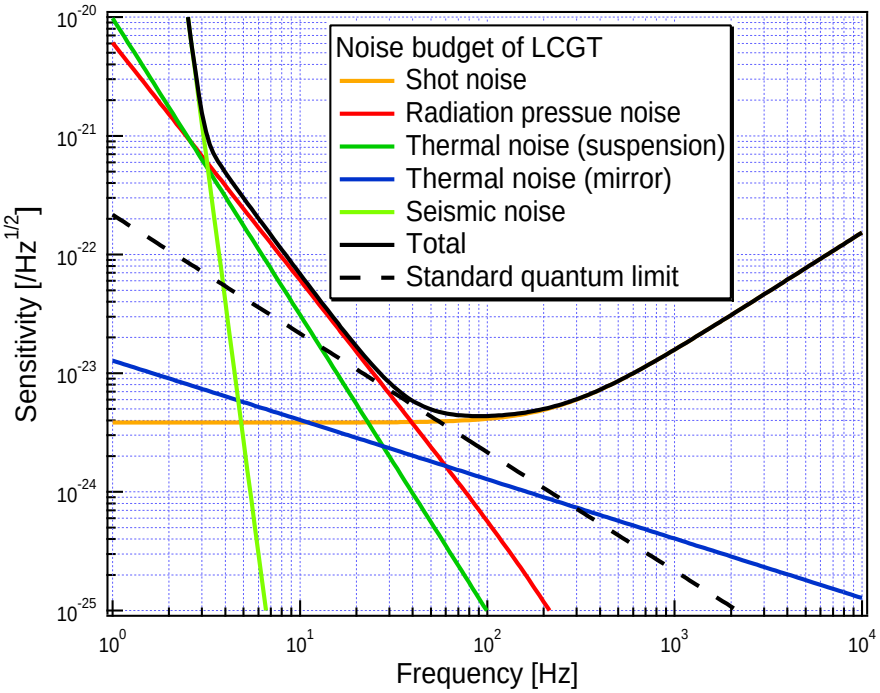

Figure 2.5: Goal sensitivity of LCGT.

nique [39]. LCGT is planned to be built in the Kamioka mine tunnel with 3 km baseline length. It has a design sensitivity better by two orders of magnitude than that of TAMA and the start of the project is expected in 2005 in the earliest case.

The original optical design of LCGT was a power recycled Fabry-Perot-Michelson interferometer with parameters as follows:

- baseline 3 km
- laser power 100 W
- cavity finesse 100
- sapphire mirror 50 kg, $Q = 10^8$, 30 K
- sapphire fiber suspension $Q = 2 \times 10^8$, 10 K
- low frequency attenuator

Expected sensitivity of LCGT is shown in Fig. 2.5. Since the establishment of the above design, technologies have advanced and new techniques have been created.

We will revise the above design to attain the target with less difficulty, less cost, and more reliability. One likely change is the adoption of a broad-band resonant-sideband-extraction scheme. With respect to the LCGT targets, black hole binary events have been discussed because their amplitude is fairly large, which means that low-frequency optimized detectors could see more remote galaxies than those optimized for nominal neutron star binaries.

Various aspects of R&D for LCGT are being investigated and the basic techniques of cryogenic mirrors have already been developed. LCGT is expected to start construction in 2005 in the earliest case .

2.5.3 Other projects in the World

Country	Project	Baseline length	Type	Observation
U.S.A	LIGO	4km	FP (PR)	2002$\sim$
Italy, France	VIRGO	3km	FP (PR)	2002$\sim$
German, U.K.	GEO	600m	DL (DR)	2001$\sim$

Table 2.2: Interferometric detector projects in the World

Table 2.2 shows the projects which are currently constructing laser interferometric gravitational wave detectors. LIGO is an American project to construct two interferometers with a baseline length of 4 km [8]. LIGO is planning coincidence detection and waveform analysis of gravitational waves with these two interferometers. VIRGO is a project by Italy and France [9]. VIRGO aims at detecting low-frequency gravitational waves by adopting a multi-stage seismic isolation system. GEO is a project by Germany and U.K. [10]. The GEO interferometer is a delay-line-Michelson interferometer with dual recycling (power and signal recycling). All these three projects adopt the power recycling technique to increase the effective laser power so as to improve the shot-noise limited sensitivity of the interferometer.

2.5.4 Interferometers with advanced configuration

The present 'first generation' concepts for LIGO, VIRGO and TAMA do not plan to use any mirror in the detection port. Then the signal storage time is given by the length and finesse of the arm cavities and cannot easily be changed. More flexibility

Group	method	mirror	modulation number	detune
Cal-tech	PR+RSE	fixed	2	off-set
Florida	PR+SR	fixed	2	off-set
ANU	PR+RSE	fixed	3	sub-carrier
NAO	RSE	suspended	1	broad band

Table 2.3: Recent small-size experiments of advanced configuration around the world

Group	method	Baseline length	modulation number
Cal-tech	PR+RSE	40m	2
Glasgow	PR+RSE	10m	2

Table 2.4: Plans of prototype interferometer which has an advanced configuration.

can be obtained by placing an additional mirror in the detection port. This configuration is called either 'signal recycling' [30] or 'resonant sideband extraction' [31, 32], depending on the microscopic position ('tuning') of the additional mirror. The effect can either be to increase the signal storage time (as in signal recycling) or decrease it (as in resonant sideband extraction, which is useful only with the existence of arm cavities). In fact these two cases are only the endpoints of a continuum of possible tunings, with the intermediate points called 'detuned'. These detuned cases may also be useful and cannot easily be classified as either 'resonant sideband extraction' or 'signal recycling'.

Resonant sideband extraction is an interesting configuration for interferometers with arm cavities. It allows the use of high-finesse cavities in the arms, with a bandwidth optimized for maximal light energy stored in the arms. The signal storage time, which is then usually too large, can be reduced independently of the carrier storage time.

Resonant sideband extraction was first proposed and demonstrated in a table-top model by the Garching group [36]. It is now seriously considered for large-scale interferometers such as the LCGT [39] and the second generation of the LIGO interferometers [40].

Four small-size experiments including ours have been built around the world for exploring advanced configuration. One is the signal recycling experiment and other three are the Resonant Sideband Extraction experiments [37, 38]. Unlike our experiment the other three experiments use the fixed mirrors in the air and adopt

multi modulations to extract the signal to avoid cross-coupling. Table2.3 shows all small-size experiments currently or recently performed.

Details of the optical configurations are different, but it can be said that the purposes of all the experiments is the same; to confirm the effects of advanced configurations using the conventional frontal modulation. However, there still remains many difficulties in applying these configurations to large-scale interferometers. For example the Multi modulation method has a problem with transmission of the modulation sidebands through the mode cleaner, and the optimal detuning method should be established.

As a process of preparation for a large-scale interferometer, several prototype scale interferometers which have the same configuration as the large-scale interferometer except for its scale are planned, as shown in table 2.4.

2.6 Space-based gravitational wave detectors

Looking further to the future, space-base gravitational wave detectors are essential for the full potential of the gravitational wave astronomy to be realized. Gravity gradient noise will ultimately limit the minimum frequency at which gravitational wave can be measured on Earth. This noise source, however, is inversely proportional to the cube of the distance from Earth and can be significantly reduced by moving the detector into space. A space antenna called LISA [51] will consist of three spacecrafts, each separated by 5×10^6 km, orbiting around the sun. LISA will allow measurement of gravitational waves in the frequency band of 0.1mHz to 0.1Hz. Operating in the low frequency band, LISA's sensitivity will be complementary to the ground-based detectors. LISA promises to provide a signal-to-noise ratio of up to 10^3 for events such as a coalescence of massive black hole binaries, which will be visible for many months before coalescence. The LISA project is currently being studied by both ESA and NASA with a view toward a collaborative mission around 2010.

Chapter 3

Optical configurations of interferometers

In this chapter, we compare various optical configurations of an interferometer. We consider the following configurations from the point of view of shot noise.

1. Fabry-Perot Michelson interferometer (FPMI) as the baseline of a gravitational wave detector.
2. Power Recycled FPMI (PRFPMI) which enhances the effective laser power by reflecting the unused light back to the interferometer.
3. Signal Recycling (SR) which reflects the gravitational wave signals back to the interferometer.
4. Resonant Sideband Extraction (RSE) which extracts the gravitational wave signals from the arm cavities.

3.1 Normalised sensitivity

The interferometer response $G(\omega)$ from the amplitude of a gravity wave $h(\omega)$ to the relative phase of the interfering beams $\delta\phi(\omega)$ caused by the gravitational wave is considered as follows,

$$G(\omega) = \frac{\delta\phi(\omega)}{h(\omega)}, \tag{3.1}$$

where ω is the frequency of the gravitational wave. However, if the absolute value of the response function $|G(\omega)|$ is used as it is, it becomes a large number of $\sim 10^{13}$. In addition, upper and lower sidebands must be added because modulated components

of the gravitational wave are detected. Therefore, the response function is normalized as follows

$$G'(\omega) = \frac{4}{\omega_0 t_{\rm a}} \times \bar{G}(\omega) = \frac{4}{\omega_0 t_{\rm a}} \times [G(\omega) + G^*(-\omega)]\,. \tag{3.2}$$

We call $G'(\omega)$ the 'normalized sensitivity'. ω_0 denotes the carrier frequency, it will be a large number of several hundreds of THz, and $t_{\rm a}$, which is given as

$$t_{\rm a} = \frac{2L}{c} \tag{3.3}$$

is a round trip time of the light in the cavity of L in length.

Let us naively assume that the shot noise itself is determined only by the incident laser power, not by the optical configurations to be considered. With this assumption, shot-noise limited sensitivity of the interferometer is naively proportional to the Normalized Sensitivity. Therefore, the sensitivity of the interferometer can be compared by the normalized sensitivity, as is done in this thesis. The relationship between the response function and the shot-noise limited sensitivity is given as

$$\tilde{h}(\omega) \;=\; \frac{1}{2\bar{G}(\omega)}\sqrt{\frac{2\hbar\omega_0}{P_0}} = \frac{2}{G'(\omega)}\frac{\sqrt{2\hbar\omega_0}/P_0}{\omega_0 t_{\rm a}} \tag{3.4}$$

where P_0 is the incident laser power, and $\hbar$ is Planck's constant.

3.2 Fabry-Perot Michelson interferometers

Fig. 3.1 shows a Michelson interferometer with a Fabry-Perot cavity in each arm. This is called Fabry-Perot Michelson interferometer (FPMI). FPMI has been a conventional configuration for a long time as a prototype interferometer of a gravitational detector. The light from the source is divided by a beamsplitter into two arms. Each arm contains two mirrors facing each other, which compose a Fabry-Perot cavity. The reflected light from the cavity in each arm interferes with that from the other arm at the beamsplitter. The beamsplitter is controlled in order to set the condition for constructive or destructive interference. Almost all the light goes back to the laser source, we call this port a 'symmetric port (SY)'. The detection port is kept dark in order to reduce the shot noise. This port is called an 'anti-symmetric port (AS)'. .

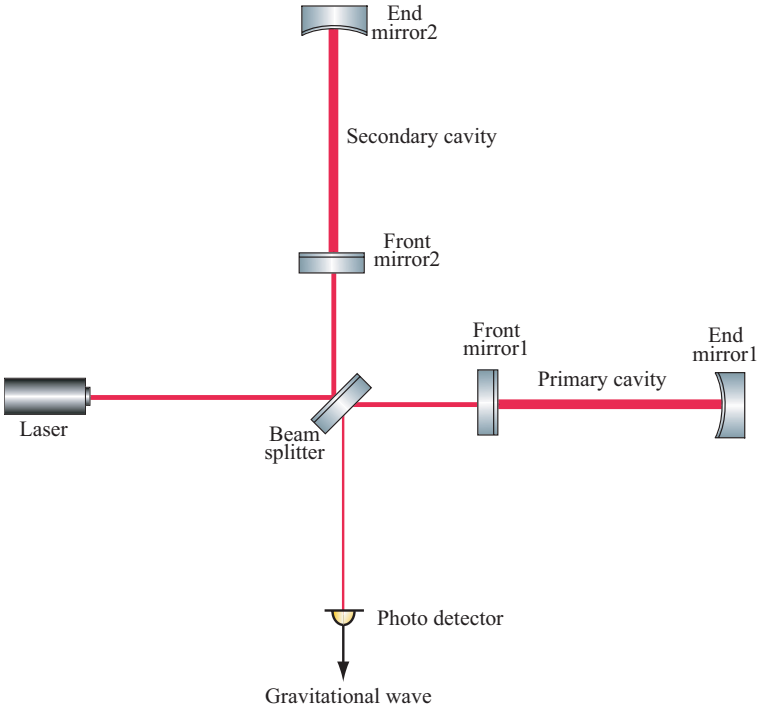

Figure 3.1: Optical configuration of an interferometer with a Fabry-Perot cavity in each arm. The light from the source is divided by a beamsplitter into two arms. Each arm contains two mirrors facing each other, which compose a Fabry-Perot cavity. The reflected light from the cavity in each arm interferes with that from the other arm at the beamsplitter.

3.2.1 The response function of a Fabry-Perot cavity

We start by considering the response of a single Fabry-Perot cavity to gravitational waves. The phase difference $\delta\phi(t)$ of the Fabry-Perot cavity caused by the gravitational wave $h(t)$ is represented as,

$$\delta\phi(t) = \int_{t-t_{\rm r}}^{t} \frac{1}{2}\omega_0 h(t)dt, \tag{3.5}$$

where ω_0 is an angular frequency of the carrier light, and $t_{\rm r}$ is a round trip time of the light in the cavity of L in length:

$$t_{\rm r} = \frac{2L}{c}. \tag{3.6}$$

We apply a Laplace transformation to Eq. (3.5)

$$\begin{aligned}
\mathcal{L}\{\delta\phi(t)\} &= \frac{\omega_0}{2}\mathcal{L}\left\{\int_{t-t_{\rm r}}^{t} h(t)dt\right\} \\
&= \frac{\omega_0}{2}[\mathcal{L}\left\{\int_{0}^{t} h(t)dt\right\} - \mathcal{L}\left\{\int_{0}^{t-t_{\rm r}} h(t)dt\right\}] \\
&= \frac{\omega_0}{2}\frac{1-e^{-st_{\rm r}}}{s}\mathcal{L}\{h(t)\} \qquad (3.7)
\end{aligned}$$

then the response function $X(\omega)$ is given as

$$X(\omega) = \frac{\mathcal{L}\{\delta\phi(t)\}}{\mathcal{L}\{h(t)\}} = \frac{\omega_0}{2}\frac{1-{\rm e}^{-i\omega t_r}}{i\omega} \qquad (3.8)$$

with s replaced by $s = i\omega$. ω denotes the frequency of the gravitational wave.

The light is bounced back and forth in the Fabry-Perot cavity many times. When reflectivity and transmissivity of the front mirror is $r_{\rm F}, t_{\rm F}$, and those of the end mirror is $r_{\rm E}, t_{\rm E}$, the response function of the Fabry-Perot cavity is given as

$$G_{\rm FP}(\omega) = t_{\rm F}^2 \sum_{n=1}^{\infty}\left[r_{\rm F}^{n-1} r_{\rm E}^{n} \times \frac{1}{2}X_{2n}(\omega)\right], \qquad (3.9)$$

where X_{2n} is given from Eq. (3.8) with $t_{\rm r}$ replaced by $t_{\rm r} = 2n \times L/c = nt_{\rm a}$. $t_{\rm a}$ represents a storage time of one round trip in the cavity.

Eq. (3.9) is expanded as,

$$\begin{aligned}
G_{\rm FP}(\omega) &= t_{\rm F}^2 \sum_{n=1}^{\infty}\frac{r_{\rm F}^{n-1} r_{\rm E}^{n}}{2}\frac{\omega_0}{2}\frac{1-{\rm e}^{-in\omega t_{\rm a}}}{i\omega} \\
&= \frac{\omega_0}{i4\omega}\frac{t_{\rm F}^2}{r_{\rm F}}\sum_{n=1}^{\infty}(r_{\rm F}r_{\rm E})^n(1-{\rm e}^{-in\omega t_{\rm a}}) \\
&= \frac{\omega_0}{i4\omega}\frac{t_{\rm F}^2}{r_{\rm F}}\left(\frac{r_{\rm F}r_{\rm E}}{1-r_{\rm F}r_{\rm E}} - \frac{r_{\rm F}r_{\rm E}{\rm e}^{-i\omega t_{\rm a}}}{1-r_{\rm F}r_{\rm E}{\rm e}^{-i\omega t_{\rm a}}}\right) \\
&= \frac{t_{\rm F}^2}{(1-r_{\rm F}r_{\rm E})(1-r_{\rm F}r_{\rm E}{\rm e}^{-in\omega t_{\rm a}})} \times \frac{r_{\rm E}\omega_0}{4}\frac{1-{\rm e}^{-i\omega t_{\rm a}}}{i\omega} \qquad (3.10)
\end{aligned}$$

Note that this can be separated into two factors. The first factor can be regarded as the power enhancement and frequency response effect of the Fabry-Perot cavity, and the second factor has the same form as that for a single bounce Michelson interferometer.

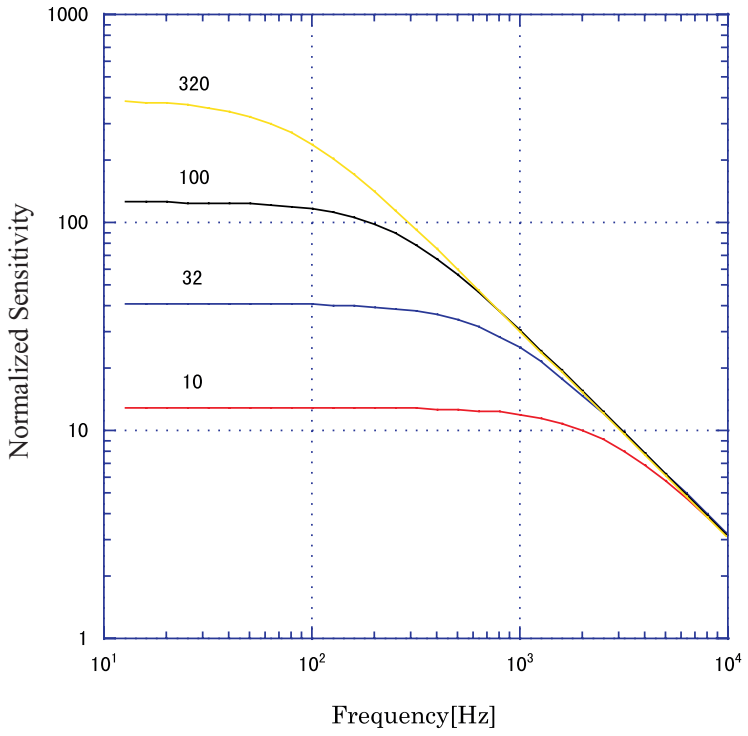

Figure 3.2: The normalized response of interferometer with 3km Fabry-Perot cavity in the arms. Each plot corresponds to a different finesse of the cavity in the arm. The sensitivity is flat from DC to certain cut-off frequency which is determined by the storage time in the arms. The slope in the higher frequency range is proportional to $1/\omega$.

3.2.2 Finesse

Eq. (3.10) is normalized by equation 3.2, and some examples of the normalized sensitivity of the Fabry-Perot Michelson interferometer are shown as a response for the frequency of the gravitational wave in the Fig. 3.2. We calculated with a wavelength of light as $\lambda = 1064$nm, and length of an arm cavity as 3km.

Numbers shown in Fig. 3.2 are called 'finesse $\mathcal{F}$' defined as

$$\mathcal{F} = \frac{\sqrt{r_{\rm F} r_{\rm E}}}{1 - r_{\rm F} r_{\rm E}}. \tag{3.11}$$

This is a quantity determined only by reflectivities of the two mirrors composing a cavity.

If the finesse is high, the sensitivity at DC improves, but the cut-off frequency goes down simultaneously. It means that the band-width of detection will be small.

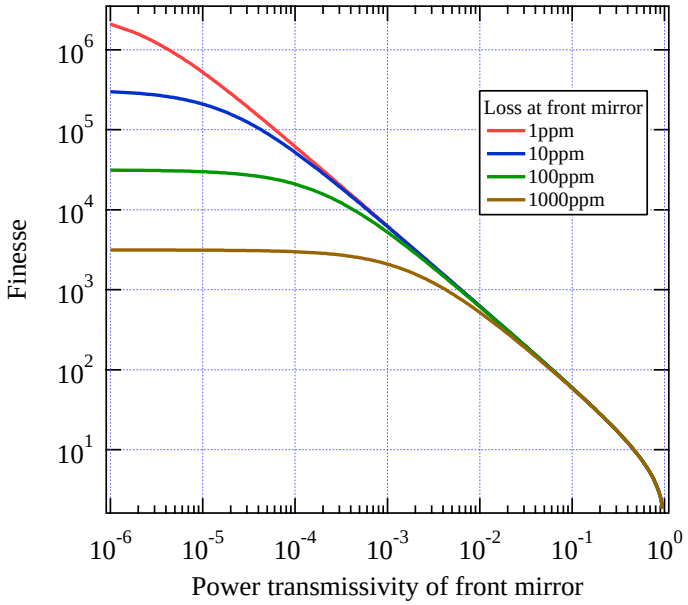

Figure 3.3: Finesse of 3km Fabry-Perot cavity as a function of power transmissivity of the front mirror. Each plot corresponds to different loss of the mirror surface. The finesse is limited at a certain transmissivity because of loss.

This is because the gravitational wave changes its phase before the light escapes from the cavity, resulting in some cancellation of the gravitational wave signals.

Finesse $\mathcal{F}$ is related to effective bounces of light N as,

$$N = \frac{2}{\pi}\mathcal{F} \tag{3.12}$$

3.2.3 Effect of loss on finesse

When loss on the coating surface of the mirror is considered, finesse has an upper limit. Reflectivity and transmissivity of the front and end mirror are related to the loss $A_{\rm F}$ and $A_{\rm E}$ by the following equations:

$$1 = r_{\rm F}^2 + t_{\rm F}^2 + A_{\rm F} \tag{3.13}$$

$$1 = r_{\rm E}^2 + t_{\rm E}^2 + A_{\rm E}. \tag{3.14}$$

From Eq. (3.11) and (3.13), (3.14), the relationship between the finesse and the transmissivity $t_{\rm F}$ of the front mirror when loss exists is shown in Fig. 3.3. Here, it is

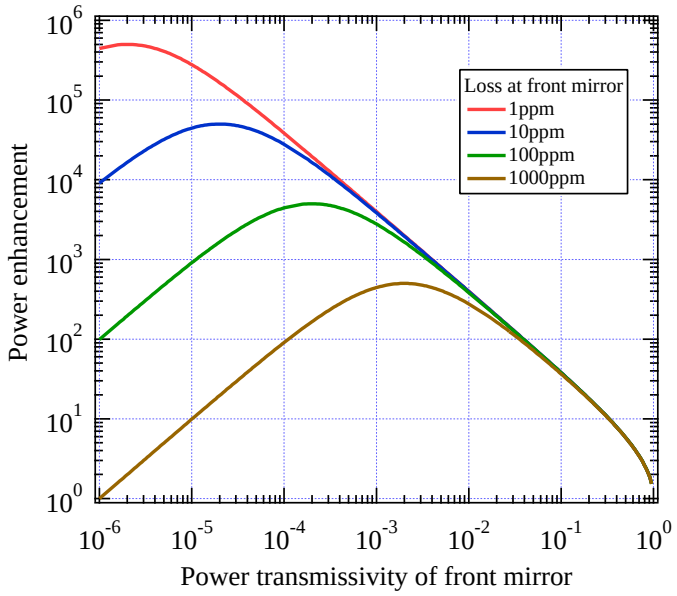

Figure 3.4: Ratio of the incident power to the power inside cavity a function of power transmissivity of the front mirror. Each plot corresponds to different loss of the mirror surface. The power enhancement has a peak at a certain transmissivity. The cavity with transmissivity of right area of the peak is called an over coupled cavity and cavity of left area is called under coupled cavity. Maximum power which can be achieved depends on the loss.

assumed that both mirrors have the same loss as $A_{\mathrm{F}} = A_{\mathrm{E}}$ and that transmissivity of the end mirror is zero, $t_{\mathrm{E}} = 0$. Each curve indicates the case of 1 ppm, 10 ppm, and 100 ppm loss, respectively. It is shown that there is the upper limit of the finesse which can be achieved for a given amount of loss.

The flat area of these graphs is called an under-coupled state where the transmissivity of the front mirror is smaller than the total loss inside the cavity (including the transmissivity of the end mirror). Arm cavities of the interferometer are usually used in an over-coupled state where the transmissivity of the front mirror is larger than the total loss inside the cavity. The power in the cavity rolls off in an under-coupled state. Fig. 3.4 shows the ratio of power in a cavity to incident power as a function of the transmissivity t_{F} of the front mirror. It is shown that the maximum power enhancement is obtained when the transmissivity of the front mirror is equal to the total loss inside the cavity (optimally-coupled state). In the optimally-coupled state the light is not reflected by the arm cavities, since all the light is consumed inside

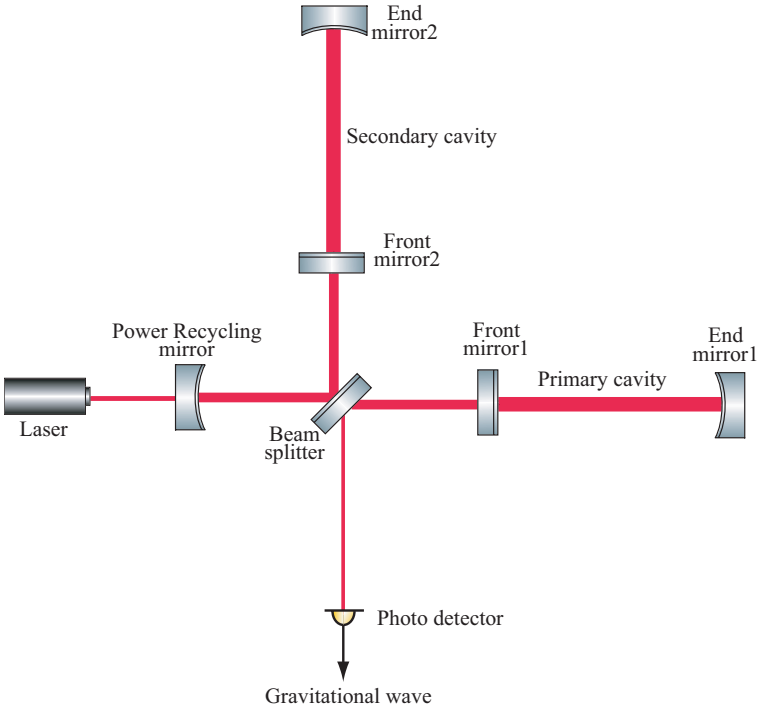

Figure 3.5: Optical configuration of a power recycled interferometer with a Fabry-Perot cavity in each arm. The power recycling mirror is added in order to compose a power recycling cavity with interferometer which is considered as a compound mirror. The light is enhanced in the power recycling cavity, resulting in the increase in the effective laser power available for the interferometer.

the cavities.

3.3 Power recycling

The shot noise sensitivity of the interferometer is in proportion to root of incident laser power as shown in Eq. (3.4). Almost all the light returns to the laser source (SY port) in the Fabry-Perot Michelson interferometer. This light is entirely abandoned in the case of a Fabry-Perot Michelson interferometer. An idea of recycling this light was proposed. The idea is that a mirror is added to the SY port to reflect the light coherently back to the interferometer. An optical configuration of the PRFPMI is shown in Fig 3.5.

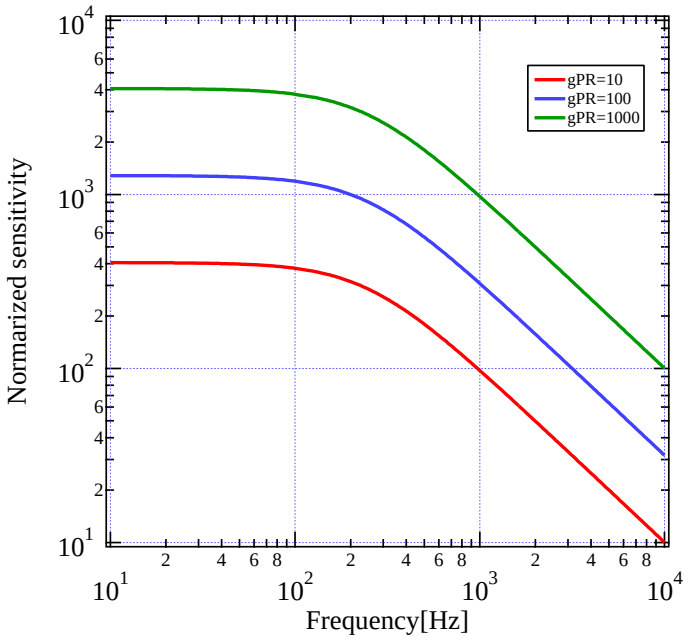

Figure 3.6: Normalized sensitivity of a power recycled interferometer with 3 km Fabry-Perot cavities in the arms. Each curve corresponds to a different power recycling gain. The sensitivity is enhanced by $\sqrt{g_{\rm PR}}$ compared with the FPMI sensitivity.

3.3.1 Response function

The response function of the PRFPMI to gravitational waves is given as

$$G_{\rm PR}(\omega) \;=\; \sqrt{g_{\rm PR}}\frac{t_{\rm F}^2}{(1-r_{\rm F}r_{\rm E})(1-r_{\rm F}r_{\rm E}{\rm e}^{-in\omega t_{\rm a}})}\times\frac{r_{\rm E}\omega_0}{4}\frac{1-{\rm e}^{-i\omega t_{\rm a}}}{i\omega}. \qquad (3.15)$$

This is only different by a factor $\sqrt{g_{\rm PR}}$ compared with the case of FPMI. $g_{\rm PR}$ is called the power recycling gain. It represents the ratio of the effective incident power to the incident power of the FPMI. Because this value has no frequency dependence and can be fixed when the parameters of the interferometer are given, it becomes $\sqrt{g_{\rm PR}}$ times the response function of FPMI at all frequencies.

The normalized sensitivity of the power recycled interferometer is shown in Fig. 3.6. Each curve corresponds to the case of a difference power recycling gain factor $g_{\rm PR} = 10, 100, 1000$ with the arm length of 3 km long and a finesse of 100 for LCGT.

3.3.2 Power recycling gain

As discussed in Sec. 3.2.3, for the maximum enhancement of the light power inside the cavity and no reflection of the light by the cavity the transmissivity of the front mirror must be equal to the total loss inside the cavity.

The power recycled FPMI can be regarded as a simple Fabry-Perot cavity by regarding the FPMI part as a compound mirror. This Fabry-Perot cavity consists of the power recycling mirror and the compound mirror. Therefore the light enhancement inside the recycling cavity is maximized and the light reflected by the recycling cavity vanishes when the transmissivity of the recycling mirror is equal to the total loss inside the recycling cavity. The total loss inside the recycling cavity is the sum of the loss in the recycling mirror and the loss in the compound mirror, that is the FPMI. In the practical case the latter is much larger than the former, so we consider only the loss in the FPMI. It consists of the loss in the arm cavities, the loss in the beamsplitter and the substrates of the front mirror, and the loss due to the contrast defect of the Michelson interferometer. The loss in the arm cavities is defined by $1 - r_{\mathrm{reso}}$, where r_{reso} is the reflectivity of the arm cavity. r_{reso} is determined by the reflectivities of the mirrors (r_{F}, r_{E}) and the transmissivity of the front mirror (t_{F}), which is related to the loss on the surface of the front mirror (A_{F}).

$$\begin{aligned} r_{\mathrm{reso}} &= -r_{\mathrm{F}} + \frac{t_{\mathrm{F}}^2 r_{\mathrm{E}}}{1 - r_{\mathrm{F}} r_{\mathrm{E}}} \\ &= \frac{r_{\mathrm{E}}(t_{\mathrm{F}}^2 + t_{\mathrm{F}}^2) - r_{\mathrm{F}}}{1 - r_{\mathrm{F}} r_{\mathrm{E}}} \\ &= \frac{r_{\mathrm{E}}(1 - A_{\mathrm{F}}) - r_{\mathrm{F}}}{1 - r_{\mathrm{F}} r_{\mathrm{E}}} \end{aligned} \tag{3.16}$$

Fig. 3.7 shows the reflectivity of the arm cavity r_{reso} vs. transmissivity t_{F} of the front mirror. It is assumed that both mirrors have the same loss, $A_{\mathrm{F}} = A_{\mathrm{E}}$, and that the transmissivity of end mirror is zero, $t_{\mathrm{E}} = 0$. The curves correspond to a loss of 1 ppm, 10 ppm, 100 ppm, and 1000 ppm, respectively. The reason why the reflectivity can be negative is that in the case of the over-coupled cavity, the phase of the light reflected by the cavity is reversed, while the phase of the light is maintained on reflection for the under-coupled case. The arm cavities of the interferometer are usually put in the over-coupled state. In such a case the reflectivity of the cavity has a significant dependence on the loss: the larger loss in the mirrors makes the

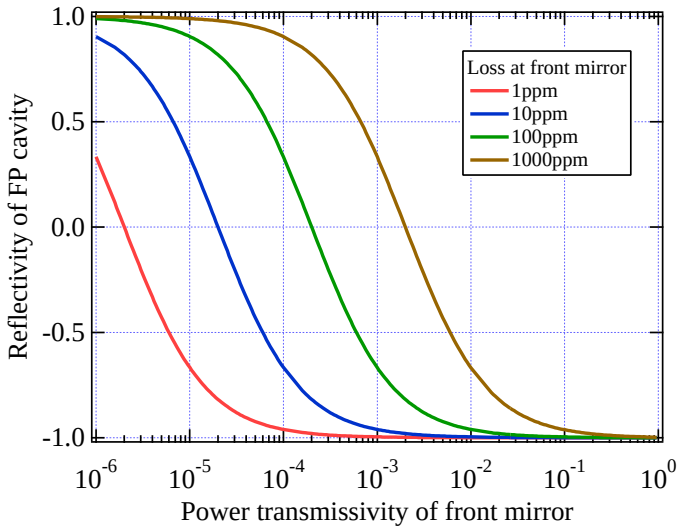

Figure 3.7: Reflectivity of the Fabry-Perot cavity as a function of power transmissivity of the front mirror. Each plot corresponds to different loss of the mirror surface. The reflectivity is negative in the over-coupled area because the phase of carrier is inverted at the reflection. On the other hand the reflectivity is positive in the under-coupled area.

reflectivity of the cavity lower.

Now let us consider the maximum-attainable power recycling gain. The recycling gain is given by the transmissivity ($t_{\rm p}$) and reflectivity ($r_{\rm p}$) of the recycling mirror and the reflectivity of the compound mirror ($r_{{\rm com_r},0}$):

$$g_{\rm PR,max} = \left(\frac{t_{\rm p}}{1 - r_{\rm p} r_{{\rm com_r},0}} \right)^2 , \tag{3.17}$$

When the transmissivity of the power recycling mirror is equal to the loss in the recycling cavity, the recycling gain is maximized. Under this condition Eq. (3.17) becomes the following:

$$g_{\rm PR} \simeq \frac{1}{A_{{\rm com_r},0}} \tag{3.18}$$

Here, it is assumed that the loss in the recycling cavity is negligible compared with the loss in the FPMI:

$$1 \gg A_{{\rm com_r},0} \gg A_{\rm p} \tag{3.19}$$

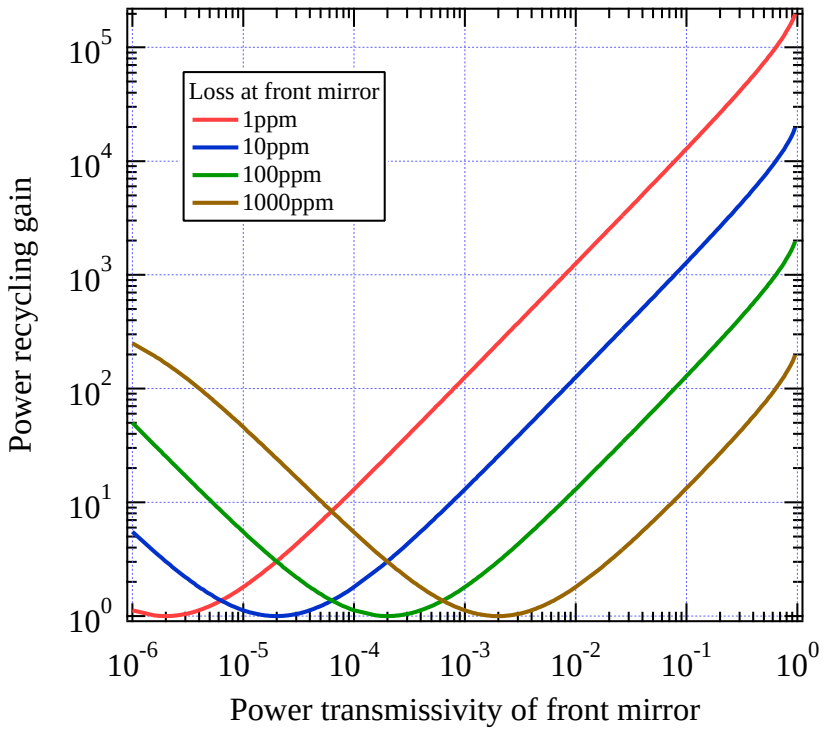

Figure 3.8: Power recycling gain g_{PR} which can be achieved as a function of power transmissivity of the front mirror. Each plot corresponds to a different loss of the mirror surface. The power recycling gain is limited by the reflectivity of the compound mirror (FPMI).

Fig. 3.8 shows the dependence of the maximum power recycling gain $g_{\mathrm{PR,max}}$ on the transmissivity t_{F} of the front mirror for a given loss in the arm cavity mirrors. The curves correspond to a loss of 1 ppm, 10 ppm, 100 ppm, and 1000 ppm, respectively. It is assumed that there is no contrast defect in the Michelson interferometer, $C = 1$, for simplicity. For each plot the right side of the curve reflects the over-coupled case. In this case the maximum recycling gain significantly depends on the loss in the arm cavity mirrors: larger loss in the mirrors makes the maximum recycling gain lower.

Fig. 3.9 shows the relationship between the finesse of the arm cavities and the maximum recycling gain. For each plot the left side of the curve reflects the over-coupled case. In this case the higher finesse of the arm cavities makes the maximum recycling gain lower.

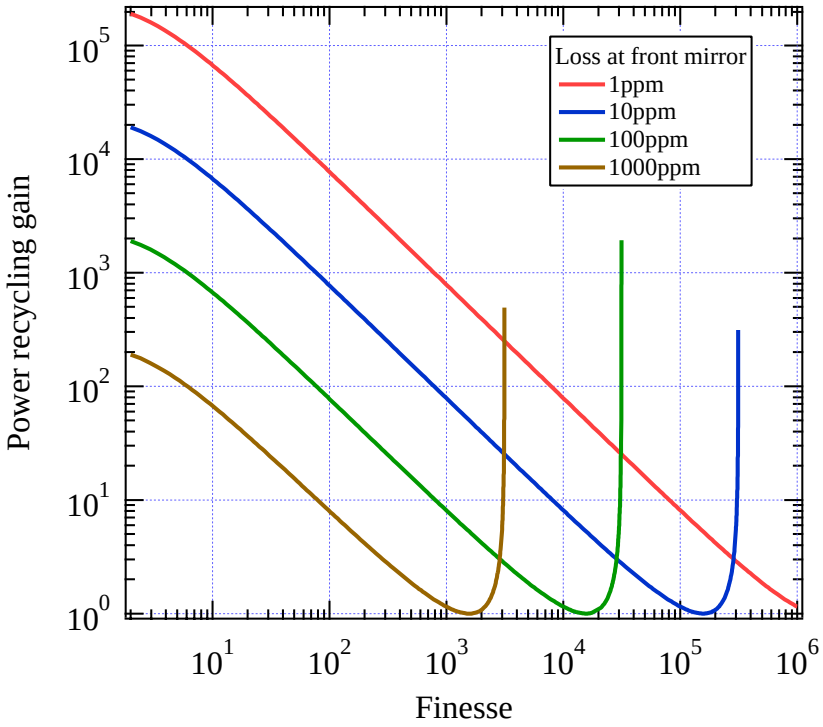

Figure 3.9: Power recycling gain g_{PR} which can be achieved as a function of Finesse of the Fabry-Perot cavity. Each plot corresponds to different loss of the mirror surface.

3.4 Signal recycling (dual recycling)

Signal recycling is a technique to recycle the gravitational wave signals appearing at the anti-symmetric port, as power recycling recycles the carrier light returning at the symmetric port. Fig. 3.10 shows an optical configuration using signal recycling. In addition to the power recycling mirror, another mirror which is called a 'signal recycling mirror' is placed at the the anti-symmetric port.

Because the light appearing at the anti-symmetric port is the audio sidebands produced by the gravitational wave, the storage time of the gravitational wave signals increases when it is recycled. The most outstanding advantages of the SR interferometer is that the enhancement of the carrier light and gravitational wave signals can be set completely independently. Therefore, for the arm cavities with reduced finesse, the enhancement of the gravitational wave signals can be maintained by SR. In this case SR needs to employ higher power recycling gain to enhance the carrier light. Since the SR interferometer is almost always used together with the power

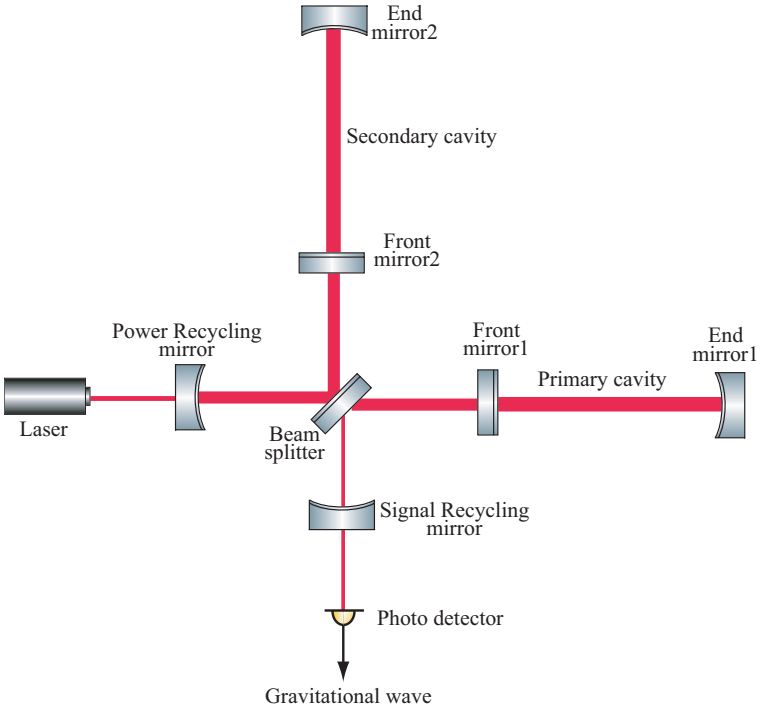

Figure 3.10: Optical configuration of a signal-recycled interferometer with a Fabry-Perot cavity in each arm. A signal recycling mirror is added in order to compose a signal recycling cavity. The gravitational wave signal near the carrier frequency is enhanced in the signal recycling cavity, and the signal storage-time can be longer than the storage-time of the FPMI configuration. Therefore signal recycling needs low finesse arm cavities and high power recycling gain.

recycling, it is also called 'dual recycling (DR)'.

3.4.1 Response function

In order to consider the response function of the SR interferometer, let us simplify SR to a three-mirror coupled cavity as shown in Fig. 3.11, assuming the two arms are identical and the Michelson interferometer stays at a dark fringe. We consider a signal recycling cavity (SRC) which is composed of the front mirror of the arm cavity and a signal recycling mirror. This signal recycling cavity can be regarded as a compound mirror. Therefore SR can be regarded as a simple cavity.

A response function of the signal recycled FPMI is given as follows:

$$G_{\rm SR}(\omega) = \sqrt{g_{\rm PR_{SR}}}\frac{t_{\rm SRC}^2}{(1-r_{\rm SRC}r_{\rm E})(1-r_{\rm SRC}r_{\rm E}{\rm e}^{-in\omega t_{\rm a}})}\times\frac{r_{\rm E}\omega_0}{4}\frac{1-{\rm e}^{-i\omega t_{\rm a}}}{i\omega}, \quad (3.20)$$

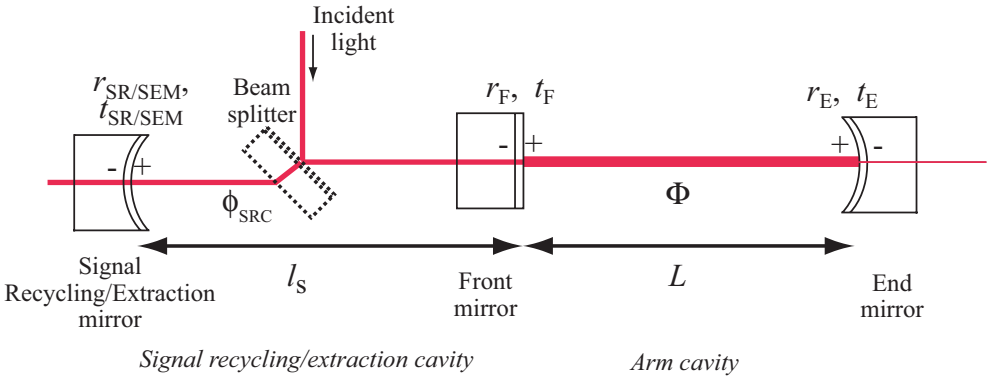

Figure 3.11: Schematic diagram of the three-mirror coupled cavity representing the SR interferometer.

where $r_{\rm SRC}$ and $t_{\rm SRC}$ denote the reflectivity and transmissivity of the compound mirror as follows (the detail of the derivation of the equations will be described in chapter 4)

$$r_{\rm SRC} = \frac{r_{\rm F} - r_{\rm SR_A} e^{-i2\phi_{\rm SRC}}}{1 - r_{\rm F} r_{\rm SR_A} e^{-i2\phi_{\rm SRC}}} \tag{3.21}$$

$$t_{\rm SRC} = \frac{t_{\rm F} t_{\rm SR_A} e^{-i\phi_{\rm SRC}}}{1 - r_{\rm F} r_{\rm SR_A} e^{-i2\phi_{\rm SRC}}}, \tag{3.22}$$

where $r_{\rm SR_A}$ and $t_{\rm SR_A}$ stand for the reflectivity and transmissivity of the signal recycling mirror including the loss existing inside the SR cavity and the loss due to the contrast effect in the Michelson interferometer. They are defined as follows:

$$r_{\rm SR_A} = r_{\rm SR}(1 - A_{\rm BS})\frac{1 + C}{2} \tag{3.23}$$

$$t_{\rm SR_A} = t_{\rm SR}\sqrt{(1 - A_{\rm BS})\frac{1 + C}{2}} \tag{3.24}$$

Here,

$$\phi_{\rm SRC} = \frac{\omega l_{\rm s}}{c} + \psi \tag{3.25}$$

is the tuning of the signal extraction cavity with ψ, which is the initial detuning at the carrier frequency defined as

$$\psi = \frac{\omega_0 l_{\rm s}}{c} \tag{3.26}$$

and C is a visibility defined by current at SY port $I_{\rm SY}$ and current at AS port $I_{\rm AS}$ as

$$C = \frac{I_{\rm SY} - I_{\rm AS}}{I_{\rm SY} + I_{\rm AS}}. \tag{3.27}$$

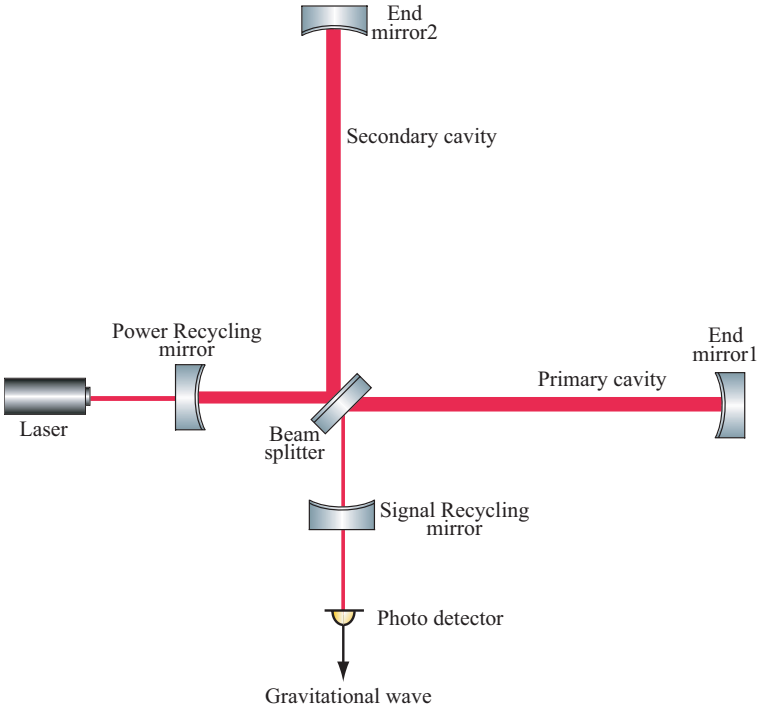

Figure 3.12: Optical configuration of an extreme dual recycling (DR) which has no Fabry-Perot arm cavities. Without Fabry-Perot arm cavities, higher power recycling gain is needed to obtain enough power in each arm. The signal storage-time is lengthened by the signal recycling mirror.

In the realistic interferometer, the length of the signal recycling cavity is much shorter than the length of arm cavity

$$\omega_0 l_s / c \ll \psi, \tag{3.28}$$

so $\phi_{\rm SRC} (\simeq \psi)$ is considered as a detuning phase actually.

Therefore the condition of the conventional SR is represented as

$$\phi_{\rm SRC} = \pi/2. \tag{3.29}$$

3.4.2 Extreme dual recycling

In the case of $r_{\rm F_{SR}} = 0$, when there is no front mirror and thus no Fabry-Perot arm cavities, let us call the DR interferometer an 'extreme DR (ExDR)' . This is the configuration which the GEO group adopted. Instead of increasing the effective optical length by the Fabry-Perot arm cavities, they enhance the light power by

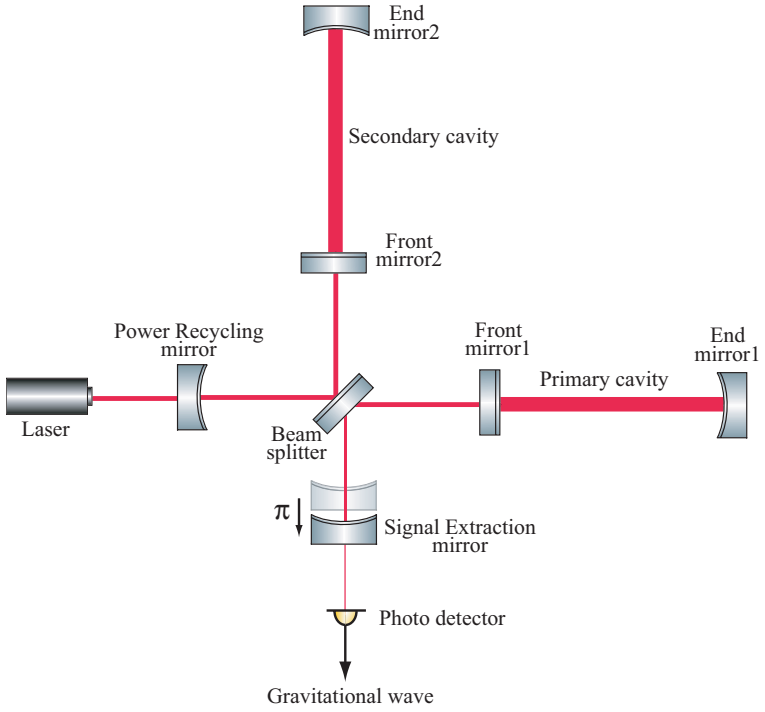

Figure 3.13: Optical configuration of a resonant sideband extraction (RSE) interferometer. RSE requires high finesse cavities in each arm for maximum power storage. A signal extraction mirror (SEM) is added in order to compose a signal extraction cavity (SEC) shorten the storage-time of the gravitational wave signal compared to the FPMI configuration. This effect can widen the band-width.

power recycling and the gravitational signals by signal recycling. Fig. 3.12 shows an optical configuration of the ExDR. Naturally, the power of the light going through the substrates of the beamsplitter is largest in the case of the ExDR.

3.5 Resonant sideband extraction (RSE)

Heat from the mirror substrate will cause a thermal lensing effect, and degrade the sensitivity of the interferometer. For the power of the laser currently used, this thermal lensing effect is negligible. However, the thermal lensing effect will cause a serious problem for large-scale interferometers in the future with the high power lasers required to further improve the shot noise.

Mizuno proposed a new optical configuration called 'resonant sideband extraction' (as shown in Fig. 3.13) to avoid the generation of the heat in the substrates. The configuration of RSE is very similar to that of DR, except that the mirror placed at

the anti-symmetric port is called a 'signal extraction mirror (SEM)' and the cavity consisting of the SEM and the front mirror of the arm cavity is called a 'signal extraction cavity (SEC)'. The SEM can extract the gravitational wave signals from the arm cavities before the gravitational wave signals would be averaged out by the high-finesse arm cavity.

The response function of the RSE can be obtained using a three-mirror coupled cavity in the same way as signal recycling as follows:

$$G_{\rm RSE}(\omega) = \sqrt{g_{\rm PR_{RSE}}}\frac{t_{\rm SEC}^2}{(1-r_{\rm SEC}r_{\rm E})(1-r_{\rm SEC}r_{\rm E}{\rm e}^{-in\omega t_{\rm a}})}\times\frac{r_{\rm E}\omega_0}{4}\frac{1-{\rm e}^{-i\omega t_{\rm a}}}{i\omega}, \quad (3.30)$$

where $r_{\rm SEC}$ and $t_{\rm SEC}$ represent the reflectivity and transmissivity of the compound mirror consisting of the front mirror and the SEM, and they are given as follows:

$$r_{\rm SEC} = \frac{r_{\rm F}-r_{\rm SEM_A}e^{-i2\phi_{\rm SEC}}}{1-r_{\rm F}r_{\rm SEM_A}e^{-i2\phi_{\rm SEC}}} \quad (3.31)$$

$$t_{\rm SEC} = \frac{t_{\rm F}t_{\rm SEM_A}e^{-i\phi_{\rm SEC}}}{1-r_{\rm F}r_{\rm SEM_A}e^{-i2\phi_{\rm SEC}}}, \quad (3.32)$$

where $r_{\rm SEM_A}$ and $t_{\rm SEM_A}$ stand for the reflectivity and transmissivity of the signal extraction mirror including the loss existing inside the SEC and the loss due to the contrast effect in the Michelson interferometer. They are defined as follows:

$$r_{\rm SEM_A} = r_{\rm SEM}(1-A_{\rm BS})\frac{1+C}{2} \quad (3.33)$$

$$t_{\rm SEM_A} = t_{\rm SEM}\sqrt{(1-A_{\rm BS})\frac{1+C}{2}}. \quad (3.34)$$

The RSE has high-finesse arm cavities, thus lower power recycling gain is required.

$$g_{\rm PR_{SR}} > g_{\rm PR} > g_{\rm PR_{RSE}} \quad (3.35)$$

The one-way phase of the SEC for the career (microscopic length) is π (mod 2π). The transmissivity of the SEC for the gravitational wave signals is lowered on the resonance condition of the carrier in the SEC. As a result, the effective finesse for the gravitational wave signals decreases, and the bandwidth for the signals expands. The mirror is controlled so that the phase of the signal extraction cavity for the carrier should be

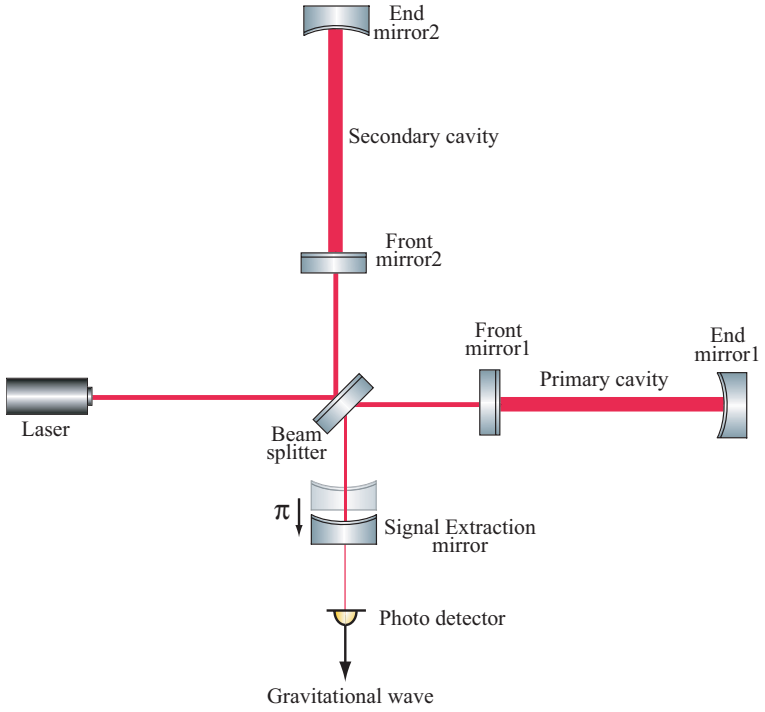

Figure 3.14: Optical configuration of an extreme resonant sideband extraction (ExRSE) interferometer. The difference from RSE is that ExRSE has no power recycling, but instead has higher finesse arm cavities to maximize the higher power in each arm. The ExRSE needs higher reflectivity of the SEM to extract the gravitational wave signal.

$$\phi_{\rm SEC} = \pi \tag{3.36}$$

.

3.5.1 Extreme RSE

Let us call RSE without power recycling an 'extreme RSE (ExRSE)'. Fig. 3.14 shows an optical configuration for ExRSE. When the transmissivity of the front mirror is equal to the total loss inside the arm cavities, the highest finesse is achieved. We will discuss later that finesse is limited by the loss in the substrates.

The ExRSE is the most advantageous for thermal effect because the light power at the beamsplitter or the substrates of the front mirrors, where heat is primarily generated, is the lowest of the various configurations.

3.6 Comparison of sensitivity in various optical configurations

In this section, we discuss the sensitivity dependence on configurations of the interferometer: ExDR, DR, PRFPMI, RSE, and ExRSE. Fig. 3.15 shows a summary of the relationship of each optical configuration.

The finesse and the power recycling gain have an opposite relation. The ExDR has no FP cavity in each arm, but has the highest power recycling gain, while the ExRSE has no power recycling, but the finesse of arm cavities is the highest. The thermal lensing effect is caused by laser power heating in substrates of optics such as the beamsplitter or the front mirrors. If the incident power is the same, power in the substrates is proportional to the power recycling gain. Therefore, the effect of the thermal lensing is the highest for the ExDR and smallest for the ExRSE.

Additionally, the number of degrees of freedom which must be controlled will be important when the interferometer is actually operated. The fewer degrees of freedom to be controlled the easier the control system necessary for stable operation becomes. The ExDR is the easiest to control because there are only three degrees of freedom. A considerably complex control system is necessary for DR and RSE: there are five degrees of freedom to control.

Here we concentrate on the comparison of the interferometer sensitivity instead of the above-mentioned heating issue or control complexity. We use the normalized sensitivity to evaluate the sensitivity of each configuration. It should be noted that the normalized sensitivity does not depend on the incident laser power, so it makes it possible to compare various configurations without practical limitations caused by laser power.

The sensitivity of each configuration is greatly influenced by the loss. There are several kinds of losses: the loss existing on the surface of a mirror ($A_{\rm sur}$), the loss existing in the substrates of the beamsplitter and the front mirrors ($A_{\rm sub}$), and the loss due to the contrast defect in the Michelson interferometer. We will deal with the former two losses and not discuss the loss due to the contrast defect because the estimate of the contrast defect requires serious investigation of the wave deformation of the light due to the roughness of the mirror. We discuss the following three cases,

1. Loss-less case.

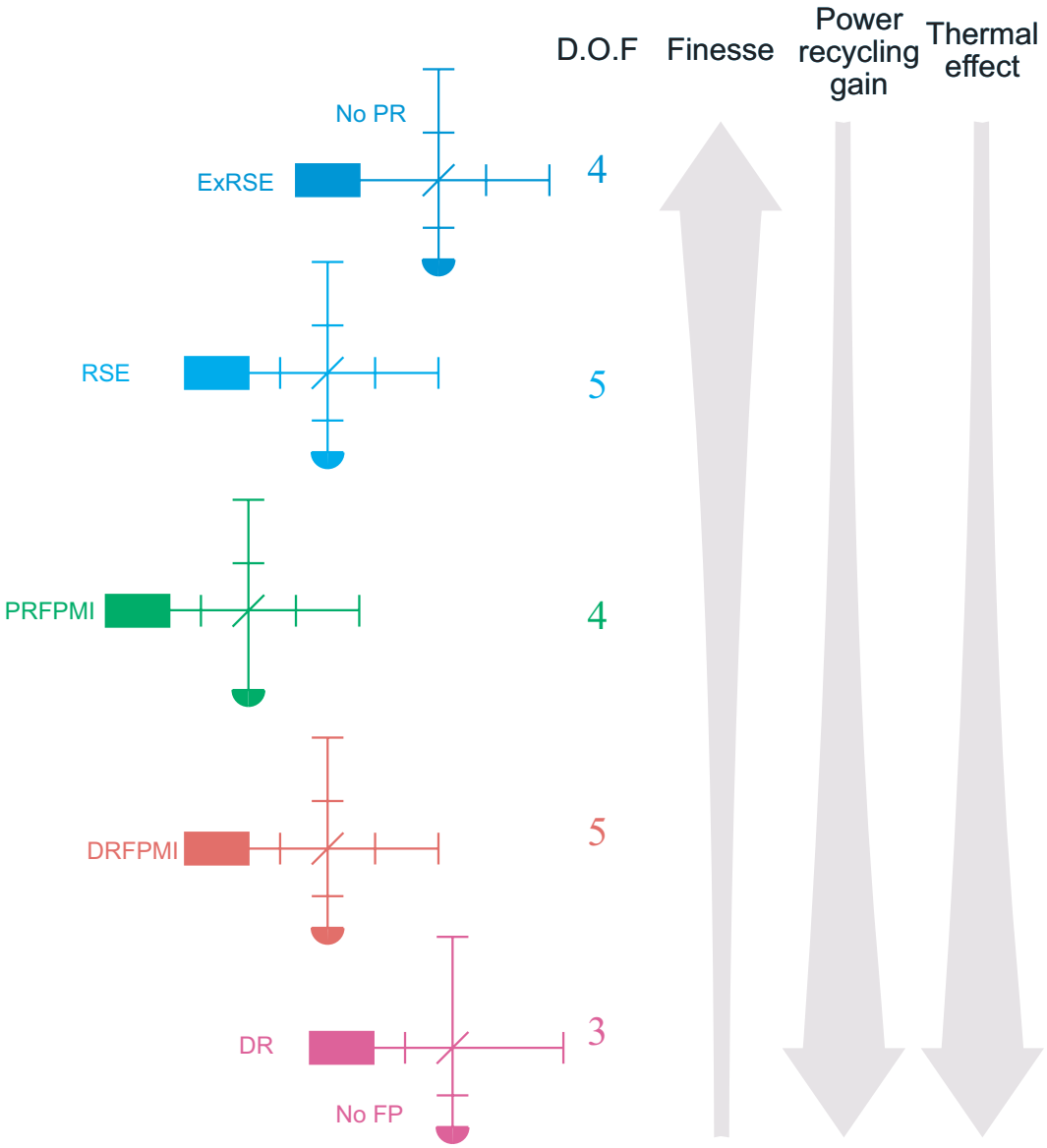

Figure 3.15: Comparison of optical configurations for advanced interferometer. Numbers represents the degree of freedom which should be controlled. Relations for finesse, power recycling gain, and thermal lensing effect are shown also.

Table 3.1: Optical parameters of a model interferometer used in the calculation.

Parameter	Symbol	Value
Wave length of the laser	λ	1064 nm
Length of the arm cavities	L	3 km
Length of the signal extraction cavity	$l_{\rm s}$	10 m
Band-width	f_0	100 Hz
Reflectivity of the beam splitter	$r^2_{\rm BS}$	50 %
Reflectivity of the end mirror	$t^2_{\rm E}$	0.00001 %
Contrast	C	1

2. Loss is dominant by 'surface loss $A_{\rm sur}$'.

3. Loss is dominant by 'substrate loss $A_{\rm sub}$'.

Table 3.1 shows optical parameters of the interferometer used for calculation here. We assume parameters for the LCGT. The length of the arm is 3 km. The finesse (determined by the reflectivity of the front mirror) and the reflectivity of the SRM/SEM are adjusted so that the bandwidth of the gravitational wave signals is 100Hz. Detuning is not considered here; only the broad-band cases are compared. A power recycling gain of 50 and total loss of 2% are assumed. This means that the sum of the loss in the substrate and the loss in the arm cavities is 2%. The contrast is assumed to be perfect for simplicity.

3.6.1 Loss less case

First we consider the case where there is no loss on the surface of the mirror or in the substrates of the mirror. However, the end mirror's reflectivity is below unity.

The normalized sensitivities of all the optical configurations are the same for the loss-less case. This is because the power in the arm cavities is the same in all the configurations when the signal bandwidth is adjusted to 100 Hz by choosing the finesse of the arm cavities and the reflectivity of the SRM/SEM. Fig. 3.16 shows the normalized sensitivities for the five configurations.

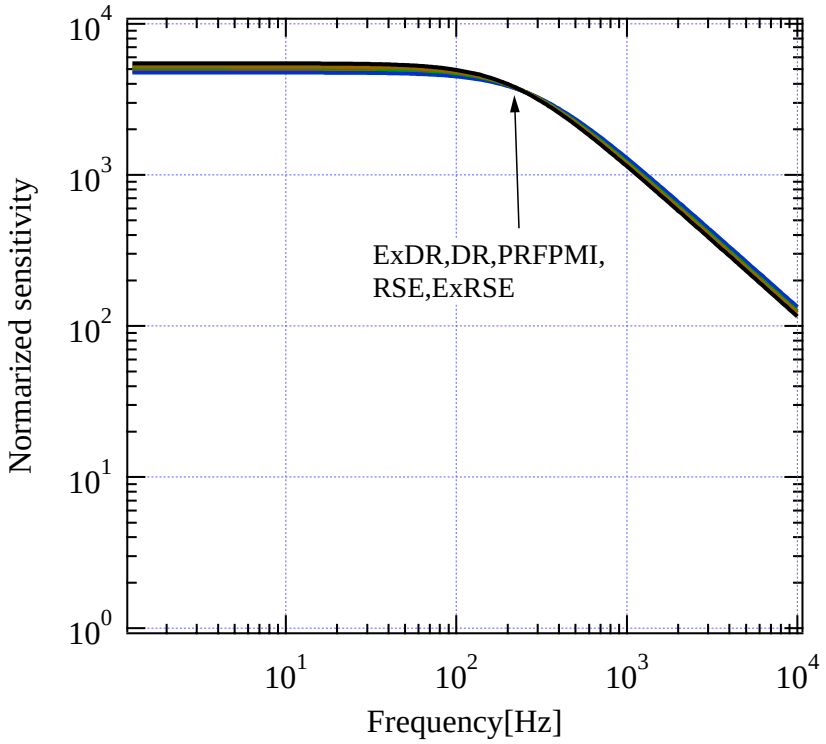

Figure 3.16: Normalized sensitivity of optical configurations in loss-less case. All the curves overlap because they have the same sensitivity.

3.6.2 Loss dominant by mirror-surface loss

We assume that the loss in the substrates of the mirrors is zero, and the loss only exists on the surface of all the mirrors. The reflectivity of the arm cavities is assumed to be 98% due to the loss on the surface of the mirrors. In such a case, the loss on the surface of one mirror is $A_{\rm sur} = 150$ppm.

Fig. 3.17 shows the normalized sensitivity of each configuration for the case of 'loss dominant by the mirror-surface'. There is little difference of the sensitivity among various configurations as shown in the figure. The reason why only the ExDR gives slightly lower sensitivity is that the loss on the surface of the beamsplitter has a non-negligible effect for the ExDR due to the higher circulating power inside the recycling cavity.

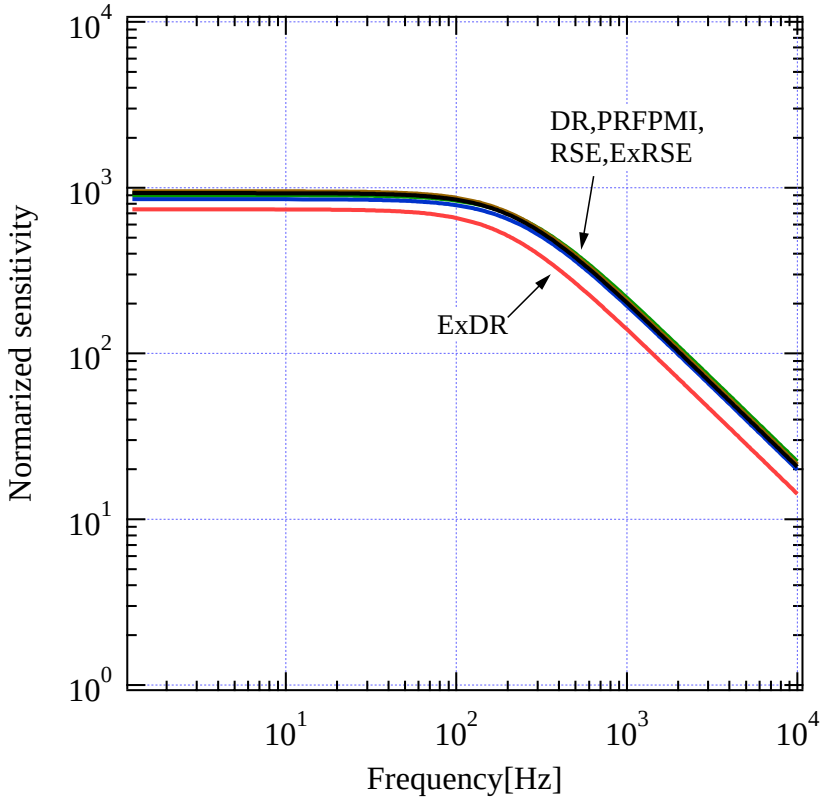

Figure 3.17: Normalized sensitivity of optical configurations with loss dominant by the mirror-surface with $A_{\rm sur} = 150$ppm case. All the sensitivity except for the ExDR overlap.

3.6.3 Loss dominant by substrate loss

In reality the loss of the substrates is predominant. Here, we assume that the loss of the surface is zero, and the loss exists only in the substrates of the mirrors. The term 'substrate' includes the surface with the AR coating and the substrates of the optics such as the beamsplitter and the front mirrors. The loss is assumed to be 2%.

Fig. 3.18 shows the normalized sensitivity of each configurations for the 'loss dominant by the substrate of optics' case. The sensitivity depends on the optical configurations significantly. The sensitivity of ExDR is the worst because the power recycling gain is limited by the loss in the substrates. The same kind of limitation exists in the DR, but the extent of the limitation is less than that for ExDR. Therefore the sensitivity of the DR can be somewhere between that of the PRFPMI and the ExDR, depending on the power recycling gain.

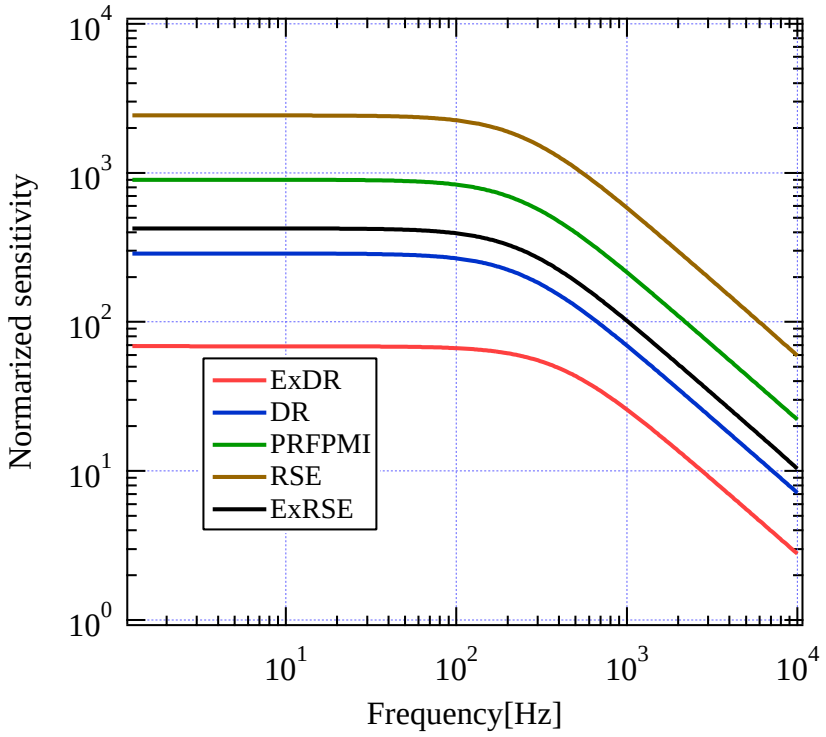

Figure 3.18: Normalized sensitivity of optical configurations for loss dominant by the substrates of the optics with $A_{\rm sub} = 2\%$.

By the same reasoning as above it may be inferred that ExRSE could achieve the highest sensitivity with loss in the substrates, but it is not true. The reason is the following. The reflectivity of the SEC, looking from inside the arm cavity, cannot be adjusted to realize the required signal bandwidth because of the loss existing inside the SEC. As a result the sensitivity of ExRSE is relatively low when the bandwidth is adjusted as same as other configurations by the lower finesse arm cavities. In other words the reflectivity of the SEM which gives the lowest reflectivity of the SEC is equal to $1 - A_{\rm sub}$. With this reflectivity of the SEC, the finesse of the arm cavities necessary to realize the required signal bandwidth is limited below the level necessary for optimum power storage. With this limited finesse of the arm cavities, some light reflects from the cavities, so power recycling can be used. This configuration is by definition not ExRSE but rather RSE.

The DC value of the normalized sensitivity as a function of $A_{\rm sub}$ is shown in Fig. 3.19, when the bandwidth of all the configurations is set to 100 Hz. When parameter $A_{\rm sub}$ is 0.002 in Fig. 3.19, these values correspond to the DC value of

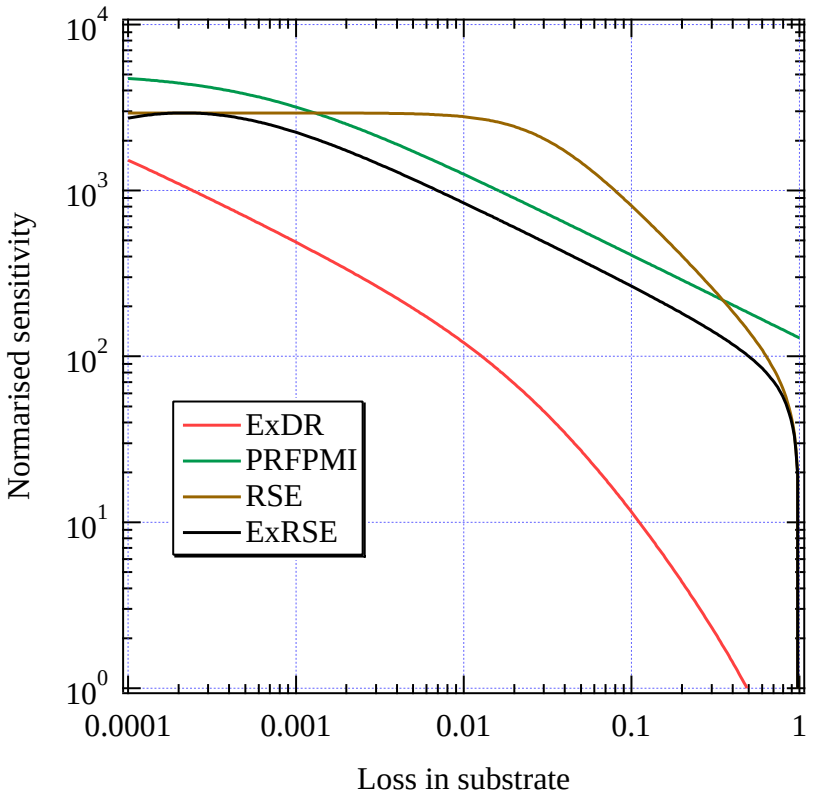

Figure 3.19: DC normalized sensitivity of each optical configurations as a function of loss dominant by substrates of optics. The bandwidth of all configurations is assumed to be 100 Hz.

Fig. 3.18.

3.6.4 limit of arm cavity finesse for RSE

As mentioned above, the arm cavity finesse for the RSE is limited. When the transmissivity of the SEM satisfies the following condition

$$t_{\mathrm{SEM}_0} = A_{\mathrm{sub}}, \tag{3.37}$$

the signal bandwidth is maximized. Under this condition, in order to make the signal bandwidth of RSE equal to the bandwidth of the FPMI (in this case, 100Hz), the reflectivity of the SEC is equal to the reflectivity of the front mirror of the FPMI:

$$r_{\mathrm{SEC}} = r_{\mathrm{F}} \tag{3.38}$$

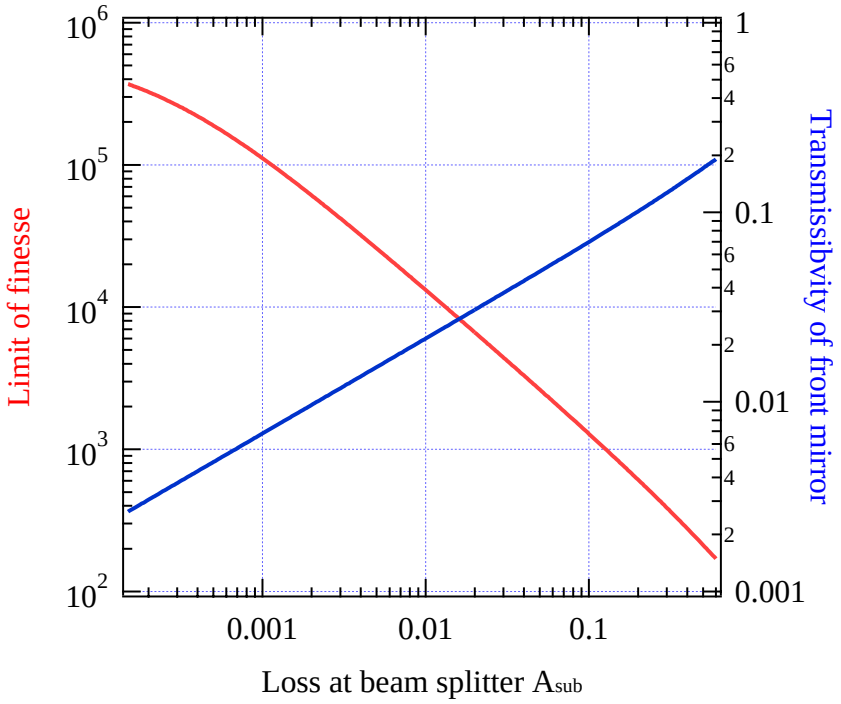

Figure 3.20: Upper limit of the finesse of Fabry-Perot cavity and t_F for the RSE as a function of the substrate loss.

3.7 Conclusion of this chapter

From the condition of Eq. (3.37) and (3.38), the upper limit of the finesse of the Fabry-Perot arm cavity is shown together with the transmissivity of the front mirror t_F in Fig. 3.20 as a function of the loss at the substrates.

This analysis presented in this chapter shows that the configuration that can achieve optimal sensitivity depends on the losses in the interferometer and the location of the losses. With the expected level of loss in optical substrates and coatings, RSE works to be the most promising optimal configuration. In the next chapter we explore control schemes for an RSE interferometer, and in chapter 5 follow with results of a prototype RSE interferometer.

Chapter 4

Signal extraction using Third Harmonic Demodulation (THD)

In the previous chapter, the advantage of RSE has been discussed from the viewpoint of the normalized sensitivity. In this chapter, we introduce a method to control an interferometer with RSE using modulation and demodulation.

A Fabry-Perot Michelson interferometer has the feature that the control signals from the arm cavities tend to dominate the control signal of the Michelson part. This is not an exception for the SEC of the RSE. The SEC is composed of two front mirrors and a signal extraction mirror placed at the anti-symmetric port. The SEC is the most essential cavity for the RSE interferometer. One way to avoid the cross-coupling of the arm cavity signals into the SEC signal is to use a multi-modulation technique. In this method, however, the control system could be considerably complicated and the transmission of the modulation sidebands through the mode cleaner may not be always possible. In this research a totally new signal extraction method to avoid the cross-coupling was developed. The new method is very simple and is free from the problem of the sideband transmission through the mode cleaner. It uses the third harmonic demodulation for the demodulation process of signal extraction of the SEC. The third harmonic demodulation technique was originally developed in a power recycling experiment by Arai [52] to avoid the cross-coupling of the arm cavity signal to the power recycling cavity signal. In this study, we applied the third harmonic demodulation to extract the SEC signal of the RSE interferometer.

In this chapter, we discuss the theory of the third harmonic demodulation for the RSE interferometer.

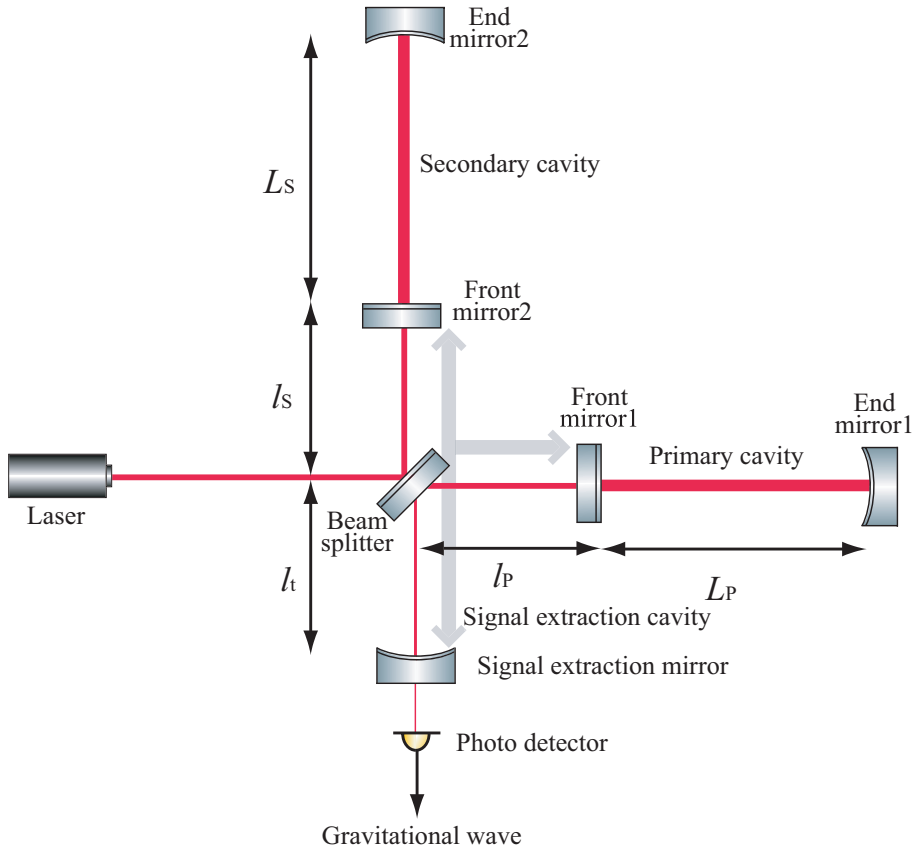

Figure 4.1: RSE interferometer optical configuration and definition of each cavity length. The cavity shown by the gray line is called the signal extraction cavity (SEC).

4.1 Optical configuration of RSE

The optical configuration of a resonant sideband extraction (RSE) interferometer is shown in Fig. 4.1. The RSE interferometer is based on a Fabry-Perot Michelson interferometer (FPMI). The main difference from the FPMI is that the RSE interferometer has an additional mirror called the "signal extraction mirror (SEM)" at the photodetection port where the gravitational wave signal leaks out.

The Fabry-Perot arm cavity in the direction where the incident light is transmitted through the beam splitter is called the "primary cavity", and the other arm cavity in the direction where the incident light is reflected by the beam splitter is called the "secondary cavity". The cavity which is composed of the two front mirrors and the SEM is called the "signal extraction cavity (SEC)". The power recycling mirror is not considered in this chapter because the power recycling technique is not

essential for RSE. We discuss RSE without power recycling in this study as the first step of full RSE with power recycling in the future.

First, we define each length between mirrors in the RSE interferometer. The length of the primary arm cavity and the secondary arm cavity are defined as $L_{\rm P}$ and $L_{\rm S}$. The length between the BS and the FM1, and the length between the BS and the FM2 are defined as $l_{\rm P}$ and $l_{\rm S}$. The length between the BS and the SEM is defined as $l_{\rm t}$.

It is useful to consider a common mode and a differential mode of each length, such as

$$L_{+} = \frac{L_{\rm P} + L_{\rm S}}{2} \tag{4.1}$$

$$L_{-} = \frac{L_{\rm P} - L_{\rm S}}{2} \tag{4.2}$$

$$l_{-} = \frac{l_{\rm P} - l_{\rm S}}{2} \tag{4.3}$$

and the length of the SEC, $l_{\rm s}$, is defined as follows,

$$l_{\rm s} = \frac{l_{\rm P} + l_{\rm S}}{2} + l_{\rm t}, \tag{4.4}$$

4.1.1 Phase description

Carrier phase

In order to describe the condition of the interferometer, we introduce phases which corresponds to each length. The parameter ω_0 is the angular frequency of the carrier of the light.

$$\Phi_{\rm P,0} = \frac{2L_{\rm P}\omega_0}{c} \tag{4.5}$$

$$\Phi_{\rm S,0} = \frac{2L_{\rm S}\omega_0}{c} \tag{4.6}$$

$$\phi_{\rm P,0} = \frac{2l_{\rm P}\omega_0}{c} \tag{4.7}$$

$$\phi_{\rm S,0} = \frac{2l_{\rm S}\omega_0}{c} \tag{4.8}$$

$$\phi_{\rm t,0} = \frac{2l_{\rm t}\omega_0}{c}, \tag{4.9}$$

where the index '$_,0$' means the phase change for the 'carrier'.

Analogous to the length definition, the round-trip phase of the common mode, the differential mode and the SEC can be defined as

$$\Phi_{+,0} = \frac{2L_+\omega_0}{c} \tag{4.10}$$

$$\Phi_{-,0} = \frac{2L_-\omega_0}{c} \tag{4.11}$$

$$\phi_{-,0} = \frac{2l_-\omega_0}{c} \tag{4.12}$$

$$\phi_{\mathrm{s},0} = \frac{2l_\mathrm{s}\omega_0}{c} \tag{4.13}$$

When the arm cavity is in the resonant condition, the round-trip phase is a multiple of 2π

$$\Phi_{+,0} = \Phi_{-,0} = 2n\pi \tag{4.14}$$

When the Michelson length satisfies the condition of the dark fringe at the anti-symmetric port, the phase is a multiple of 2π

$$\phi_{-,0} = 2n\pi \tag{4.15}$$

The phase, $\phi_{s,0}$, is a multiple of 2π in the case of the broad-band RSE,

$$\phi_{\mathrm{s},0} = 2n\pi. \tag{4.16}$$

For the broad-band SR,

$$\phi_{\mathrm{s},0} = (2n+1)\pi, \tag{4.17}$$

and in the detuned case,

$$\phi_{\mathrm{s},0} \neq n\pi. \tag{4.18}$$

Sideband phase

In the next section, we will introduce modulated light in order to extract control signals for each degree of freedom of the interferometer. Modulation generates harmonic sidebands around the carrier. The round trip phase of sidebands with a modulation angular frequency ω_m can be written as follows,

$$\Phi_{+,n} = \frac{2L_+(\omega_0 + n\omega_\mathrm{m})}{c} \tag{4.19}$$

$$\Phi_{-,n} = \frac{2L_-(\omega_0 + n\omega_\mathrm{m})}{c} \tag{4.20}$$

$$\phi_{-,n} = \frac{2l_-(\omega_0 + n\omega_\mathrm{m})}{c} \tag{4.21}$$

$$\phi_{\mathrm{s},n} = \frac{2l_\mathrm{s}(\omega_0 + n\omega_\mathrm{m})}{c} \tag{4.22}$$

where, the index n means nth order (including sign) sideband.

It is convenient to define the round trip phase caused by the first-order sideband in $\phi_{-,n}$ and $\phi_{\mathrm{s},n}$ as follows,

$$\alpha = \frac{2l_-\omega_\mathrm{m}}{c} \tag{4.23}$$

$$\gamma = \frac{2l_\mathrm{s}\omega_\mathrm{m}}{c} \tag{4.24}$$

so, Eq. (4.21),(4.22) are rewritten as a separated form into carrier phase and sideband phase,

$$\phi_{-,n} = \phi_{-,0} + n\alpha \tag{4.25}$$

$$\phi_{\mathrm{s},n} = \phi_{\mathrm{s},0} + n\gamma \tag{4.26}$$

Derivatives of the phase change

Response of the interferometer when it changes from the operational point will be discussed in the next section, so it is necessary to find the derivatives of the phases in order to describe the change of interferometer. Relations of the phase between the common-differential forms and the independent-armed forms are

$$\Phi_+ = \frac{\Phi_\mathrm{P} + \Phi_\mathrm{S}}{2} \tag{4.27}$$

$$\Phi_- = \frac{\Phi_\mathrm{P} - \Phi_\mathrm{S}}{2} \tag{4.28}$$

$$\phi_- = \frac{\phi_\mathrm{P} - \phi_\mathrm{S}}{2} \tag{4.29}$$

$$\phi_\mathrm{s} = \frac{\phi_\mathrm{P} + \phi_\mathrm{S}}{2} + \phi_\mathrm{t} \tag{4.30}$$

so, the derivatives of phase change as the common differential form can be written as

$$\frac{\partial}{\partial\Phi_+} = \left(\frac{\partial}{\partial\Phi_\mathrm{P}} + \frac{\partial}{\partial\Phi_\mathrm{S}}\right) \tag{4.31}$$

$$\frac{\partial}{\partial\Phi_-} = \left(\frac{\partial}{\partial\Phi_\mathrm{P}} - \frac{\partial}{\partial\Phi_\mathrm{S}}\right) \tag{4.32}$$

$$\frac{\partial}{\partial\phi_-} = \left(\frac{\partial}{\partial\phi_\mathrm{P}} - \frac{\partial}{\partial\phi_\mathrm{S}}\right) \tag{4.33}$$

$$\frac{\partial}{\partial\phi_\mathrm{s}} = \frac{1}{2}\left(\frac{\partial}{\partial\phi_\mathrm{P}} + \frac{\partial}{\partial\phi_\mathrm{S}} + \frac{\partial}{\partial\phi_\mathrm{t}}\right) \tag{4.34}$$

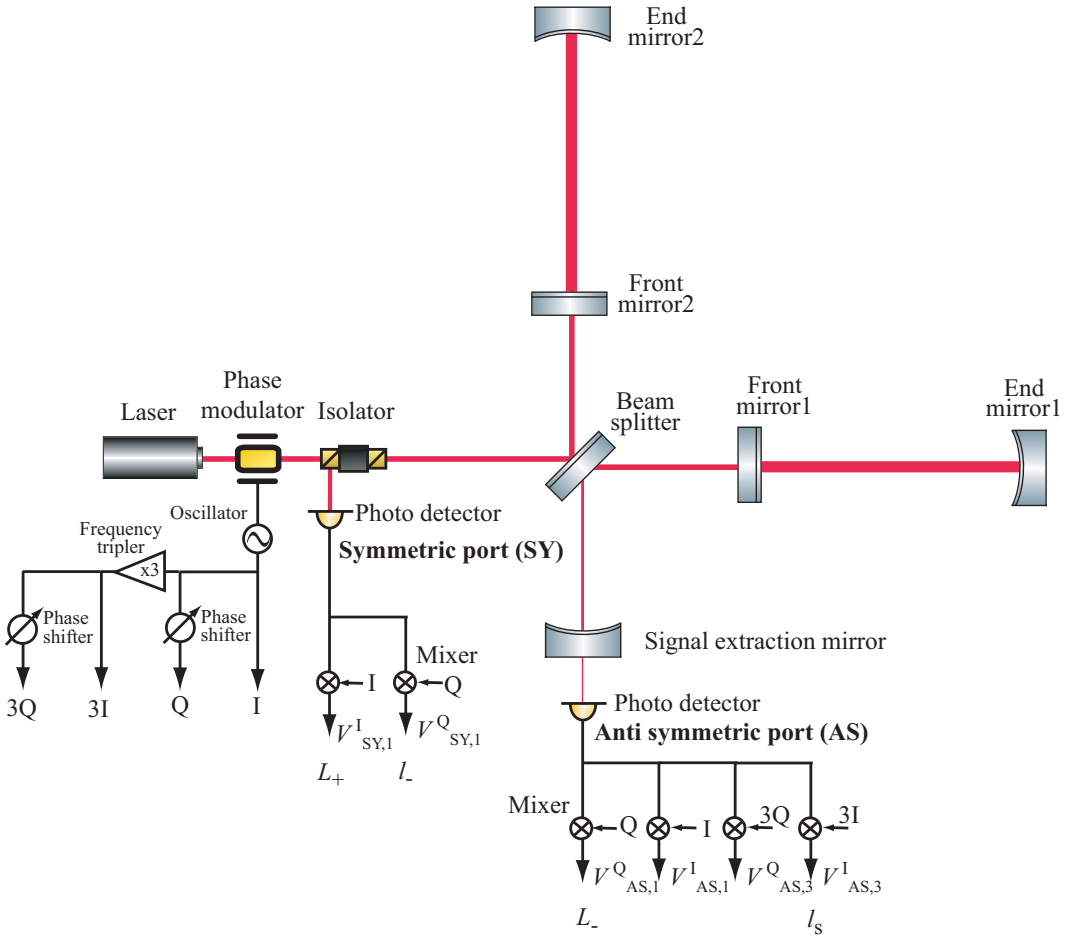

Figure 4.2: Configuration of a signal extraction scheme using phase modulation and demodulation for RSE.

4.2 Modulation and demodulation

The gravitational wave signals and the control signals for the interferometer appear in the phase of light. However, the laser light used for the interferometer is an electro magnetic wave with frequency of hundreds of THz. We do not have photodetectors which can directly detect oscillations at the frequency. The signal which can be detected with the photodetector is actually time average of the amplitude, so the information of the phase of light is lost. Modulation is often used to extract the phase information of light. The Pound-Drever-Hall is a method that uses modulation. In this section, we discuss sidebands generated by the phase modulation, photo detection, and the signal extracted by demodulation.

The configuration of a signal extraction scheme using phase modulation and demodulation of the RSE interferometer is shown in Fig. 4.2. An incident laser is modulated by a phase modulator which is put after the laser. The phase modulator imposes the electric input signal on the optical signal. The light is modulated at frequency $f_{\rm m}$ which is generated by an oscillator. The local oscillator signals for demodulation are also taken from this oscillator. A frequency tripler makes a wave having three times frequency of original wave. This wave is used as a local oscillator for the third harmonic demodulation. There are two photodetection ports. One is placed to detect the reflected light of the interferometer, at the so called "symmetric (SY) port", and the other is to detect the transmitted light of the interferometer, at the so-called "anti-symmetric (AS) port ". For the demodulation phase, "I" means the in-phase demodulation and "Q" means the quadrature-phase demodulation. After the demodulation, the control signals having information of the degree of freedom of the interferometer can be extracted.

4.2.1 Phase modulation

An electric field of the light from the laser $E_{\rm in}$ is written as

$$E_{\rm in} = Ee^{i\omega_0 t}, \tag{4.35}$$

where E is an amplitude of the incident light which has an angular frequency ω_0[radians/second]. The optical power $P_{\rm in}$ is related to the electric field by,

$$P_{\rm in} = |E_{\rm in}|^2 = E^*_{\rm in}E_{\rm in} \tag{4.36}$$

where $E^*_{\rm in}$ denotes the complex conjugate of $E_{\rm in}$, so

$$\begin{aligned} P_{\rm in} &= E^*e^{-i\omega_0 t}Ee^{i\omega_0 t} && (4.37)\\ &= E^*E && (4.38)\\ &= P && (4.39) \end{aligned}$$

This result shows that a measurement of the power P does not give an indication of the instantaneous phase of the field.

When the light is phase modulated with a modulation index m and a modulation frequency $\omega_{\rm m}$, the modulated light $E_{\rm mod}$ is written as

$$E_{\rm mod} = E_{\rm in}e^{im\cos\omega_{\rm m}t} \tag{4.40}$$

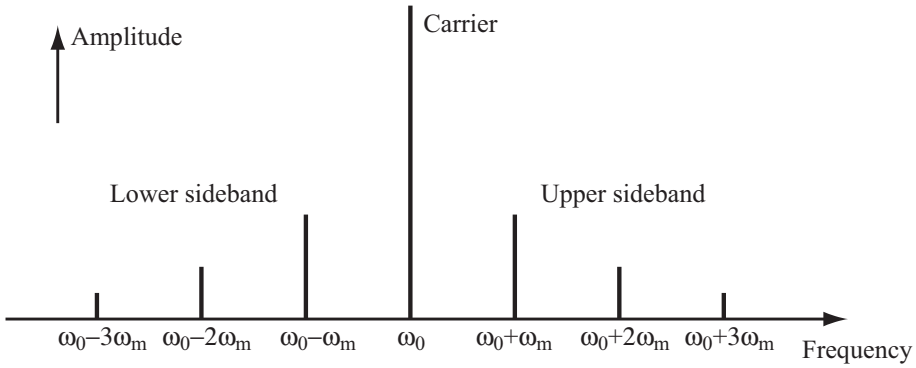

Figure 4.3: Sidebands generated by a phase modulation. The laser beam after phase modulation is composed of the superposition of these sidebands.

Eq. (4.40) is expanded as Bessel function $J_n(m)$ as

$$E_{\mathrm{mod}} = E_{\mathrm{in}} \sum_{n=-\infty}^{\infty} i^n J_n(m) e^{in\omega_{\mathrm{m}}t} \tag{4.41}$$

Eq. (4.41) shows that the laser beam after phase modulation is composed of the superposition of beams with angular frequencies of $\omega_0 + n\omega_{\mathrm{m}}$ (see Fig. 4.3).

The amplitude of the nth ($\neq 0$) order sidebands E_n which include the carrier frequency is defined as

$$E_n = i^n J_n(m) E_{\mathrm{in}} \tag{4.42}$$

when $n = 0$, Eq. (4.42) corresponds to the electric field of carrier after the phase modulation. Then Eq. (4.41) is rewritten as a sum of the carrier and nth ($\neq 0$) order sidebands,

$$E_{\mathrm{mod}} = \sum_{n=-\infty}^{\infty} E_n e^{in\omega_{\mathrm{m}}t} \tag{4.43}$$

The following relations are useful for the subsequent section.

$$J_{-n}(m) = (-1)^n J_n(m) \tag{4.44}$$

$$i^{-n} = (-1)^n i^n \tag{4.45}$$

$$E_{-n} = E_n \tag{4.46}$$

4.2.2 Photo detection

The phase modulated light E_{mod} experiences amplitude and phase changes while travelling in the interferometer. These changes of the carrier ($n = 0$) and the nth

order sideband ($n \neq 0$) are defined as phase change parameters x_n. The nth order component of amplitude and phase changed light $E_{\mathrm{PD}n}$ received by a photodetector can be written with the initial amplitude E_n and the phase change parameter x_n as

$$E_{\mathrm{PD}n} = x_n E_n, \tag{4.47}$$

so the electric field just before the photodetector is given by sum of $E_{\mathrm{PD}n}$ as

$$E_{\mathrm{PD}} = \sum_{n=-\infty}^{\infty} E_{\mathrm{PD}_n} \tag{4.48}$$

After the light has been detected by the photodetector, the photodetector generates the photocurrent. The $e^{in\omega_{\mathrm{m}}t}$ component of the photocurrent is written as

$$I_n = \sum_{m=-\infty}^{\infty} I_{n,m} \tag{4.49}$$

$$I_{n,m} = E_{\mathrm{PD}_m} E^*_{\mathrm{PD}_{m-n}} \tag{4.50}$$

The photocurrent is given by sum of I_n as

$$I = \eta \sum_{n=0}^{\infty} I_n e^{in\omega_{\mathrm{m}}t} = \eta \sum_{n=-\infty}^{\infty} \sum_{m=-\infty}^{\infty} I_{n,m} e^{in\omega_{\mathrm{m}}t} \tag{4.51}$$

where η[A/W] is the efficiency of the photodetector.

Consider some concrete examples of the photocurrent here. For simplicity, we will sidebands with order higher than four for the remainder of this discussion.

First, the DC component of the photocurrent is written as

$$I_0 = \sum_{n=-3}^{3} I_{0,n}, \tag{4.52}$$

concretely,

$$\begin{aligned} I_0 &= \sum_{n=-3}^{3} E_{\mathrm{PD}_n} E^*_{\mathrm{PD}_n} \\ &= \sum_{n=-3}^{3} |x_n|^2 |E_n|^2 \\ &= \sum_{n=-3}^{3} |x_n|^2 J_n^2(m) |E_{\mathrm{in}}|^2 \end{aligned} \tag{4.53}$$

Next the $e^{i\omega_{\mathrm{m}}t}$ component of the photocurrent is

$$I_1 = \sum_{n=-2}^{3} I_{1,n} \tag{4.54}$$

here, it is convenient to separate to $E_{-1}E_0, E_0E_1$ as $I_{1\mathrm{a}}$ and $E_{-2}E_{-1}, E_1E_2$ as $I_{1\mathrm{b}}$. This is because the $e^{i3\omega_{\mathrm{m}}t}$ component has $E_{-3}E_0, E_0E_3$ and $E_{-2}E_1, E_{-1}E_2$. If the $e^{i\omega_{\mathrm{m}}t}$ component is separated as such, the $e^{i\omega_{\mathrm{m}}t}$ component can be easily compared with the $e^{i3\omega_{\mathrm{m}}t}$. Moreover, $E_{-3}E_{-2}, E_2E_3$ component remains but it can be negligible because it is small compared with $E_{-1}E_0, E_0E_1$.

$$\begin{aligned} I_{1\mathrm{a}} &= I_{1,0} + I_{1,1} \\ &= E^*_{\mathrm{PD}_{-1}} E_{\mathrm{PD}_0} + E^*_{\mathrm{PD}_0} E_{\mathrm{PD}_1} \\ &= (x^*_{-1}x_0 - x^*_0 x_1)(-i)J_0(m)J_1(m)|E_{\mathrm{in}}|^2 \end{aligned} \tag{4.55}$$

$$\begin{aligned} I_{1\mathrm{b}} &= I_{1,-1} + I_{1,2} \\ &= E^*_{\mathrm{PD}_{-2}} E_{\mathrm{PD}_{-1}} + E^*_{\mathrm{PD}_1} E_{\mathrm{PD}_2} \\ &= (x^*_{-2}x_{-1} - x^*_1 x_2)(-i)J_1(m)J_2(m)|E_{\mathrm{in}}|^2 \end{aligned} \tag{4.56}$$

The second-order component is not discussed here because it is known that the second harmonic demodulation does not produce any useful signals. The $e^{i3\omega_{\mathrm{m}}t}$ component is written as

$$I_3 = \sum_{n=0}^{3} I_{3,n} \tag{4.57}$$

It is convenient to separate the form of I_3 as $I_{3\mathrm{a}}$ with $E_{-3}E_0, E_0E_3$ and $I_{3\mathrm{b}}$ with $E_{-2}E_1, E_{-1}E_2$ just the same as for I_1.

$$\begin{aligned} I_{3\mathrm{a}} &= I_{3,0} + I_{3,3} \\ &= E^*_{\mathrm{PD}_{-3}} E_{\mathrm{PD}_0} + E^*_{\mathrm{PD}_0} E_{\mathrm{PD}_3} \\ &= (x^*_{-3}x_0 - x^*_0 x_3)iJ_0(m)J_3(m)|E_{\mathrm{in}}|^2 \end{aligned} \tag{4.58}$$

$$\begin{aligned} I_{3\mathrm{b}} &= I_{3,1} + I_{3,2} \\ &= E^*_{\mathrm{PD}_{-2}} E_{\mathrm{PD}_1} + E^*_{\mathrm{PD}_{-1}} E_{\mathrm{PD}_2} \\ &= (x^*_{-2}x_1 - x^*_{-1} x_2)(-i)J_1(m)J_2(m)|E_{\mathrm{in}}|^2 \end{aligned} \tag{4.59}$$

4.2.3 Demodulation

The $e^{in\omega_{\mathrm{m}}t}$ component of the photocurrent is extracted by the nth order demodulation. The demodulation has two processes, mixing and filtering. The photocurrent

is multiplied with the local oscillator by a mixer. The mixer down-converts $n\omega_{\rm m}$ components to DC region with an nth order local oscillator. The excessive higher frequency components are excluded by low pass filtering. The process of mixing and low pass filtering can be mathematically described as a product with a cosine or sine at the demodulation frequency $n\omega_{\rm m}$, which is then averaged over period T, equal to the period of the modulation.

When $\cos n\omega_{\rm m}t$ is used as a local oscillator, the signal obtained by demodulation is called "in(I)-phase" signal,

$$\begin{aligned} V^{\rm I}_{{\rm PD},n} &= \frac{g_{\rm det}}{T}\int_{t-T}^{t} I(t')\cos n\omega_{\rm m}t'dt' \\ &= \frac{g_{\rm det}}{2}(I_n + I_{-n}) \\ &= g_{\rm det}{\rm Re}[I_n] \end{aligned} \tag{4.60}$$

and when $\sin n\omega_{\rm m}t$ is used, the signal is called "quadrature(Q)-phase" signal,

$$\begin{aligned} V^{\rm Q}_{{\rm PD},n} &= \frac{g_{\rm det}}{T}\int_{t-T}^{t} I(t')\sin n\omega_{\rm m}t'dt' \\ &= \frac{g_{\rm det}}{2}(-I_n + I_{-n}) \\ &= -g_{\rm det}{\rm Im}[I_n] \end{aligned} \tag{4.61}$$

where index PD denotes the name of the port expressed as 'SY' or 'AS' in Fig. 4.2. Parameter $g_{\rm det}$ is the gain of the demodulation including the efficiency of photodetection and the demodulator. Eq. (4.60) and (4.61) show that the real and imaginary part of $I(t)$ can be extracted independently.

In general, a local oscillator which has a demodulation phase of $\theta_{\rm dem}$ is written as

$$\cos(n\omega_{\rm m}t + \theta_{\rm dem}) = \cos n\omega_{\rm m}t\sin\theta_{\rm dem} - \sin n\omega_{\rm m}t\cos\theta_{\rm dem} \tag{4.62}$$

so the demodulated signal is given as

$$\begin{aligned} V^{\theta_{\rm dem}}_{{\rm PD},n} &= \frac{g_{\rm det}}{T}\int_{t-T}^{t} I(t')\cos(n\omega_{\rm m}t' + \theta_{\rm dem})dt' \\ &= V^{\rm I}_n\cos\theta_{\rm dem} - V^{\rm Q}_n\sin\theta_{\rm dem} \end{aligned} \tag{4.63}$$

This result shows that the signal is a linear combination of Eq. (4.60) and (4.61).

It is useful to write the demodulated signal corresponding to $I_{\rm 1a}$ and $I_{\rm 1b}$ etc.

First-order demodulation

$$\begin{aligned} V^{\mathrm{I}}_{\mathrm{PD,1a}} &= \frac{g_{\mathrm{det}}}{T}\int_{t-T}^{t} I_{\mathrm{1a}}(t')\cos\omega_{\mathrm{m}}t'dt' \\ &= g_{\mathrm{det}}\mathrm{Re}[I_{\mathrm{1a}}] \\ &= g_{\mathrm{det}}\mathrm{Im}[(x^*_{-1}x_0 - x^*_0x_1)]J_0(m)J_1(m)|E_{\mathrm{in}}|^2 \end{aligned} \tag{4.64}$$

$$\begin{aligned} V^{\mathrm{Q}}_{\mathrm{PD,1a}} &= \frac{g_{\mathrm{det}}}{T}\int_{t-T}^{t} I_{\mathrm{1a}}(t')\sin\omega_{\mathrm{m}}t'dt' \\ &= -g_{\mathrm{det}}\mathrm{Im}[I_{\mathrm{1a}}] \\ &= g_{\mathrm{det}}\mathrm{Re}[(x^*_{-1}x_0 - x^*_0x_1)]J_0(m)J_1(m)|E_{\mathrm{in}}|^2 \end{aligned} \tag{4.65}$$

$$V^{\mathrm{I}}_{\mathrm{PD,1b}} = g_{\mathrm{det}}\mathrm{Im}[(x^*_{-2}x_{-1} - x^*_1x_2)]J_1(m)J_2(m)|E_{\mathrm{in}}|^2 \tag{4.66}$$

$$V^{\mathrm{Q}}_{\mathrm{PD,1b}} = g_{\mathrm{det}}\mathrm{Re}[(x^*_{-2}x_{-1} - x^*_1x_2)]J_1(m)J_2(m)|E_{\mathrm{in}}|^2 \tag{4.67}$$

Third-order demodulation

$$\begin{aligned} V^{\mathrm{I}}_{\mathrm{PD,3a}} &= \frac{g_{\mathrm{det}}}{T}\int_{t-T}^{t} I_{\mathrm{3a}}(t')\cos 3\omega_{\mathrm{m}}t'dt' \\ &= -g_{\mathrm{det}}\mathrm{Im}[(x^*_{-3}x_0 - x^*_0x_3)]J_0(m)J_3(m)|E_{\mathrm{in}}|^2 \end{aligned} \tag{4.68}$$

$$\begin{aligned} V^{\mathrm{Q}}_{\mathrm{PD,3a}} &= \frac{g_{\mathrm{det}}}{T}\int_{t-T}^{t} I_{\mathrm{3a}}(t')\sin 3\omega_{\mathrm{m}}t'dt' \\ &= -g_{\mathrm{det}}\mathrm{Re}[(x^*_{-3}x_0 - x^*_0x_3)]J_0(m)J_3(m)|E_{\mathrm{in}}|^2 \end{aligned} \tag{4.69}$$

$$V^{\mathrm{I}}_{\mathrm{PD,3b}} = g_{\mathrm{det}}\mathrm{Im}[(x^*_{-2}x_1 - x^*_{-1}x_2)]J_1(m)J_2(m)|E_{\mathrm{in}}|^2 \tag{4.70}$$

$$V^{\mathrm{Q}}_{\mathrm{PD,3b}} = g_{\mathrm{det}}\mathrm{Re}[(x^*_{-2}x_1 - x^*_{-1}x_2)]J_1(m)J_2(m)|E_{\mathrm{in}}|^2 \tag{4.71}$$

These results will be used later in Sec. 4.4.2

4.3 Response of the RSE interferometer

In this section, we discuss the static response of interferometer in order to prepare for considering the derivative response of interferometer in the next section. Parameter x_n defined in Eq. (4.47) represents the response of the interferometer and it is described as an amplitude transmissivity or an amplitude reflectivity including the phase information of the interferometer.

4.3.1 Fabry-Perot cavity

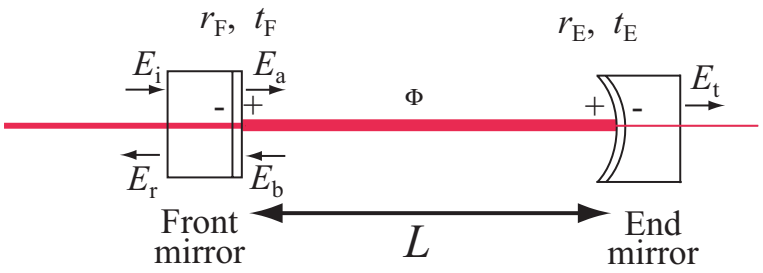

Figure 4.4: Electric fields of the Fabry-Perot cavity.

First, we start to analyze the static response of a Fabry-Perot cavity. Electric fields of the Fabry-Perot cavity are shown in Fig. 4.4. Relations of these electric fields can be written as

$$\begin{aligned} E_a &= t_F E_i + r_F E_b \\ E_t &= t_E e^{i\frac{-L\omega_0}{c}} E_a \\ E_b &= r_E e^{i\frac{-2L\omega_0}{c}} E_a \\ E_r &= -r_F E_i + t_F E_b, \end{aligned} \tag{4.72}$$

where L is the length of the Fabry-Perot cavity, and ω_0 is an angular frequency of incident light. Parameter r and t are a reflectivity and a transmissivity of mirrors. Index 'F' and 'E' mean a front mirror and a end mirror.

A round-trip phase of the Fabry-Perot cavity is defined as

$$\Phi = \frac{2L\omega_0}{c}. \tag{4.73}$$

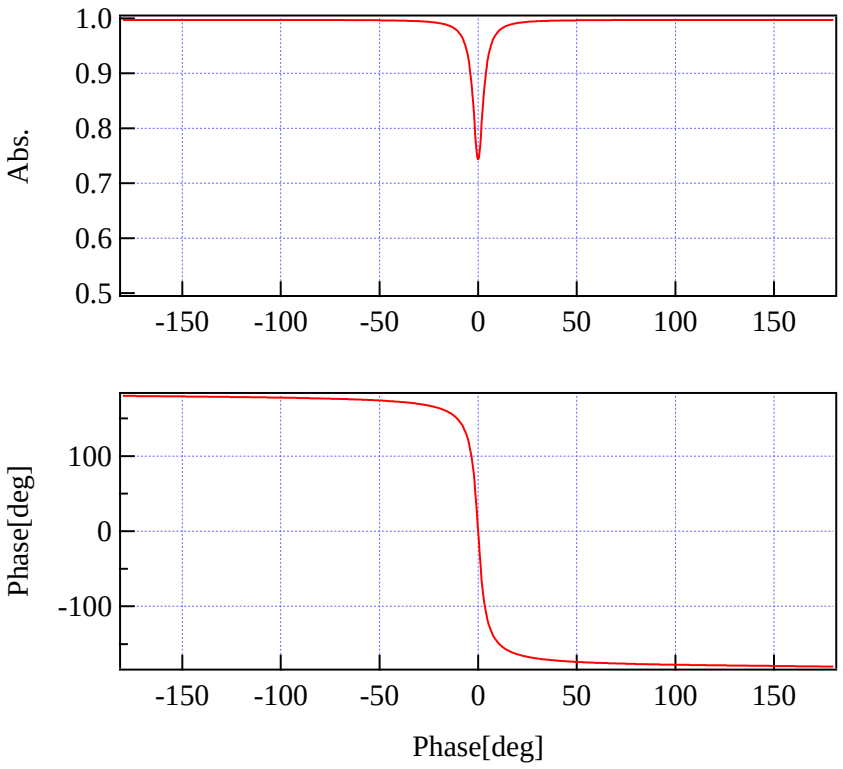

Figure 4.5: Absolute value and phase of $r_{\rm cav}$ as a function of Φ.

From Eq. (4.72) and Eq. (4.73), a reflectivity $r_{\rm cav}$, a transmissivity $t_{\rm cav}$ and a power enhancement $g_{\rm cav}$ of the Fabry-Perot cavity are defined as

$$r_{\rm cav}(\Phi) = \frac{E_{\rm r}}{E_{\rm i}} = -r_{\rm F} + \frac{t_{\rm F}^2 r_{\rm E} e^{-i\Phi}}{1 - r_{\rm F} r_{\rm E} e^{-i\Phi}} \tag{4.74}$$

$$t_{\rm cav}(\Phi) = \frac{E_{\rm t}}{E_{\rm i}} = \frac{t_{\rm F} t_{\rm E} e^{-i\Phi/2}}{1 - r_{\rm F} r_{\rm E} e^{-i\Phi}} \tag{4.75}$$

$$g_{\rm cav}(\Phi) = \frac{E_{\rm a}}{E_{\rm i}} = \frac{t_{\rm F}}{1 - r_{\rm F} r_{\rm E} e^{-i\Phi}}. \tag{4.76}$$

For the following calculation, we write the differentiated form of the reflectivity of Fabry-Perot cavity. The derivative of Eq. (4.74) by the phase is given as

$$r'_{\rm cav}(\Phi) \equiv \frac{\partial}{\partial\Phi} r_{\rm cav}(\Phi) = \frac{-i t_{\rm F}^2 r_{\rm E} e^{-i\Phi}}{(1 - r_{\rm F} r_{\rm E} e^{-i\Phi})^2}. \tag{4.77}$$

The absolute value and the phase of $r_{\rm cav}(\Phi)$ are shown in Fig. 4.5. The phase of the reflected light of Fabry-Perot cavity changes rapidly around the resonant point. When $\Phi = 2n\pi$, the Fabry-Perot cavity is resonant, and the reflectivity at the resonant point $r_{\rm reso}$ is defined as

$$r_{\rm reso} \equiv r_{\rm cav}(2n\pi) = -r_{\rm F} + \frac{t_{\rm F}^2 r_{\rm E}}{1 - r_{\rm F} r_{\rm E}} > 0 \tag{4.78}$$

and when $\Phi = (2n+1)\pi$, the Fabry-Perot cavity is anti resonant, and the reflectivity at anti resonant condition $r_{\rm anti}$ is defined as

$$r_{\rm anti} \equiv r_{\rm cav}((2n+1)\pi) = -r_{\rm F} + \frac{t_{\rm F}^2 r_{\rm E}}{1 + r_{\rm F} r_{\rm E}} < 0. \tag{4.79}$$

The derivatives of Eq. (4.78) and Eq. (4.79) by the phase are given as

$$r'_{\rm reso} \equiv r'_{\rm cav}(2n\pi) = \frac{-i t_{\rm F}^2 r_{\rm E}}{(1 - r_{\rm F} r_{\rm E})^2} \tag{4.80}$$

$$r'_{\rm anti} \equiv r'_{\rm cav}((2n+1)\pi) = \frac{-i t_{\rm F}^2 r_{\rm E}}{(1 + r_{\rm F} r_{\rm E})^2}. \tag{4.81}$$

In the conventional interferometer, the end mirror reflectivity is chosen to be high ($r_{\rm E} \approx 1$), and the reflectivity of the front mirror is selected to be slightly less than that of the end mirror. In this case, we can approximate that $r_{\rm reso}$ is slightly less than 1, $r_{\rm anti} \approx -r_{\rm F}$, and $|r'_{\rm reso}| \gg 1 \gg |r'_{\rm anti}|$.

4.3.2 Fabry-Perot Michelson Interferometer

Next, we discuss the static response of Fabry-Perot Michelson Interferometer. Fig. 4.6 shows electric fields around the beam splitter. As for the Fabry-Perot cavity part, the response discussed in the previous section is applied. A light entering the beam splitter from the symmetric port with an electric field $E_{\rm i}$ returns again to the symmetric port with $E_{\rm SY}$ and goes out into the anti-symmetric port $E_{\rm AS}$. Moreover, we consider another input light $E_{\rm i_s}$ coming from the anti-symmetric port.

If the whole Fabry-Perot Michelson Interferometer is regarded as a compound mirror, the reflectivities and the transmissivities of compound mirror are defined. It must be noted that the light experiences the phase change defined by Eq. (4.7)∼Eq. (4.9) when light goes along each pass of $l_{\rm P}$, $l_{\rm S}$, and $l_{\rm t}$. We assume that the beam splitter divides the light into 50 : 50, and it has no loss. The reflectivities and the transmissivities of each port of the compound mirror are given as follows,

$$r_{\rm com_r} = \frac{E_{\rm SY}}{E_{\rm i}}$$

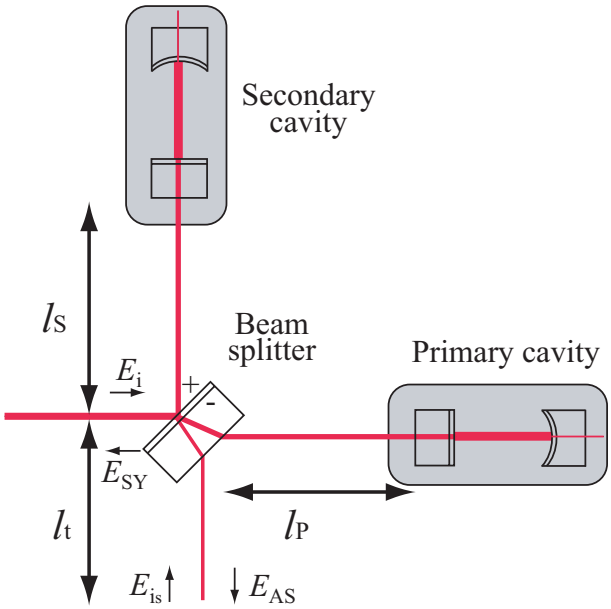

Figure 4.6: Electric fields around the beamsplitter of a Fabry-Perot Michelson interferometer.

$$= r_{cav}(\Phi_S)e^{-i\phi_S} + r_{cav}(\Phi_P)e^{-i\phi_P} \tag{4.82}$$

$$\begin{aligned} t_{com_r} &= \frac{E_{AS}}{E_i} \\ &= r_{cav}(\Phi_S)e^{-i(\phi_S+\phi_t/2)} - r_{cav}(\Phi_P)e^{-i(\phi_P+\phi_t/2)} \end{aligned} \tag{4.83}$$

$$\begin{aligned} r_{com_t} &= \frac{E_{AS}}{E_{i_s}} \\ &= r_{cav}(\Phi_S)e^{-i(\phi_t+\phi_S)} + r_{cav}(\Phi_P)e^{-i(\phi_t+\phi_P)} \end{aligned} \tag{4.84}$$

$$\begin{aligned} t_{com_t} &= \frac{E_{SY}}{E_{i_s}} \\ &= r_{cav}(\Phi_S)e^{-i(\phi_t/2+\phi_S)} - r_{cav}(\Phi_P)e^{-i(\phi_t/2+\phi_P)}, \end{aligned} \tag{4.85}$$

where the index 'com' means compound mirror, 't' means a transmitted port, and 'r' means a reflected port.

The reflectivities of Fabry-Perot cavity at the operating point $r_{,n}$ for the carrier $(n = 0)$ and for the nth $(n \neq 0)$ order sidebands are expressed as

$$r_{,n} = \begin{cases} r_{reso} & (n = 0) \\ r_{anti} & (n \neq 0) \end{cases}$$

that is, the Fabry-Perot cavity is assumed to be resonant for the carrier, and anti-resonant for the sidebands at the operating point. Moreover, in order to maintain the bright-dark condition of Michelson interferometer, $\phi_{\rm P}$ and $\phi_{\rm S}$ satisfy

$$\phi_- = \frac{\phi_{\rm P} - \phi_{\rm S}}{2} = 2n\pi \tag{4.86}$$

and in order to deal with $\phi_{\rm t}$ independently, $\phi_{\rm P}$ and $\phi_{\rm S}$ are assumed to satisfy

$$\frac{\phi_{\rm P} + \phi_{\rm S}}{2} = 2n\pi \tag{4.87}$$

at the operating point.

Then, Eq. (4.82)∼Eq. (4.85) are simplified as

$$\begin{aligned}
r_{{\rm com_r},n} &= r_{,n}\cos(n\alpha) && (4.88)\\
t_{{\rm com_r},n} &= -ir_{,n}\sin(n\alpha)e^{-i\frac{\phi_{\rm t}+n\gamma}{2}} && (4.89)\\
r_{{\rm com_t},n} &= r_{,n}\cos(n\alpha)e^{-i(\phi t+n\gamma)} && (4.90)\\
t_{{\rm com_t},n} &= -ir_{,n}\sin(n\alpha)e^{-i\frac{\phi_{\rm t}+n\gamma}{2}}. && (4.91)
\end{aligned}$$

In addition, we write the derivatives, when Eq. (4.82)∼Eq. (4.85) are differentiated with Φ_+,Φ_-,ϕ_-,$\phi_{\rm s}$, respectively, for the carrier ($n = 0$) and the sidebands ($n \neq 0$).

$$\begin{aligned}
\frac{\partial}{\partial\Phi_+}r_{{\rm com_r},n} &= r'_{,n}\cos(n\alpha) && (4.92)\\
\frac{\partial}{\partial\Phi_+}t_{{\rm com_r},n} &= -ir'_{,n}\sin(n\alpha)e^{-i\frac{\phi_{\rm t}+n\gamma}{2}} && (4.93)\\
\frac{\partial}{\partial\Phi_+}r_{{\rm com_t},n} &= r'_{,n}\cos(n\alpha)e^{-i(\phi t+n\gamma)} && (4.94)\\
\frac{\partial}{\partial\Phi_+}t_{{\rm com_t},n} &= -ir'_{,n}\sin(n\alpha)e^{-i\frac{\phi_{\rm t}+n\gamma}{2}} && (4.95)
\end{aligned}$$

$$\begin{aligned}
\frac{\partial}{\partial\Phi_-}r_{{\rm com_r},n} &= -ir'_{,n}\sin(n\alpha) && (4.96)\\
\frac{\partial}{\partial\Phi_-}t_{{\rm com_r},n} &= r'_{,n}\cos(n\alpha)e^{-i\frac{\phi_{\rm t}+n\gamma}{2}} && (4.97)\\
\frac{\partial}{\partial\Phi_-}r_{{\rm com_t},n} &= -ir'_{,n}\sin(n\alpha)e^{-i(\phi t+n\gamma)} && (4.98)\\
\frac{\partial}{\partial\Phi_-}t_{{\rm com_t},n} &= r'_{,n}\cos(n\alpha)e^{-i\frac{\phi_{\rm t}+n\gamma}{2}} && (4.99)
\end{aligned}$$

$$\frac{\partial}{\partial\phi_-}r_{\mathrm{com_r},n} = -r_{,n}\sin(n\alpha) \tag{4.100}$$
$$\frac{\partial}{\partial\phi_-}t_{\mathrm{com_r},n} = -ir_{,n}\cos(n\alpha)e^{-i\frac{\phi_\mathrm{t}+n\gamma}{2}} \tag{4.101}$$
$$\frac{\partial}{\partial\phi_-}r_{\mathrm{com_t},n} = -r_{,n}\sin(n\alpha)e^{-i(\phi t+n\gamma)} \tag{4.102}$$
$$\frac{\partial}{\partial\phi_-}t_{\mathrm{com_t},n} = -ir_{,n}\cos(n\alpha)e^{-i\frac{\phi_\mathrm{t}+n\gamma}{2}} \tag{4.103}$$

$$\frac{\partial}{\partial\phi_s}r_{\mathrm{com_r},n} = 0 \tag{4.104}$$
$$\frac{\partial}{\partial\phi_s}t_{\mathrm{com_r},n} = -\frac{i}{2}r_{,n}\sin(n\alpha)e^{-i\frac{\phi_\mathrm{t}+n\gamma}{2}} \tag{4.105}$$
$$\frac{\partial}{\partial\phi_s}r_{\mathrm{com_t},n} = -ir_{,n}\cos(n\alpha)e^{-i(\phi t+n\gamma)} \tag{4.106}$$
$$\frac{\partial}{\partial\phi_s}t_{\mathrm{com_t},n} = -\frac{i}{2}r_{,n}\sin(n\alpha)e^{-i\frac{\phi_\mathrm{t}+n\gamma}{2}}, \tag{4.107}$$

where Eq. (4.31)$\sim$Eq. (4.34) are used to obtain derivatives from Φ_P,Φ_S,ϕ_P,ϕ_S,ϕ_t to Φ_+,Φ_-,ϕ_-,ϕ_s.

4.3.3 RSE

Fig. 4.7 shows the electric field of an RSE interferometer. The RSE interferometer forms a cavity composed of a Fabry-Perot Michelson interferometer and a signal extraction mirror (SEM). The response described in 4.3.2 is applied to the Fabry-Perot Michelson interferometer part. Here, the port to which the input light returns from the RSE interferometer is called the 'symmetric (SY)' port and the port to which the input light goes through is called the 'anti-symmetric (AS)' port.

The response of the RSE interferometer is obtained by solving the following simultaneous equations,

$$\begin{aligned} E_\mathrm{so} &= t_{\mathrm{com_t}}E_\mathrm{in} + r_{\mathrm{com_t}}E_\mathrm{si} \\ E_\mathrm{tr} &= t_\mathrm{s}E_\mathrm{so} \\ E_\mathrm{si} &= r_\mathrm{s}E_\mathrm{so} \\ E_\mathrm{ref} &= t_{\mathrm{com_r}}E_\mathrm{si} + r_{\mathrm{com_r}}E_\mathrm{in}. \end{aligned} \tag{4.108}$$

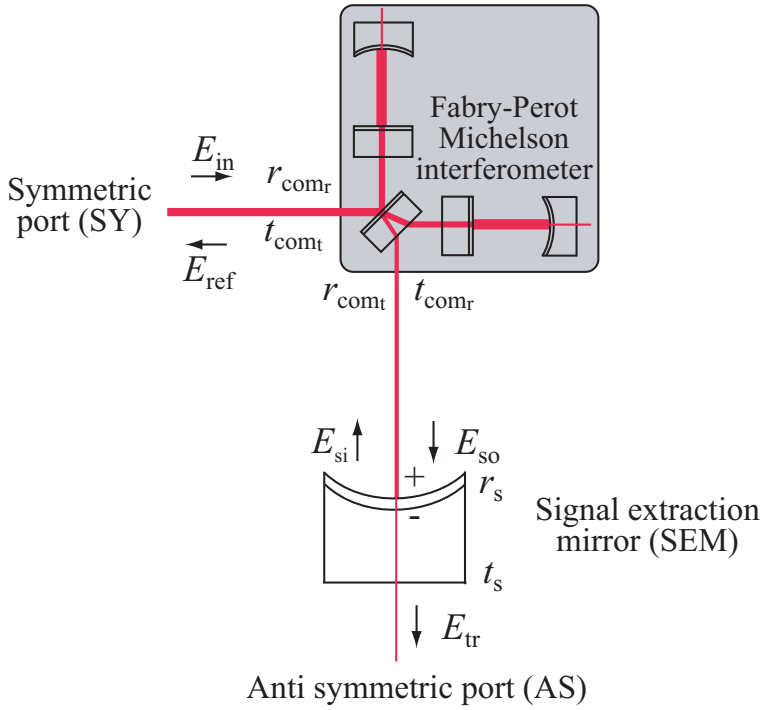

Figure 4.7: Electric fields of an RSE interferometer. The RSE interferometer forms a cavity composed of a Fabry-Perot Michelson interferometer and a signal extraction mirror (SEM). The Fabry-Perot Michelson interferometer is described as a black box which has two inputs and two outputs.

Because all the phase changes are experienced in the Fabry-Perot Michelson interferometer part, we don't need to consider the phase change here. $E_{\rm in}$ shows the amplitude of input light, $E_{\rm ref}$ shows the light at symmetric port, and $E_{\rm tr}$ shows the light at anti-symmetric port. $E_{\rm si}$ exists because there is a signal extraction mirror (SEM). $E_{\rm si}$ is the light which enters again into the Fabry-Perot Michelson interferometer from the anti-symmetric port side. $E_{\rm si}$ sees the reflectivity and transmissivity of the Fabry-Perot Michelson interferometer as calculated in Eq. (4.84),(4.85).

An input light which enters from the symmetric port as $E_{\rm in}$ returns to the symmetric port as $E_{\rm ref}$, and goes to the anti-symmetric port as $E_{\rm tr}$. The ratio in that case is defined as a reflectivity $r_{\rm RSE}$ of the RSE and a transmissivity $t_{\rm RSE}$ of the RSE respectively,

$$r_{\rm RSE} \equiv \frac{E_{\rm ref}}{E_{\rm in}} = r_{\rm com_r} + \frac{t_{\rm com_r} r_{\rm t} t_{\rm com_t}}{1 - r_{\rm com_t} r_{\rm s}} \tag{4.109}$$

$$t_{\mathrm{RSE}} \equiv \frac{E_{\mathrm{tr}}}{E_{\mathrm{in}}} = \frac{t_{\mathrm{com_r}} t_{\mathrm{s}}}{1 - r_{\mathrm{com_t}} r_{\mathrm{s}}}. \tag{4.110}$$

4.4 Signal extraction

According to the static response which has been discussed in the previous section, we can find the derivative to the phase in this section. If the phase change is small enough from the operating point of the interferometer, it shows a linear response. Therefore, the magnitude of these derivatives will be on error signals to control the degrees of freedom.

As shown in Fig. 4.2, one photodetector is placed at the symmetric port, and another photo detector is placed at the anti-symmetric port. We concretely find the signals demodulated with in-phase and quadrature-phase from each port. As for the anti-symmetric port, we will find the signal demodulated by third-order harmonics, too.

4.4.1 Static response of the interferometer

Static responses of the symmetric port are given by substituting Eq. (4.109) for x_n of Eq. (4.47) as follows,

$$x_n = r_{\mathrm{RSE},n} = r_{\mathrm{com_r},n} + \frac{t_{\mathrm{com_r},n} r_{\mathrm{t}} t_{\mathrm{com_t},n}}{1 - r_{\mathrm{com_t},n} r_{\mathrm{s}}} \tag{4.111}$$

where index n means carrier with $n = 0$ and nth order sidebands with $n \neq 0$.

Next, static responses of the anti-symmetric port are given by substituting Eq. (4.110) for x_n,

$$x_n = t_{\mathrm{RSE},n} = \frac{t_{\mathrm{com_r},n} t_{\mathrm{s}}}{1 - r_{\mathrm{com_t},n} r_{\mathrm{s}}}. \tag{4.112}$$

Eq. (4.60) and (4.61) are used for the demodulation with these x_n. All demodulated signals both at the symmetric port and the anti-symmetric port become 0 at the operating point of the interferometer.

4.4.2 Derivative response of the interferometer

We next consider derivatives of the static response to compare the magnitude of error signals of each degree of freedom. Since Eq. (4.82)$\sim$(4.85) are functions of

Φ_+,Φ_-,ϕ_-,$\phi_{\rm s}$, Eq. (4.109) and (4.110) are function of Φ_+,Φ_-,ϕ_-,$\phi_{\rm s}$. Therefore x_n is also a function of Φ_+,Φ_-,ϕ_-,$\phi_{\rm s}$. The demodulated signal differentiated with θ is described as

$$\delta V_n = \frac{\partial V_n}{\partial \theta}\delta\theta \tag{4.113}$$

and, the coefficient

$$\frac{\partial V_n}{\partial \theta} \tag{4.114}$$

shows the magnitude of the error signal. Here, V_n is substituted by Eq. (4.64) $\sim$ (4.71), and θ indicates Φ_+,Φ_-,ϕ_-,$\phi_{\rm s}$.

The calculation will be a little complex, so only the results are written here. $g_{\rm det}$ and $E_{\rm in}$ are assumed to be unity and broad-band RSE is assumed for simplicity:

$$\phi_{\rm t,0} = 2n\pi. \tag{4.115}$$

We define a variable

$$g_n \equiv \frac{1}{1 + r'_{\rm anti} r_{\rm S} \cos n\alpha}. \tag{4.116}$$

This means a gain of the carrier ($n = 0$) and the $n\,(n \neq 0)$ order sidebands in the RSE cavity which is composed of the Fabry-Perot Michelson interferometer as a compound mirror and the SEM.

Because the first-order sidebands resonate in the SEC to enable the signal acquisition at the anti-symmetric port, the first-order sidebands satisfy

$$\gamma = 2n\pi \tag{4.117}$$

First, demodulated signal of Eq. (4.64) differentiated by each phase Φ_+,Φ_-,ϕ_-,$\phi_{\rm s}$ are

$$\begin{aligned}
\frac{\partial}{\partial \Phi_+} V^{\rm I}_{\rm SY,1a} &= 2 - J_0 J_1 g_1^2 \{ |r'_{\rm reso}| r_{\rm anti} (r_{\rm anti} r_{\rm S} + \cos\alpha)(1 + r_{\rm anti} r_{\rm S} \cos\alpha) \\
&\quad - |r'_{\rm anti}| r_{\rm reso} (2 r_{\rm anti} r_{\rm S} + \cos\alpha + r_{\rm anti}^2 r_{\rm S}^2 \cos\alpha) \} \qquad (4.118) \\
\frac{\partial}{\partial \Phi_-} V^{\rm I}_{\rm SY,1a} &= 0 \qquad (4.119) \\
\frac{\partial}{\partial \phi_-} V^{\rm I}_{\rm SY,1a} &= 0 \qquad (4.120) \\
\frac{\partial}{\partial \phi_s} V^{\rm I}_{\rm SY,1a} &= 2 J_0 J_1 g_1^2 r_{\rm anti} r_{\rm reso}^3 r_{\rm S}^2 \cos\alpha \sin\alpha \qquad (4.121)
\end{aligned}$$

which are the '-1, 0, 1' order signal of the symmetric port demodulated in-phase. The signals demodulated in-phase have no differential mode components, that is, Φ_-,ϕ_- will not come out, only the common modes are extracted.

Next, the higher-order '2, -1, 1, 2' of the symmetric port demodulated in-phase, that is to say, the derivative of Eq. (4.66) by each phase are given as

$$\begin{aligned}
\frac{\partial}{\partial\Phi_+}V^{\rm I}_{SY,1b} &= -2J_1J_2g_1^2g_2^2|r'_{\rm anti}|r^2_{\rm anti}r_{\rm S}(1+2\cos\alpha)\{2-2r_{\rm anti}r_{\rm S}+2r^2_{\rm anti}r^2_{\rm S} \\
&\quad -2(1-r_{\rm anti}r_{\rm S})^2\cos\alpha+(1+r^2_{\rm anti}r^2_{\rm S})\cos 2\alpha\}\sin^2\alpha \qquad (4.122)\\
\frac{\partial}{\partial\Phi_-}V^{\rm I}_{\rm SY,1b} &= 0 \qquad (4.123)\\
\frac{\partial}{\partial\phi_-}V^{\rm I}_{\rm SY,1b} &= 0 \qquad (4.124)\\
\frac{\partial}{\partial\phi_s}V^{\rm I}_{\rm SY,1b} &= -J_1J_2g_1^2g_2^2[r^4_{\rm anti}r^2_{\rm S}(1+\cos\alpha+\cos 2\alpha)\{3r_{\rm anti}r_{\rm S} \\
&\quad +2(1-3r_{\rm anti}r_{\rm S}+r^2_{\rm anti}r^2_{\rm S})\cos\alpha+2(1-4r_{\rm anti}r_{\rm S}+r^2_{\rm anti}r^2_{\rm S})\cos 2\alpha \\
&\quad +2(1-r_{\rm anti}r_{\rm S}+r^2_{\rm anti}r^2_{\rm S})\cos 3\alpha+r_{\rm anti}r_{\rm S}\cos 4\alpha\}\sin^2\alpha] \qquad (4.125)
\end{aligned}$$

which also have no contributions from the differential mode.

Next, the derivatives of the symmetric port with quadrature-phase are obtained by differentiating Eq. (4.65) and (4.67),

$$\begin{aligned}
\frac{\partial}{\partial\Phi_+}V^{\rm Q}_{\rm SY,1a} &= 0 \qquad (4.126)\\
\frac{\partial}{\partial\Phi_-}V^{\rm Q}_{\rm SY,1a} &= 2J_0J_1g_1^2|r'_{\rm anti}|r_{\rm reso}(1-r^2_{\rm anti}r^2_{\rm S})\sin\alpha \qquad (4.127)\\
\frac{\partial}{\partial\phi_-}V^{\rm Q}_{\rm SY,1a} &= 2J_0J_1g_1^2r_{\rm anti}r_{\rm reso}(1-r^2_{\rm anti}r^2_{\rm S})\sin\alpha \qquad (4.128)\\
\frac{\partial}{\partial\phi_s}V^{\rm Q}_{\rm SY,1a} &= 0 \qquad (4.129)
\end{aligned}$$

$$\begin{aligned}
\frac{\partial}{\partial\Phi_+}V^{\rm Q}_{\rm SY,1b} &= 0 \qquad (4.130)\\
\frac{\partial}{\partial\Phi_-}V^{\rm Q}_{\rm SY,1b} &= 2J_1J_2g_1g_2|r'_{\rm anti}|r_{\rm anti}(1-r^2_{\rm anti}r^2_{\rm S})\{g_1(r_{\rm anti}r_{\rm S}+\cos 2\alpha)\sin\alpha \\
&\quad +g_2(r_{\rm anti}r_{\rm S}+\cos\alpha)\sin 2\alpha\} \qquad (4.131)\\
\frac{\partial}{\partial\phi_-}V^{\rm Q}_{\rm SY,1b} &= J_1J_2g_1^2g_2^2r^2_{\rm anti}(1-r^2_{\rm anti}r^2_{\rm S})\{2(1-r_{\rm anti}r_{\rm S})^2 \\
&\quad +(4-r_{\rm anti}r_{\rm S}+4r^2_{\rm anti}r^2_{\rm S})\cos\alpha
\end{aligned}$$

$$+r_{\rm anti}r_{\rm S}\cos 3\alpha\}(\sin\alpha+\sin 2\alpha) \tag{4.132}$$

$$\frac{\partial}{\partial\phi_s}V^{\rm Q}_{\rm SY,1b} = 0 \tag{4.133}$$

which have no common mode signal.

Next, we look at the anti-symmetric port. The derivatives of the anti-symmetric port signal by each phase are

$$\frac{\partial}{\partial\Phi_+}V^{\rm I}_{\rm AS,1a} = 0 \tag{4.134}$$

$$\frac{\partial}{\partial\Phi_-}V^{\rm I}_{\rm AS,1a} = 0 \tag{4.135}$$

$$\frac{\partial}{\partial\phi_-}V^{\rm I}_{\rm AS,1a} = 0 \tag{4.136}$$

$$\frac{\partial}{\partial\phi_s}V^{\rm I}_{\rm AS,1a} = 0 \tag{4.137}$$

$$\frac{\partial}{\partial\Phi_+}V^{\rm I}_{\rm AS,1b} = 2J_1J_2g_1^2g_2^2|r'_{\rm anti}|r^2_{\rm anti}r_{\rm S}t_{\rm s}^2(\cos\alpha+\cos 2\alpha)\sin\alpha\sin 2\alpha \tag{4.138}$$

$$\frac{\partial}{\partial\Phi_-}V^{\rm I}_{\rm AS,1b} = 0 \tag{4.139}$$

$$\frac{\partial}{\partial\phi_-}V^{\rm I}_{\rm AS,1b} = 0 \tag{4.140}$$

$$\frac{\partial}{\partial\phi_s}V^{\rm I}_{\rm AS,1b} = 32J_1J_2g_1^2g_2^2r^3_{\rm anti}r_{\rm S}t_{\rm s}^2\cos\left(\frac{\alpha}{2}\right)^2(1+\cos\alpha+\cos 2\alpha)\sin\left(\frac{\alpha}{2}\right)^4 \tag{4.141}$$

$$\frac{\partial}{\partial\Phi_+}V^{\rm Q}_{\rm AS,1a} = 0 \tag{4.142}$$

$$\frac{\partial}{\partial\Phi_-}V^{\rm Q}_{\rm AS,1a} = -2J_0J_1g_0g_1|r'_{\rm reso}|r_{\rm anti}t_{\rm s}^2\sin\alpha \tag{4.143}$$

$$\frac{\partial}{\partial\phi_-}V^{\rm Q}_{\rm AS,1a} = -2J_0J_1g_0g_1r_{\rm reso}r_{\rm anti}t_{\rm s}^2\sin\alpha \tag{4.144}$$

$$\frac{\partial}{\partial\phi_s}V^{\rm Q}_{\rm AS,1a} = 0 \tag{4.145}$$

$$\frac{\partial}{\partial\Phi_+}V^{\rm Q}_{\rm AS,1b} = 0 \tag{4.146}$$

$$\frac{\partial}{\partial\Phi_-}V^{\mathrm{Q}}_{\mathrm{AS,1b}} = -2J_1J_2g_1g_2|r'_{\mathrm{anti}}|r_{\mathrm{anti}}t_{\mathrm{s}}^2\{g_1(r_{\mathrm{anti}}r_{\mathrm{S}}+\cos\alpha)\sin 2\alpha + g_2(r_{\mathrm{anti}}r_{\mathrm{S}}+\cos 2\alpha)\sin\alpha\} \quad (4.147)$$

$$\frac{\partial}{\partial\phi_-}V^{\mathrm{Q}}_{\mathrm{AS,1b}} = J_1J_2g_1^2g_2^2r_{\mathrm{anti}}^2t_{\mathrm{s}}^2\{(1+r_{\mathrm{anti}}r_{\mathrm{S}}\cos\alpha)(r_{\mathrm{anti}}r_{\mathrm{S}}+\cos 2\alpha)\sin\alpha + (r_{\mathrm{anti}}r_{\mathrm{S}}+\cos\alpha)(1+r_{\mathrm{anti}}r_{\mathrm{S}}\cos 2\alpha)\sin 2\alpha\} \quad (4.148)$$

$$\frac{\partial}{\partial\phi_s}V^{\mathrm{Q}}_{\mathrm{AS,1b}} = 0. \quad (4.149)$$

We should notice that the common mode signals are not obtained from '-1, 0, 1' even with in-phase demodulation. They come from the '2, -1, 1, 2' order.

Finally, we think about the third harmonic demodulation at the anti-symmetric port,

$$\frac{\partial}{\partial\Phi_+}V^{\mathrm{I}}_{\mathrm{AS,3a}} = 0 \quad (4.150)$$

$$\frac{\partial}{\partial\Phi_-}V^{\mathrm{I}}_{\mathrm{AS,3a}} = 0 \quad (4.151)$$

$$\frac{\partial}{\partial\phi_-}V^{\mathrm{I}}_{\mathrm{AS,3a}} = 0 \quad (4.152)$$

$$\frac{\partial}{\partial\phi_s}V^{\mathrm{I}}_{\mathrm{AS,3a}} = 0 \quad (4.153)$$

$$\frac{\partial}{\partial\Phi_+}V^{\mathrm{I}}_{\mathrm{AS,3b}} = 2J_1J_2g_1^2g_2^2|r'_{\mathrm{anti}}|r_{\mathrm{anti}}^2r_{\mathrm{S}}t_{\mathrm{s}}^2(\cos\alpha+\cos 2\alpha)\sin\alpha\sin 2\alpha \quad (4.154)$$

$$\frac{\partial}{\partial\Phi_-}V^{\mathrm{I}}_{\mathrm{AS,3b}} = 0 \quad (4.155)$$

$$\frac{\partial}{\partial\phi_-}V^{\mathrm{I}}_{\mathrm{AS,3b}} = 0 \quad (4.156)$$

$$\frac{\partial}{\partial\phi_s}V^{\mathrm{I}}_{\mathrm{AS,3b}} = 32J_1J_2g_1^2g_2^2r_{\mathrm{anti}}^3r_{\mathrm{S}}t_{\mathrm{s}}^2\cos\left(\frac{\alpha}{2}\right)^2(1+\cos\alpha+\cos 2\alpha)\sin\left(\frac{\alpha}{2}\right)^4 \quad (4.157)$$

$$\frac{\partial}{\partial\Phi_+}V^{\mathrm{Q}}_{\mathrm{AS,3a}} = 0 \quad (4.158)$$

$$\frac{\partial}{\partial\Phi_-}V^{\mathrm{Q}}_{\mathrm{AS,3a}} = -2J_0J_3g_0g_3|r'_{\mathrm{reso}}|r_{\mathrm{anti}}t_{\mathrm{s}}^2\sin 3\alpha \quad (4.159)$$

$$\frac{\partial}{\partial\phi_-}V^{\mathrm{Q}}_{\mathrm{AS,3a}} = -2J_0J_3g_0g_3r_{\mathrm{reso}}r_{\mathrm{anti}}t_{\mathrm{s}}^2\sin 3\alpha \quad (4.160)$$

$$\frac{\partial}{\partial \phi_s} V^{\mathrm{Q}}_{\mathrm{AS,3a}} = 0 \tag{4.161}$$

$$\frac{\partial}{\partial \Phi_+} V^{\mathrm{Q}}_{\mathrm{AS,3b}} = 0 \tag{4.162}$$

$$\frac{\partial}{\partial \Phi_-} V^{\mathrm{Q}}_{\mathrm{AS,3b}} = -2J_1J_2g_1g_2|r'_{\mathrm{anti}}|r_{\mathrm{anti}}t_{\mathrm{s}}^2\{g_1(r_{\mathrm{anti}}r_{\mathrm{S}}+\cos\alpha)\sin 2\alpha + g_2(r_{\mathrm{anti}}r_{\mathrm{S}}+\cos 2\alpha)\sin\alpha\} \tag{4.163}$$

$$\frac{\partial}{\partial \phi_-} V^{\mathrm{Q}}_{\mathrm{AS,3b}} = J_1J_2g_1^2g_2^2r_{\mathrm{anti}}^2t_{\mathrm{s}}^2[2-r_{\mathrm{anti}}r_{\mathrm{S}}+r_{\mathrm{anti}}r_{\mathrm{S}}\{3\cos\alpha+2\cos 2\alpha - (1-r_{\mathrm{anti}}r_{\mathrm{S}})\cos 3\alpha+\cos 4\alpha\}]\sin\alpha \tag{4.164}$$

$$\frac{\partial}{\partial \phi_s} V^{\mathrm{Q}}_{\mathrm{AS,3b}} = 0 \tag{4.165}$$

here, it must be noted that (4.141) and (4.157) have the same form. In other words, the signals of the higher-order (2, -1, 1, 2) for the change of ϕ_{s} have the same magnitude, regardless of whether first-order or third-order demodulation is used.

4.5 Signal-separation method using THD

The preparation to discuss the response of the RSE interferometer has been completed in the last section. In this section we examine the effect of third harmonic demodulation (THD) applied to the RSE interferometer.

4.5.1 Effect of THD

THD is a method of using the third harmonic of modulation frequency f_{m} as a local oscillator for the demodulation. In the conventional scheme the error signal of the SEC consists of the beat between the -2nd order sideband with the -1st order sideband plus the beat of the +1st order sideband with the +2nd order sideband (see the left of Fig. 4.5.1). In the case of THD, the error signal of the SEC consists of the beat between the -2nd order sideband with the +1st order sideband plus the beat of the -1st order sideband with the +2nd order sideband (see the right of Fig. 4.5.1). The magnitude of signal is the same as the signal obtained using first order demodulation.

On the other hand, the phase change of the carrier, which has information of the arm cavities, will be detected by the beat of the carrier with the third-order

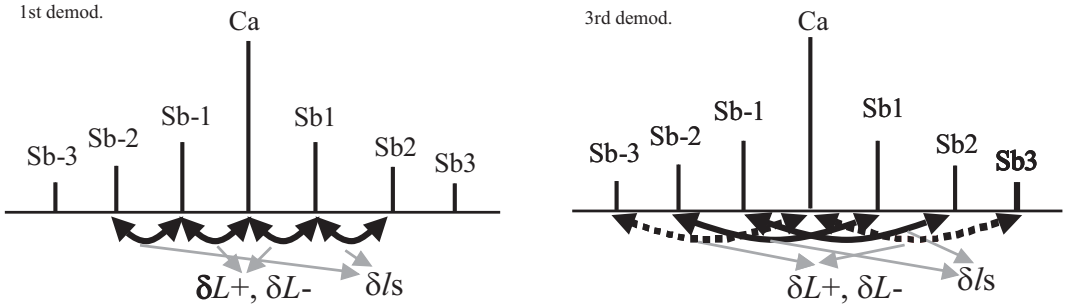

Figure 4.8: Demodulated signal. Left figure shows the case of conventional first order demodulation, and right figure shows the case of third harmonic demodulation.

sidebands. Compared with the conventional first-order demodulation, where the carrier beating with the first order sidebands detect the phase change of the carrier, the influence of the arm cavities is reduced by

$$\frac{J_3 g_3 \sin 3\alpha}{J_1 g_1 \sin \alpha} \tag{4.166}$$

from Eq. (4.159), (4.143). Since $J_3 \ll J_1$, the cross-coupling ratio of the arm cavity signal to the SEC signal will be improved.

4.5.2 Adjusting the asymmetry for THD

We can further improve the cross-coupling by making the amplitude of the third-order sideband zero, because the phase change of the carrier is not detected if there are no the third-order sidebands. We can satisfy this condition by adjusting the asymmetry length l_- of the interferometer for a given modulation frequency. Such l_- is given as follows

$$\frac{3\omega_m l_-}{c} = \pi, \tag{4.167}$$

where ω_m is a modulation frequency, and c is a light velocity. The reason of π (not 2π) is that the phase of the third-order sideband is reversed by the asymmetry , so the total phase change of third-order sideband is 2π. If THD is used under such a condition, the signal ratio can be drastically improved.

4.5.3 Resonant condition

In the section we determine the proper resonant conditions of the carrier and the sidebands in the signal extraction cavity to extract the proper control signal.

Carrier

Parameter $l_{\rm s}$ should be controlled in accuracy below the laser wave length so that the carrier may be resonant in the signal extraction cavity of RSE when each arm cavity is not resonant. However if each arm cavity is resonant, the phase reverses at the reflection on each arm cavity, with the net effect that the carrier becomes anti-resonant condition in the SEC. So the carrier experiences the phase change in the SEC as follows

$$\phi_{\rm s,0} = \pi + 0 = \pi \qquad (\mathrm{mod}\, 2\pi). \tag{4.168}$$

The first term represents the phase change experienced in the SEC without considering the reflection at the front mirror of each arm cavity (see Eq. (4.16)). The second term is the phase change experienced at the reflection from each arm cavity, because a complex reflectivity of the Fabry-Perot cavity is positive if the Fabry-Perot cavity is resonant (see Eq. (4.78)).

first-order sideband

The macroscopic length of the SEC $l_{\rm s}$ is determined by the wave length of first-order sideband in order to extract the proper control signal under the resonant condition of the carrier given as Eq. (4.168) in the SEC. The first-order sideband experiences the phase change in the SEC as

$$\phi_{\rm s,1} = \pi + 2\pi + \pi + 0 = 0 \qquad (\mathrm{mod}\, 2\pi). \tag{4.169}$$

The first term represents the phase of the carrier. The second term is the phase change determined by the macroscopic length of the SEC. The third term is the phase change experienced at the reflection on the arm cavity, and the forth term is the phase change obtained by the asymmetry.

second-order sideband

If the first-order sideband is completely anti-resonant for the arm cavity, the second-order sideband is resonant in the arm cavity. However, when nothing is controlled, the state with the first-order sideband completely anti-resonant is thought to be uncommon. It can be thought that the first-order sideband is not resonant in conventional case, therefore, the situation that the second-order sideband is not resonant in the arm is plausible. Then the resonant condition of the second-order sideband is written as

$$\phi_{\mathrm{s},2} = \pi + 4\pi + \pi + \pi = \pi \qquad (\mathrm{mod}\, 2\pi). \tag{4.170}$$

The second-order sideband is anti resonant in the signal extraction cavity in total. The explanation of phase change of each term is the same in the case of the first-order sideband. The last term is caused by an asymmetry length. It is assumed that the special asymmetry with which the third-order sideband vanishes at the anti-symmetric port is present.

third-order sideband

If the first-order sideband is completely anti-resonant for the arm cavity, the third-order sideband is completely anti-resonant for the arm cavity. Even if it is not completely anti-resonant, it is hard to consider the situation that the third-order sideband enters into the arms as same reason as the second-order sideband. Anyway, as a result, the phase change which the third-order sideband experiences in the signal extraction cavity is written as

$$\phi_{\mathrm{s},3} = \pi + 6\pi + \pi + \pi = \pi \qquad (\mathrm{mod}\, 2\pi). \tag{4.171}$$

It is expected that the third-order sideband is anti-resonant or is near to be anti-resonant for the signal extraction cavity

It should be noted that the resonant condition of the first- and second-order sideband can be changed by changing the asymmetry length. This THD method assumes the asymmetry length which extinguishes the third-order sideband at the anti-symmetric port. This interesting condition indicates that the no power-recycling RSE interferometer can be expanded to a power-recycled RSE interferometer with THD.

The actual value at the 4th term of Eq. (4.169)∼(4.171) was not 0,π and π but rather $\pi/3$,$2\pi/3$ and π. For clarify of explanation these terms were rounded to 0,π and π so that the cavity could be considered simple as resonant or anti-resonant rather than somewhere in between. Since the finesse of the cavity is low, in practice, this detuning is not critical.

4.6 DC signal sensitivity

In this section, we substitute a concrete numerical value, and discuss whether the acquisition of the control signal is possible.

4.6.1 Optical parameters

Table 4.1: Optical parameters of a model interferometer used in the calculation for comparing the cross-coupling.

Parameter	Symbol	Value
Modulation index	m	0.6
Reflectivity of beam splitter	r_{BS}^2	50 %
Reflectivity of front mirror	r_{F}^2	99.5 %
Reflectivity of end mirror	r_{E}^2	99.99 %
Reflectivity of signal extraction mirror	r_{s}^2	60 %

Parameters used for the calculation is shown in Table 4.1. The phase in the SEC and the asymmetry are determined by the the resonant condition discussed in Sec. 4.5.3. It should be noted that the calculation results do not depend on the incident power and the demodulation g_{det} gain because the results are represented as ratios.

4.6.2 Matrix of discriminants

Conventional first-order demodulation

We calculated an example of a signal extraction method for RSE using a single pre-modulation. Tables 4.2 and 4.3 show the derivatives of the error signals to the length

Table 4.2: Signal ratio of each mirror motion from the carrier and the first-order sidebands.

	δL_+	δL_-	δl_-	δl_s
SY(I)	1	0	0	0.0010
AS(Q)	0	1	0.00075	0
SY(Q)	0	0.00075	1	0
AS(I)	0	0	0	0

Table 4.3: Signal ratio of each mirror motion from the first and the second-order sidebands.

	δL_+	δL_-	δl_-	δl_s
SY(I)	1	0	0	0.00095
AS(Q)	0	1	0.00082	0
SY(Q)	0	0.00075	1	0
AS(I)	0.00075	0	0	1

Table 4.4: Signal ratio of each mirror motion from the first and the second-order sidebands with the THD.

	δL_+	δL_-	δl_-	δl_s
AS3(I)	0.00074	0	0	1

changes around the resonant point. For the lengths, "δL_+" and "δL_-" stand for the common- and differential-mode lengths of the arm cavities. "δl_-" is the differential-mode length of the Michelson interferometer and "$\delta l_{\rm s}$" the length of the SEC (see Fig. 4.1). For the ports, "AS" the dark port, and "SY" the reflected port of the interferometer. For the demodulation phase, "I" means the in-phase demodulation and "Q" the quadrature-phase demodulation (see Fig. 4.2).

The coefficients in Table 4.2 are calculated from the beat signals between the carrier and the first-order sidebands. It should be noted that there is no signal of δl_s from AS(I) in Table 4.2. The beat of the carrier and the first sideband will be zero when only the first sideband are considered because the carrier does not leak out to the anti-symmetric port when the interferometer is moved in common mode.

The situation changes if we take into account the second-order sidebands which appear for sufficiently high modulation index. Table 4.3 shows the error signals obtained from the beat between the first- and second-order sidebands. The signals obtained are identical to these for the beat between the carrier and first-order sidebands, except for the in-phase signal at the anti-symmetric port. If we consider up to the third-order sideband, signal of the signal extraction cavity can be extracted by the beat of the first- and second-order sideband.

The photodetectors detect a linear combination of the two signals (from Tables 4.2 and 4.3). By proper choice of the modulation index, independent signals for all degrees of freedom can be obtained.

Third harmonic demodulation

Next, we show the result of calculation of signals demodulated at the frequency of the third-order sideband (THD) in Table 4.4. The result is the same as the result for first-order demodulation with the third-order harmonics shown in Table 4.3. This is because the signal is from the sum of beat of -2,-1 and beat of 1,2 in the first demodulation, on the other hand the signal is from the sum of beat of -1,2 and beat of -2,1 in the third harmonic demodulation. Therefore we can acquire the signal without changing the magnitude.

Table 4.5: Signal ratio of each mirror motion. The upper line is the signal extracted by the fundamental demodulation with the quadrature-phase, and the lower line is the signal extracted by the THD with the quadrature-phase.

	δL_+	δL_-	δl_-	δl_s
AS(Q)	0	27000	22	0
AS3(Q)	0	0.0000034	0.0045	0

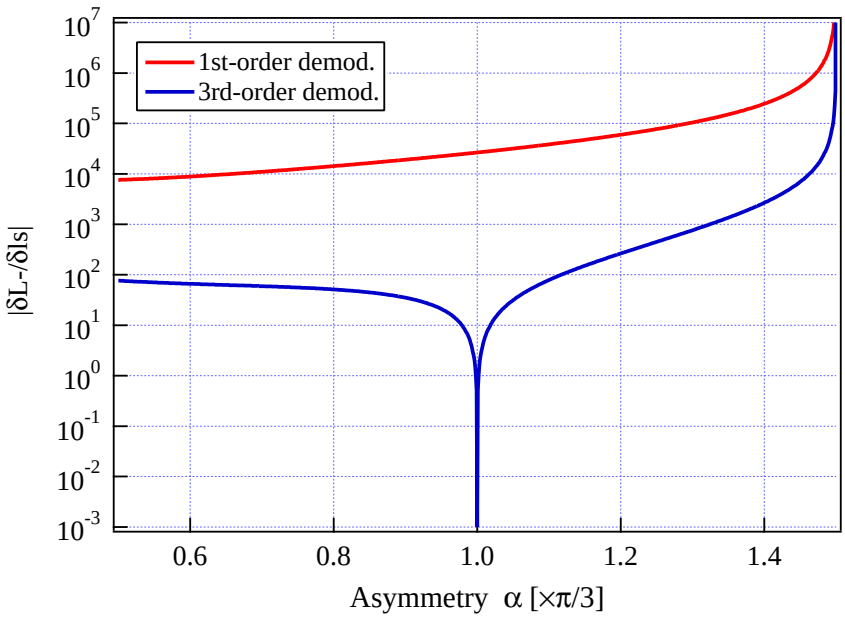

Figure 4.9: The signal ratio of δL_- to δl_s for fundamental demodulation and for THD. The curve obtained by the THD has a good signal ratio at the point which the third-order sideband vanish at the anti-symmetric port.

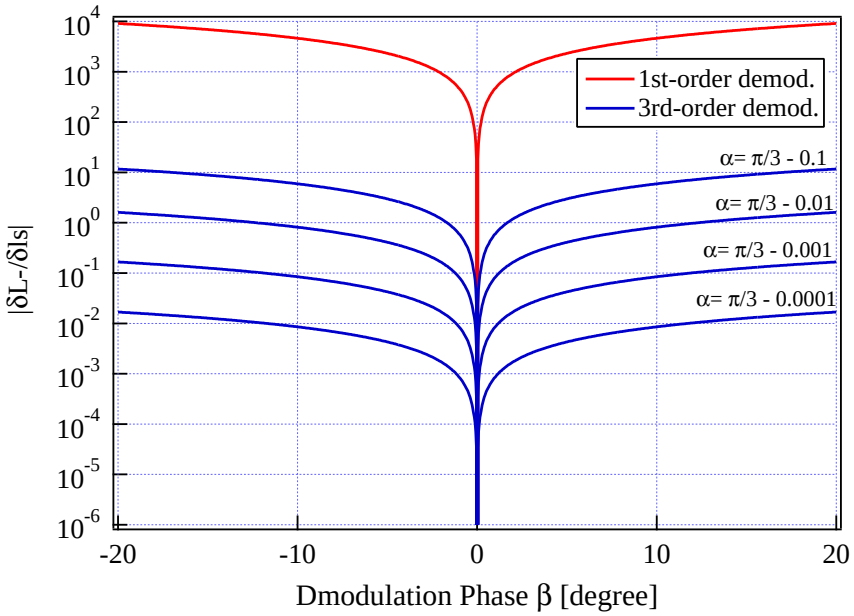

Figure 4.10: The signal ratio of δL_- to δl_s for fundamental demodulation and for THD with various asymmetries as a function of the demodulation phase of the SEC signal.

4.6.3 Demodulation phase

From the result above, it seems that first-order demodulation can extract the control signal well enough, so we don't need the third harmonic demodulation. However, this assumes the ideal condition that the demodulation phase is perfectly 'In-phase'. That is to say the fear of δL_- signal mixing greatly with the δl_s signal exists when the phase of the local oscillator deviated. How much the signal mixes depends on the size of the signal of δL_- obtained in the 'Q-phase' demodulation. There is a big difference in the size of this δL_- between the first-order demodulation and the third harmonic demodulation.

Table 4.5 shows signals from the anti-symmetric port demodulated by the first-order or the third harmonic demodulation. Because of the Q-phase demodulation, only δL_- and δl_- signal appear. Because it is difficult to adjust the demodulation phase properly, Q-phase and In-phase mix actually according to Eq. (4.62). The top line shows the signal from the first-order demodulation and the bottom line shows the signal from the third harmonic demodulation. The size of δL_- is remarkably small, so it is understood that cross-coupling is drastically improved with the third

harmonic demodulation.

If the asymmetry about 2.9 m is adopted for the modulation frequency of 17.25 MHz used by this experiment, we can achieve the condition which makes the third sideband vanish in the anti-symmetric port. Naturally because the third-order sideband leaks out to the anti-symmetric port when the asymmetry is shifted, a cross-coupling term appears. Fig. 4.9 shows the cross-coupling between δL_- and δl_s as a function of the asymmetry by the first-order demodulation and the third harmonic demodulation. In the case of the third harmonic demodulation, there is a point at $\alpha = 1$, where $\alpha = (2l_-\omega_{\rm m})/c$ that the cross-coupling is drastically improved, see Eq. (4.23).

In this condition, the cross-coupling is determined by three parameters; the asymmetry, the demodulation phase, and the contrast. When contrast is also considered, we will concretely see how much the accuracy of the demodulation phase and the asymmetry is needed. We consider the graph with the cross-coupling as the vertical axis and the demodulation phase as the horizontal axis for variable asymmetry. Fig. 4.10 shows the result. If the accuracy of the demodulation phase is within ± 10 degree, the cross-coupling does not exceed 1 with an asymmetry accurately set to 1 put in 100.

4.7 Frequency response

Deriving the frequency dependent signal requires the knowledge of how signals are generated, and a model for how they are detected.

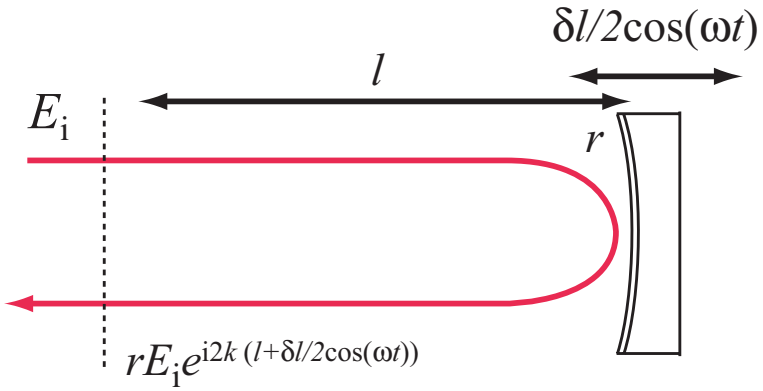

Figure 4.11: The effect of a field incident on a moving mirror.

The effect of the gravitational wave on the end mirrors can be interpreted as a

tidal force causing the mirrors to move relative to the beamsplitter. The motion of the mirrors phase modulates the fields incident on the mirror, as seen in Fig. 4.11. It is assumed for this analysis that the mirror motion is sinusoidal at frequency $\omega = 2\pi f$. If the incident field at the dashed line is given by $E_{\rm i}$, then the field returning from the mirror is

$$\begin{aligned} E_{\rm r} &= r E_{\rm i} e^{i2k(l+\delta l/2\cos(\omega t))} \\ &\approx r E_{\rm i} e^{i2kl(1+ik\delta l\cos(\omega t))} \\ &\approx r E_{\rm i} e^{i2kl(1+ik\delta l/2e^{\omega t}+ik\delta l/2e^{-\omega t}} \end{aligned} \tag{4.172}$$

The approximation is a Taylor series assuming a very small modulation of the mirror position $\delta l \ll k$. In this limit, the phase modulation of the light adds small signal sidebands on either side of the incident frequency, with amplitudes $irk\delta l/2$ relative to the input field. These are occasionally frequency band from referred to as "audio sidebands", since the frequencies of interest tend to be in the 10 to 1000 Hz.

Detection is a more complicated function now that the light incident on the photodiode includes the audio sidebands. For full generality, it is assumed that the modulation of the mirror is applied to the carrier and both RF sidebands, which produces two audio sidebands on each incident field at frequency $\pm\omega_{\rm g}$. There are nine field components incident on the photodiode.

$$\begin{aligned} E_{\rm PD} &= E_{0+}e^{i\omega_{\rm g}t} + E_{00} + E_{0-}e^{-i\omega_{\rm g}t} + \\ &\quad E_{++}e^{i(\Omega+\omega_{\rm g})t} + E_{+0}e^{i\Omega_{\rm g}t} + E_{0-}e^{i(\Omega-\omega_{\rm g})t} + \\ &\quad E_{-+}e^{i(-\Omega+\omega_{\rm g})t} + E_{-0}e^{-i\Omega_{\rm g}t} + E_{--}e^{i(-\Omega-\omega_{\rm g})t}. \end{aligned} \tag{4.173}$$

The overall carrier $e^{i\omega t}$ phase has been dropped, and the subscripts are ordered to indicate first, the RF sidebands or the carrier (+ indicating the +/− RF sideband, 0 indicating the carrier, etc.), and second, which order audio sideband. E_{+-} is then the lower audio sideband of the upper RF sideband.

The power measured by the photodiode will have, as in the DC case, power at DC, Ω and 2Ω, as well as components close to these frequencies. Demodulation and subsequent low-pass filtering only picks out the components in the bandwidth defined by the low pass filter around Ω, so these are the only components of interest.

The low-pass frequency is assumed to be much greater than the frequencies of signals considered. It is also assumed that products between the signal sidebands are negligible.

$$\begin{aligned} |E_{\mathrm{PD}}|^2_{@\Omega} &= 2\mathrm{Re}\{E_{++}E_{00}^* e^{i(\Omega+\omega_{\mathrm{g}})t} + E_{-+}E_{00}^* e^{i(-\Omega+\omega_{\mathrm{g}})t} + \\ &\quad E_{+-}^* E_{00} e^{i(-\Omega+\omega_{\mathrm{g}})t} + E_{--}^* E_{00} e^{i(\Omega+\omega_{\mathrm{g}})t} + \\ &\quad E_{+0}E_{0-}^* e^{i(\Omega+\omega_{\mathrm{g}})t} + E_{-0}E_{0-}^* e^{i(-\Omega+\omega_{\mathrm{g}})t} + \\ &\quad E_{+0}^* E_{0+} e^{i(-\Omega+\omega_{\mathrm{g}})t} + E_{-0}E_{0-}^* e^{i(-\Omega+\omega_{\mathrm{g}})t}\}. \end{aligned} \tag{4.174}$$

The demodulated signal $V_{out}(t)$ is

$$\begin{aligned} V_{out}(t) &= \mathrm{Re}\{[E_{00}^*(E_{++}e^{i\beta} + E_{-+}e^{-i\beta}) + E_{00}(E_{--}^* e^{i\beta} + E_{+-}^* e^{-i\beta}) + \\ &\quad E_{0+}(E_{-0}^* e^{i\beta} + E_{+0}^* e^{-i\beta}) + E_{0-}^*(E_{+0}e^{i\beta} + E_{-0}e^{-i\beta})]e^{i\omega_{\mathrm{g}}t}\} \end{aligned} \tag{4.175}$$

where β is the demodulation phase. If it is assumed that the mirror motion is $\delta l(t) = \mathrm{Re}\{(1/k)e^{i\omega_{\mathrm{g}}t}\}$, the factor of k scales out of the amplitude of the audio sidebands (Eq. (4.172)). Equivalently, this also can be thought of as the direct phase modulation of the light incident on the mirror with amplitude of 1 rad. The signal sideband amplitudes are proportional to the individual transmission functions from the mirror to the photodiode, evaluated at frequency ω_{g}, as well as the amplitude of the light incident on the mirror.

4.8 Conclusion of this chapter

The model of sideband generation by a gravitational wave signal completes our model of the interferometer. In the next chapter we describe the prototype RSE interferometer and compare the predictions of this model to the result from the prototype.

Chapter 5

Prototype interferometer for RSE

We have discussed the signal extraction method of RSE using the THD in the last chapter. In this chapter, an experiment performed to investigate the RSE effect using the THD is described. We have constructed a prototype interferometer using suspended optics in a vacuum system. We performed a lock of the RSE and confirmed the band-variable effect by measurement the response of interferometer for the RSE and the FPMI configurations.

5.1 Experimental setup

To verify the THD experimentally, we constructed a prototype RSE interferometer as shown in Fig. 5.1. The laser light enters the interferometer through some mode matching lenses. An electro-optical modulator (EOM) is used for phase modulation with a modulation frequency of 17.25MHz. The main optical components of the interferometer are placed in the vacuum chamber. There are two vacuum chambers, which are connected to each other with a 3m beam tube to obtain an appropriate cavity length. The light which enters in the vacuum tank is divided into two beams by a beamsplitter (BS), and enters two Fabry-Perot (FP) arm cavities, respectively. A proper asymmetry of the Michelson interferometer is obtained by applying a big difference to the distance between the beamsplitter and the two front mirrors. Two mode matching lenses are used to provide proper mode matching for both arm cavities. The light reflected from the two Fabry-Perot cavities is recombined at the BS again. The interfering light which proceeds to the anti-symmetric port is partially reflected by the SEM, and resonates in the SEC. The main mirrors are suspended as pendulums, and the mirror position and alignment are controlled by four coil magnet

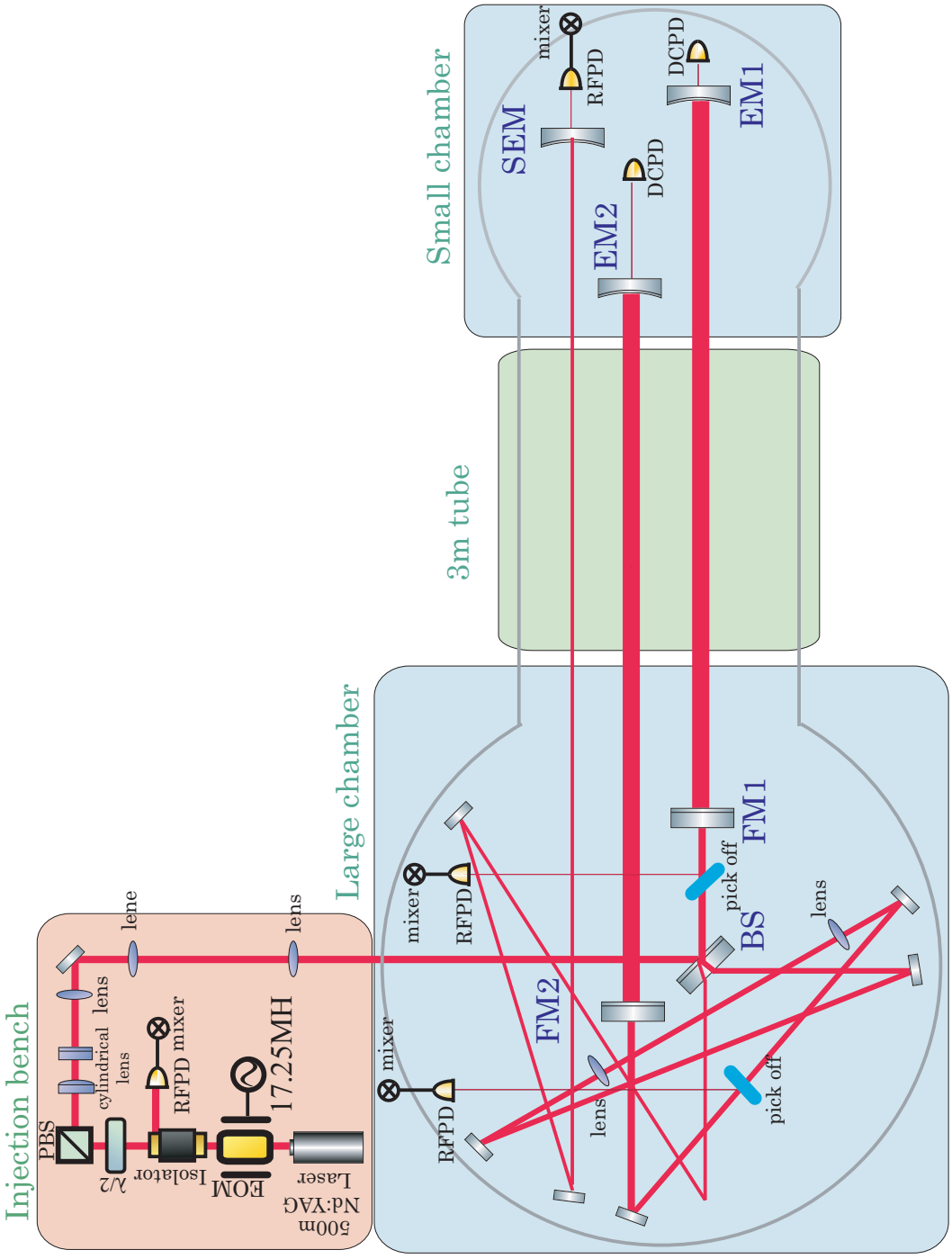

Figure 5.1: RSE interferometer optical configuration.

actuators. Motion of the mirror at the resonant frequency is efficiently damped by eddy-current damping.

5.1.1 Optical parameters of the experimental setup

Table 5.1: Optical parameters of the experimental setup.

Parameter	Symbol	Value
Power of laser source	P	500 mW
Wave length of laser	λ	1064 nm
Modulation frequency	$\omega_{\rm m}/2\pi$	17.25 MHz
Modulation index	m	0.6
Length of arm cavity	L	4 m
Length of asymmetry	l_-	2.89 m
Length of signal extraction cavity	$l_{\rm s}$	8.70 m
Reflectivity of beam splitter	$r^2_{\rm BS}$	50 %
Reflectivity of front mirror	$r^2_{\rm F}$	99.5 %
Reflectivity of end mirror	$r^2_{\rm E}$	99.99 %
Reflectivity of signal extraction mirror	$r^2_{\rm s}$	60 %
Radius of curvature of front mirror	$R_{\rm F}$	∞
Radius of curvature of end mirror	$R_{\rm E}$	6 m
Radius of curvature of signal extraction mirror	$R_{\rm s}$	10 m

Optical parameters of the interferometer shown in Table 5.1. These are the parameters of the experimental setup we have constructed. The length of the asymmetry and the SEC are determined by the resonant conditions discussed in Sec. 4.5.3.

5.1.2 Optics

Laser

The light source is a Lightwave model 126-1064-500, which is a 500 mW NPRO Nd:YAG 1064 nm laser. The frequency of laser is controlled in two ways: a slow

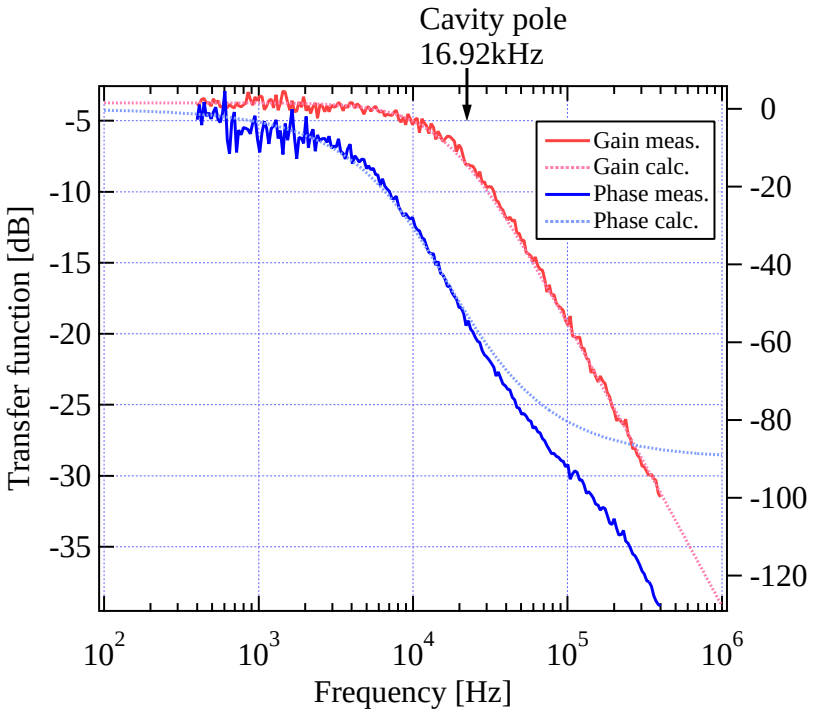

Figure 5.2: Measured transfer function of a single Fabry-Perot cavity. The cavity pole are obtained by fitting the measurement data.

control (<0.1 Hz) to a heater on the master oscillator laser crystal that tunes the laser frequency over a wide range and a fast control (0.1 Hz-12 kHz) to a PZT on the master oscillator laser crystal that tunes the laser frequency over a shorter range, but with a faster response. In this experiment, the fast control is used to stabilize the frequency of laser by using the error signal of the primary arm cavity.

Modulators

The phase modulator is a New Focus 4004M, which is a broad-band type from DC-100 MHz with roughly 15 mrad/V modulation depth. Instead of the resonance circuit which is often used for the EOM to increase the modulation depth with small applied voltages, a 33 dB power amplifier for the RF band is used to obtain enough modulation depth.

An AOM is used to measure the transfer function of the single Fabry-Perot cavity. Fig. 5.2 shows the measured transfer function of a single Fabry-Perot cavity. The frequency of cavity pole is determined to be 16.92 kHz which is obtained by the

fitting of the measurement.

Faraday isolator

The isolators are necessary to keep reflected light from one interferometer from coupling backwards to a previous interferometer. Specifically, any light going back into the laser resonator tends to cause the laser to either become noisy or go unstable altogether. Isolation is actually accomplished by three components, the Faraday rotator component to keep the polarization of the reflected light vertical and two polarizer components to separate the light of which polarization is missed. We use an OFR isolator, IO-3-YAG-HP, which contains the polarizers.

Mirrors

Front mirrors, end mirrors, and a beam splitter have been made by REO. A signal extraction mirror has been made by CVI. Reflectivity and radius of curvature of each mirror are shown in Table5.1. These core optics are suspended by the pendulums (see in Sec. 5.1.4). Other steering mirrors have been made by SIGMA KOKI. The steering mirrors are fixed on the bread-board by ULTIMA series mirror mount from NEW PORT. The size of all the mirrors is 1 inch in diameter and 5 mm in thickness.

Lenses

Two cylindrical lenses and three plain convex lenses are used for the mode matching. However the big asymmetry for the THD destroys of the modematching in one arm, so two other lenses are added between the beam splitter and the front mirror of the primary cavity to compensate the destroyed modematching.

Photodetectors

We have designed and developed for this experiment two kinds of photodetectors (PD).

The purpose of one type of PD is to see the phase modulated light which is separated several ten MHz from the carrier, this PD is sensitive in the RF band and is called "RFPD". The circuit of RFPD is shown in C.1. The RFPD has a broadband response over 400 kHz which is obtained by a high-pass filter. The RFPD also has another output with DC sensitivity below 400 kHz with a low-pass filter in order

to see the power of the light. There are four RFPD. One of them is placed at the pick-off port of each arm cavity, one is placed at the symmetric port, and last one is placed at the anti-symmetric port. The RF signal of the RFPD is used to generate the control signal by the demodulation scheme, and the DC signal of the RFPD is used to monitor the resonant condition of the interferometer.

The other type of photodetector is sensitive only near DC area. Its purpose is to see the power of the transmitted light through the arm cavities. This photodetector is called "DCPD". The circuit of DCPD is shown in C.2. The DCPD has a 3000× variable gain. There are two DCPD place after the arm cavity.

CCD cameras

Eight CCD cameras are used to monitor power build-up, the mode shape of the transmitted light of the arm cavity, and alignment in the vacuum chamber. We use the commercial CCD unit purchased at the AKITSUKI DENKI, which has a decent sensitivity at 1064 nm. The imaging lens on each camera for monitoring the mode shape was removed, and the light is was projected directly on the CCD element. We have three monitors which are connected to a selection system for the eight CCD signals.

5.1.3 Circuits

Frequency tripler

The THD needs a local oscillator whose frequency is three times the modulation frequency. The fundamental modulation frequency is 17.25 MHz, so the frequency of 51.75 MHz should be produced by a frequency tripler circuit (see Fig. C.3 in appendix C).

The frequency tripler works in the following way. First it makes a square wave from the original sinusoidal wave by a comparator. The square wave A includes components of frequencies which are $2n+1$ times the fundamental frequency f_{m} as

$$A = \frac{\pi}{4}[f_{\mathrm{m}} + \frac{1}{3}f_{3\mathrm{m}} + \frac{1}{5}f_{5\mathrm{m}}...] \tag{5.1}$$

Then the tripled frequency is extracted by a passive 3-pole band-pass filter. Finally the amplitude of the tripled frequency is amplified to the required level.

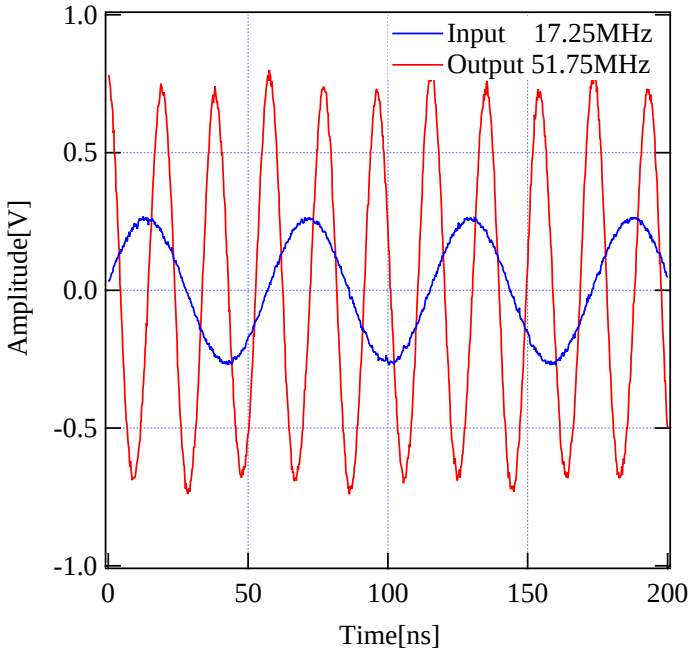

Figure 5.3: Input and output of the frequency tripler.

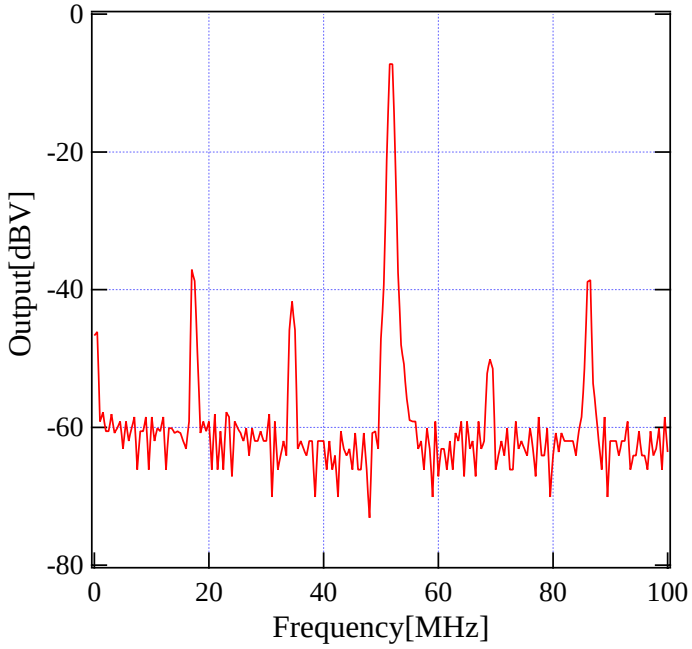

Figure 5.4: Ratio of the output amplitude in all band.

Fig. 5.3 shows the input and output wave forms of the frequency tripler. The output amplitude is $1.4\,V_{p-p}$, which is required for the demodulator. The output wave form seems to contain some fundamental mode. Fig. 5.4 shows the ratio of the output amplitude in all bands. The ratio between the amplitude of the tripled and the fundamental frequency is about 30dB. This value is not a concern for the experiment.

Feedback filter

The condition of the stability in the control system is that the delay of the phase does not exceed 180 degrees at the unity gain frequency (UGF) and the loop gain is high enough to keep the operating point well within the linear range. Because the interferometer used in this experiment is controlled via the pendulums, the phase is delayed by 180 degrees at frequencies above the resonant frequency of the pendulum (see Fig. 5.5). The feedback circuit should be designed in such a way that the phase delay of 180 degrees caused by the pendulum is recovered by the phase advance of the circuit.

The gain of the response function of this filter is $f^{1/2}$ between 5 Hz and 5 kHz. The circuit with such a frequency dependence has the effect of recovering the phase delay by 45 degrees within the frequency band mentioned above. Therefore, the UGF can be anywhere between 5 Hz and 5 kHz and the feedback system is still stable in terms of the phase delay condition. This filter is useful because the loop gain can change depending on the status of another degree of freedom in the interferometer.

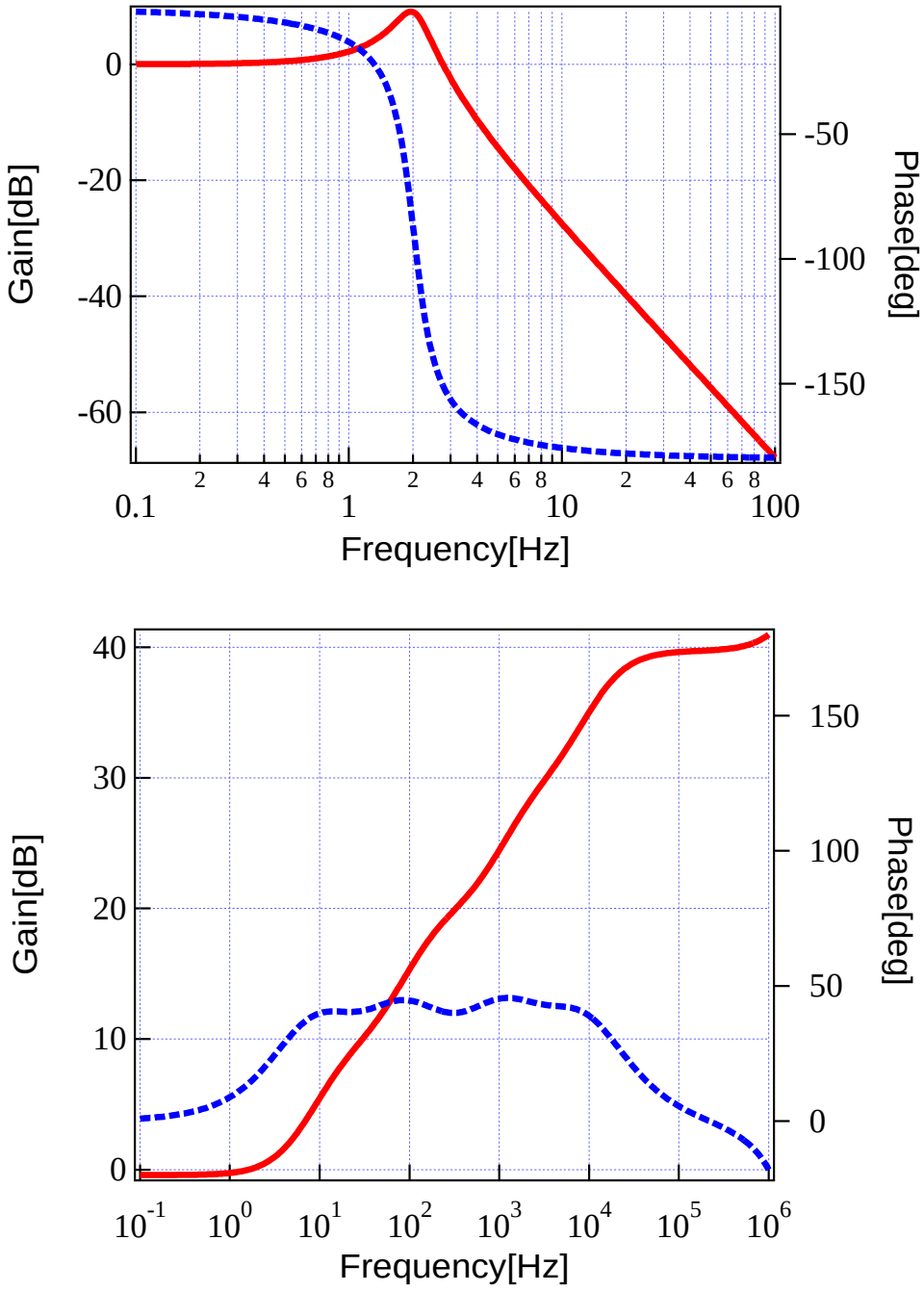

Figure 5.5: The upper graph is calculated transfer function of the pendulum, and lower one is calculated feedback filter. Solid lines are the gain, and dotted lines are the phase.

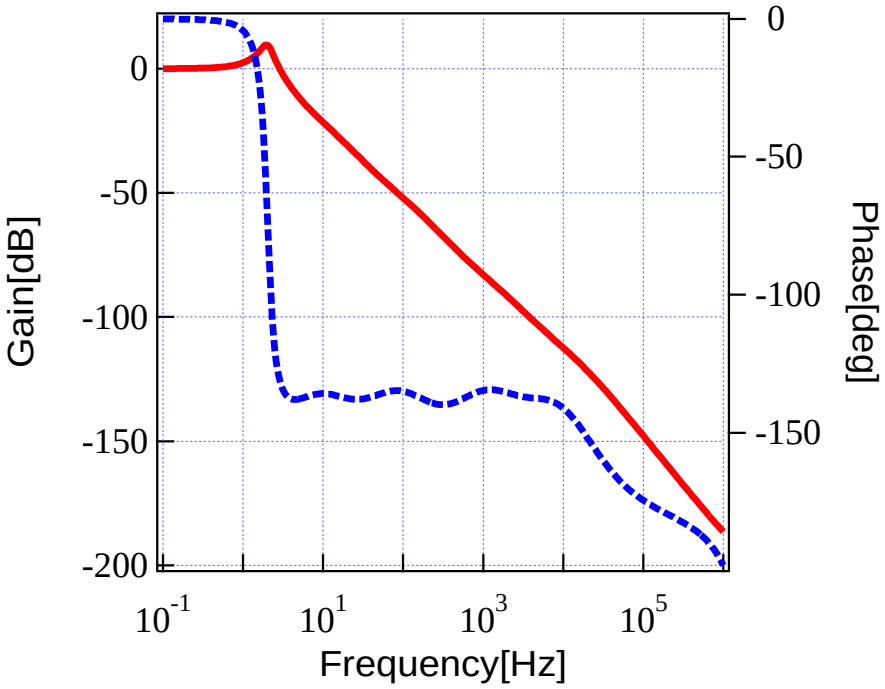

Figure 5.6: Transfer function of the product of the pendulum and feedback filter. Solid line is the gain, and dotted line is the phase.

5.1.4 Pendulum as a mirror mount

A mirror is suspended as a pendulum so that the mirror can be regarded as a free mass much above the resonant frequency of the pendulum. This makes the experimental setup of this research closer to the real interferometer setup. Here, we describe the pendulum which is used for this experiment.

A small suspension system was developed to satisfy the following requirements:

(1) Control capability of the mirror position with a wide bandwidth and a large range.

(2) Remote control capability of the mirror orientation.

(3) Simple damping mechanism of the pendulum and orientation resonances.

(4) Compactness for accommodation of several light paths in the beam tube.

From these requirements, the suspension system was designed as a small one-loop pendulum with magnet-coil actuation and eddy current damping system (See Fig. 5.7).

A mirror of 1 inch in diameter is attached to a piece of aluminum. The mirror position and orientation are controlled by four magnet-coil actuators. A driver circuit for the control of this coil is shown in Fig. C.6, C.7 in appendix C. All parts (mirror, pendulum, damping magnets, and coils) are fabricated as a module so that they can be moved up and down to adjust the beam heights. The suspension system is so small that at maximum, nine laser beams can be accommodated in the one 15 cm diameter beam tube.

Motion of the mirror at the resonant frequency is efficiently damped by the eddy-current damping between the aluminum piece and the external magnets. Because the interference between the magnets for actuation and the magnets for damping exist, attention must be paid for the position of the magnets. The detail will be described in appendix B.

5.1.5 Vacuum system

Fig. 5.8 shows the vacuum system. The two vacuum chambers are connected by a beam tube with a length of 3 m and a diameter of 15 cm. The beam tube can accommodate many light paths of the RSE interferometer with the help of a small

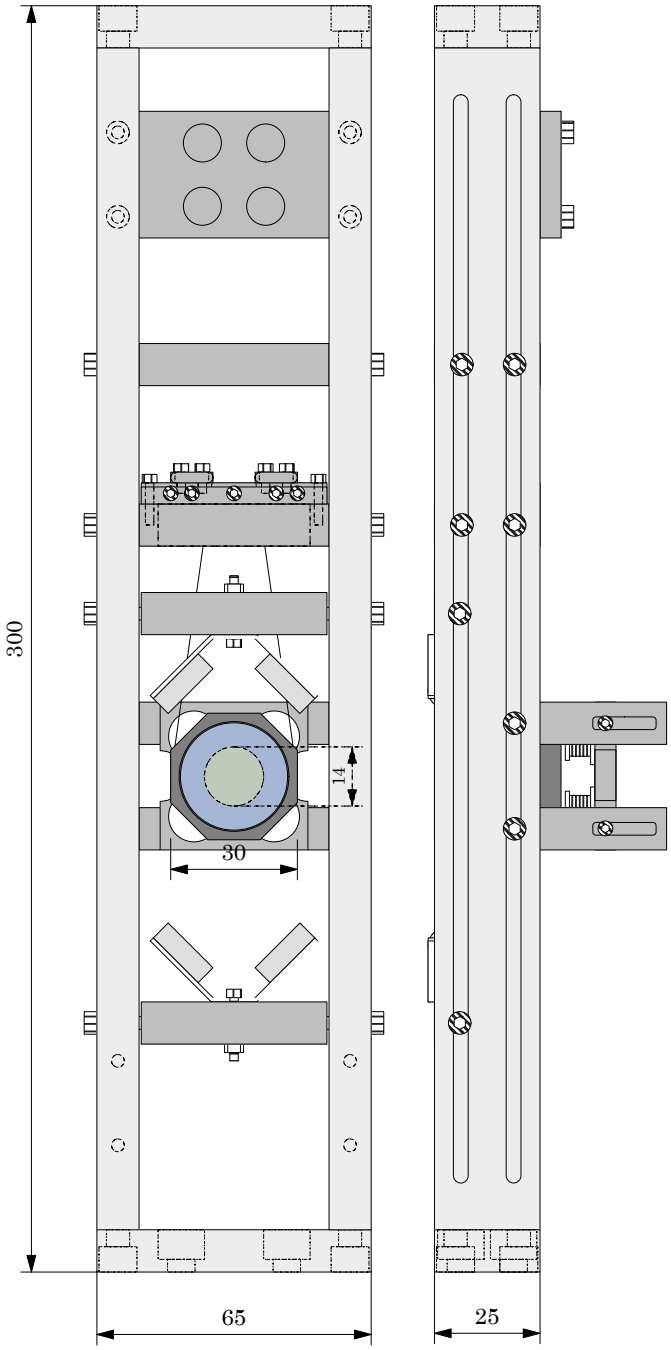

Figure 5.7: Small mirror suspension system: The mirror is suspended by one wire loop, and damped by eddy current damping. Length and alignment control is achieved by a 4 magnet coil actuation systems. They are moduled to be adaptable for varying beam heights.

mirror suspension system described below. A rotary pump and a turbo pump are used to evacuate the chamber.

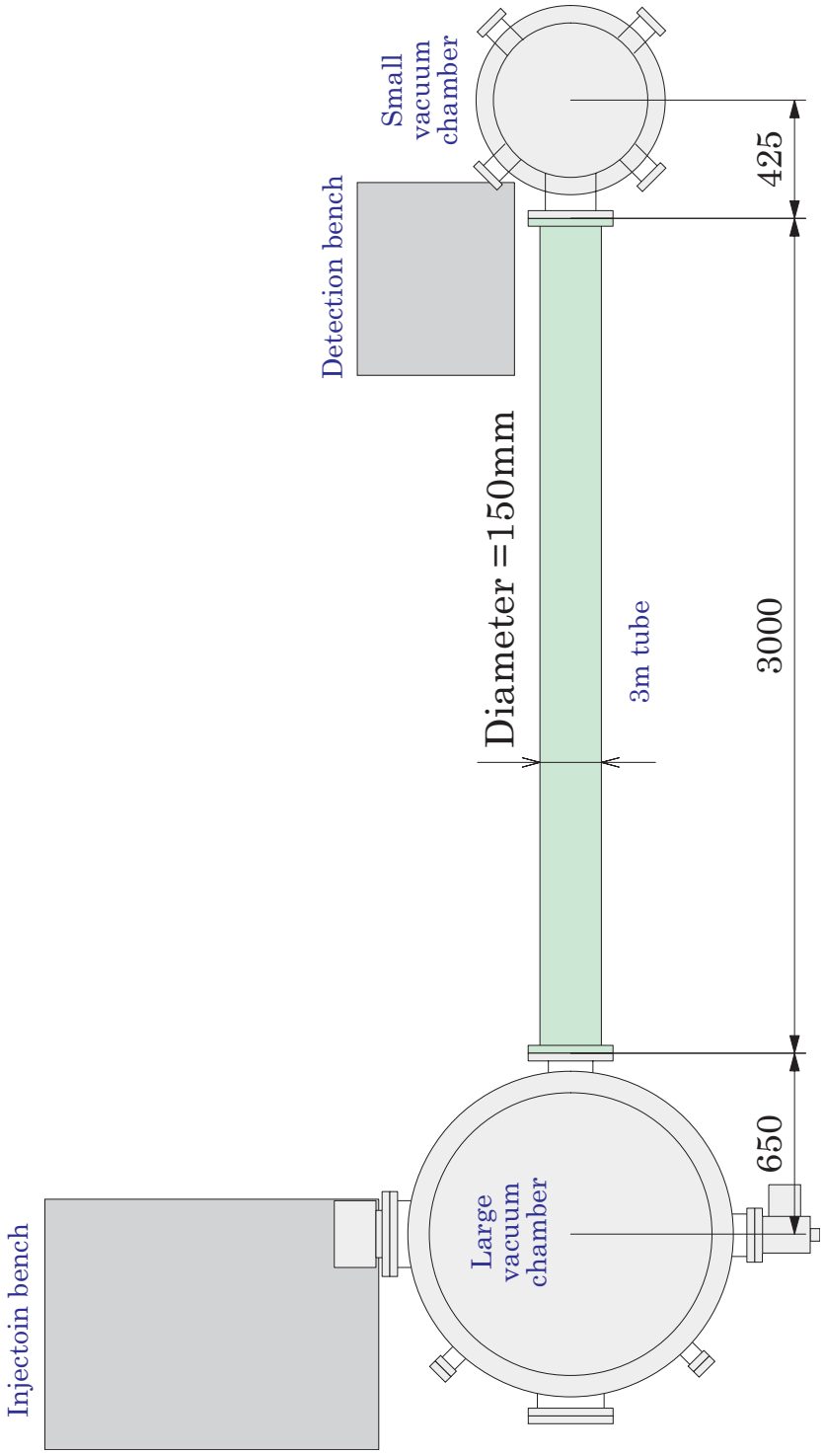

Figure 5.8: Experimental setup. There are two vacuum chambers connected by a 3 m length vacuum tube, 15 cm in diameter. We make four cavities in this vacuum tube.

5.2 Operation of RSE

Lock of a suspended-mass RSE interferometer has been performed for the first time in the world using this experimental setup with THD.

5.2.1 Control topology

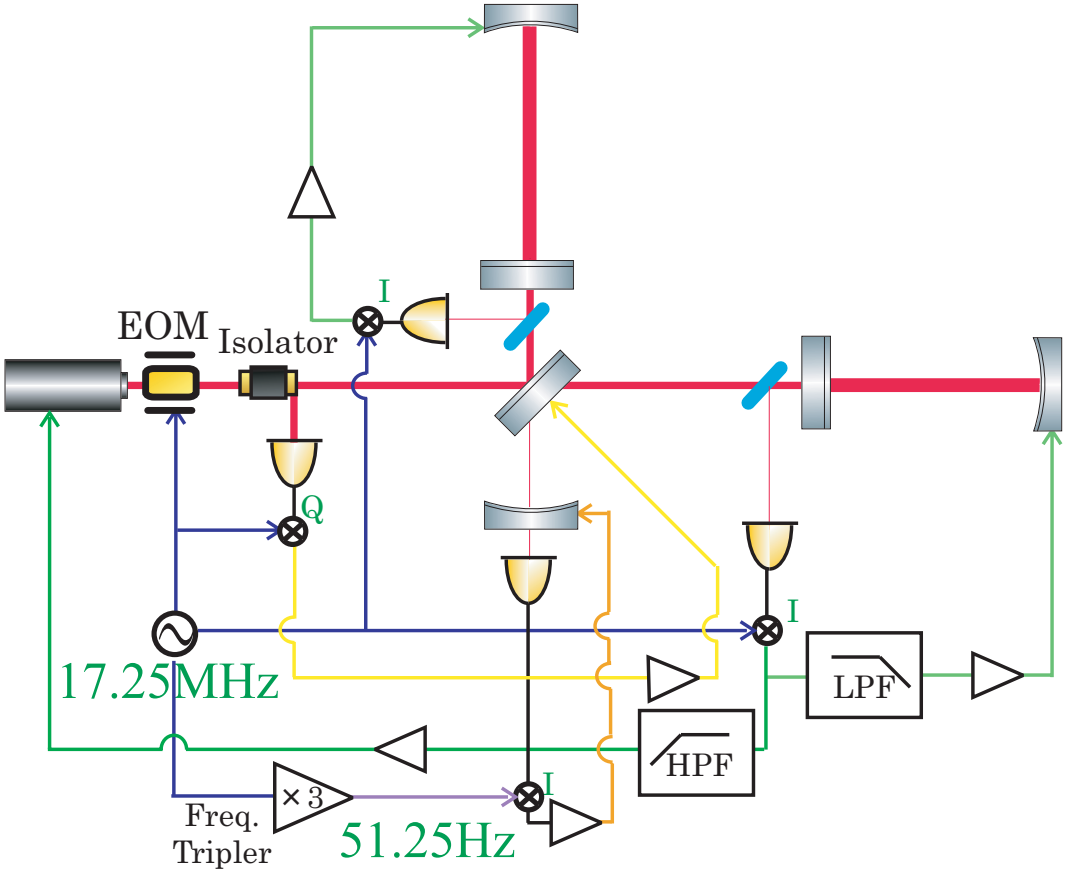

Figure 5.9: The RSE interferometer control topology.

Four degree of freedoms should be controlled in the RSE interferometer:

(1) Two Fabry-Perot cavities.

(2) The Michelson interferometer.

(3) The signal extraction cavity.

The control topology of the RSE interferometer using THD is shown in Fig. 5.9. Each Fabry-Perot arm cavity signals is independently extracted by picked-off light and is fed back to each end mirror. The error signal of the primary FP cavity is also used to stabilize the frequency of the laser source at high frequencies. The Michelson signal is extracted from the symmetric port with the quadrature-phase demodulation and fed back to the beamsplitter. The third harmonic demodulation is applied to the signal detected at the anti-symmetric port after the SEM and the obtained signal is fed back to the SEM.

5.2.2 Asymmetry

Asymmetry length should be chosen according to Eq. (4.167). When the modulation frequency is 15.25 MHz, the proper asymmetry length is 2.89 m. It is difficult to make such a big asymmetry length in this experimental setup, so the light pass of the primary cavity is folded 3 times (See Fig. 5.1). In order to compensate the modematching destroyed by the asymmetry, two lenses are placed between the beam splitter and the front mirror of the primary cavity.

5.2.3 Lock acquisition

We have succeeded in the locking the suspended-mass RSE at first, anywhere in the world. Fig. 5.10 shows a typical lock acquisition procedure. The upper two graphs show the transmitted power of the two FP arm cavities, and the third graph shows the light power at the anti-symmetric port. The bottom graph shows the error signal of the SEC using the THD.

(a) The primary FP cavity is locked, and the frequency stabilized loop is locked simultaneously.

(b) The secondary FP cavity is locked

(c) The Michelson part is locked.

(d) Finally, the Signal extraction cavity is locked and the entire RSE interferometer is operated.

Lock is stable, and locking time is typically over 10 minutes. After the lock of the SEC, the transmitted power of the primary cavity is increased, on the other

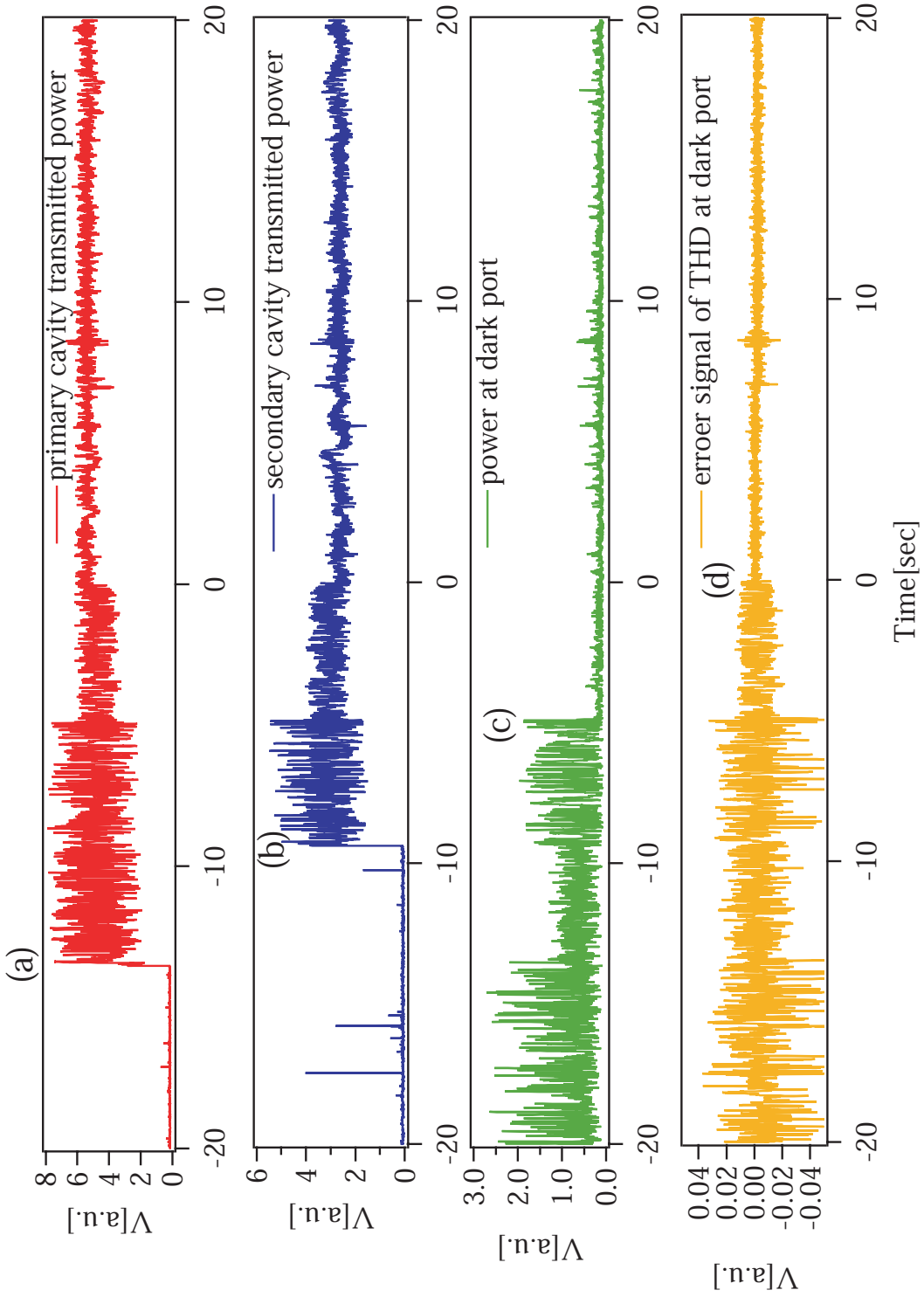

Figure 5.10: Lock acquisition of the RSE.

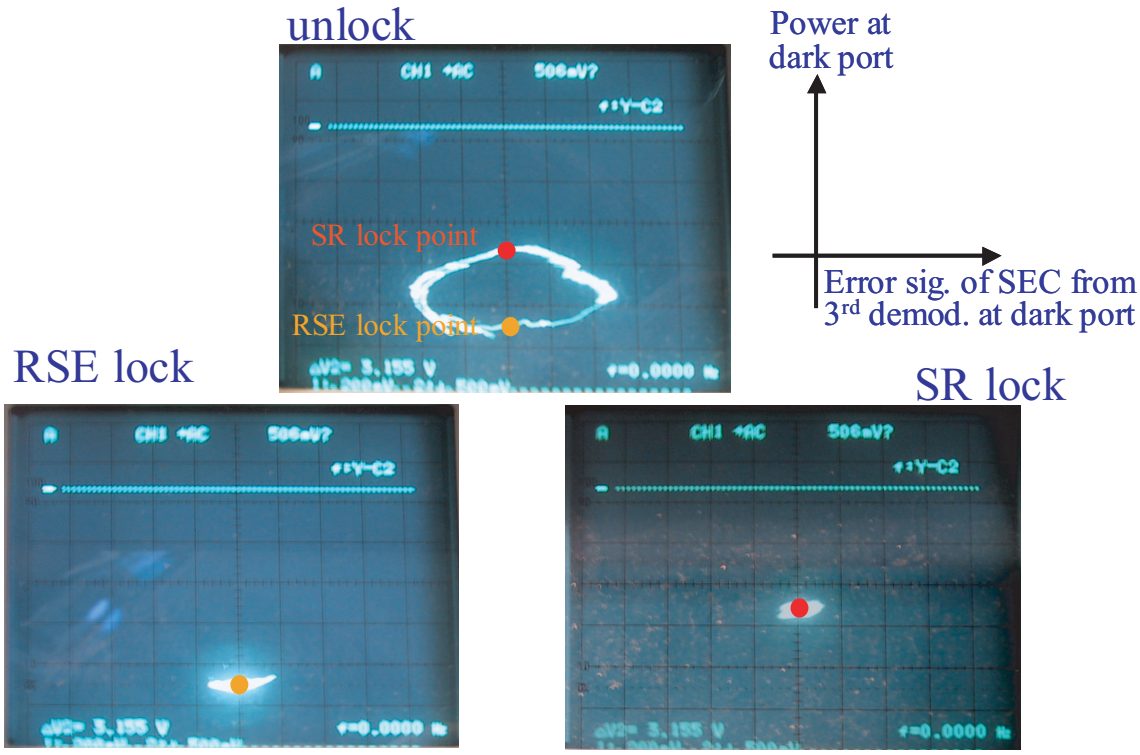

Figure 5.11: Monitor of the power at the anti-symmetric port as a function of the SEC signal when the RSE or the SR is locked.

hand the transmitted power of the secondary cavity is decreased. This is because the contrast is not perfect. The reflected light from the arm cavities interfere at the beamsplitter and if the contrast is not perfect, some carrier leaks out to the anti-symmetric port with the opposite phase. The SEM reflects this light in such a way that the SEC in one arm is resonant and the SEC in the other arm is anti-resonant. The interferometer can also be locked to another state which has the opposite power change in the arm cavities by reversing the polarity of the error signal of the SEC. We can tell that RSE is obtained when the power at the anti-symmetric port is decreased and SR is obtained when the power at the anti-symmetric port is increased (see Fig. 5.11). If the contrast is perfect, this phenomenon cannot be seen. So, we cannot tell whether it is locked to RSE or SR. We would have to investigate the locking status by measurement of the response function of the interferometer.

5.3 Measurement of the interferometer response

In order to confirm a variable-bandwidth effect by the RSE, we need to measure the frequency response of interferometer. A response function of the interferometer is obtained by a measurement of the differential mode of the arm cavities while the two end mirrors are excited with differential mode by coil-magnet actuators.

5.3.1 Setup

A setup for the measurement of the response function of the interferometer is shown in Fig. 5.12.

A network analyzer YOKOGAWA SA2600 which has an oscillator is used for this measurement. Measurement data were obtained by using a swept sine mode of the network analyzer. The swept sine mode performs all frequency measurement by sweeping the single frequency of the oscillator while measuring the same frequency using FFT.

Oscillation is added to two feedback loops of the arm cavity control in the differential mode. The signal right after the summing junction in one loop is subtracted from that in the other loop to obtain the signal V_1. The signal V_2 of the differential mode of the arm cavities L_- is obtained from the anti-symmetric port with the quadrature-phase demodulation.

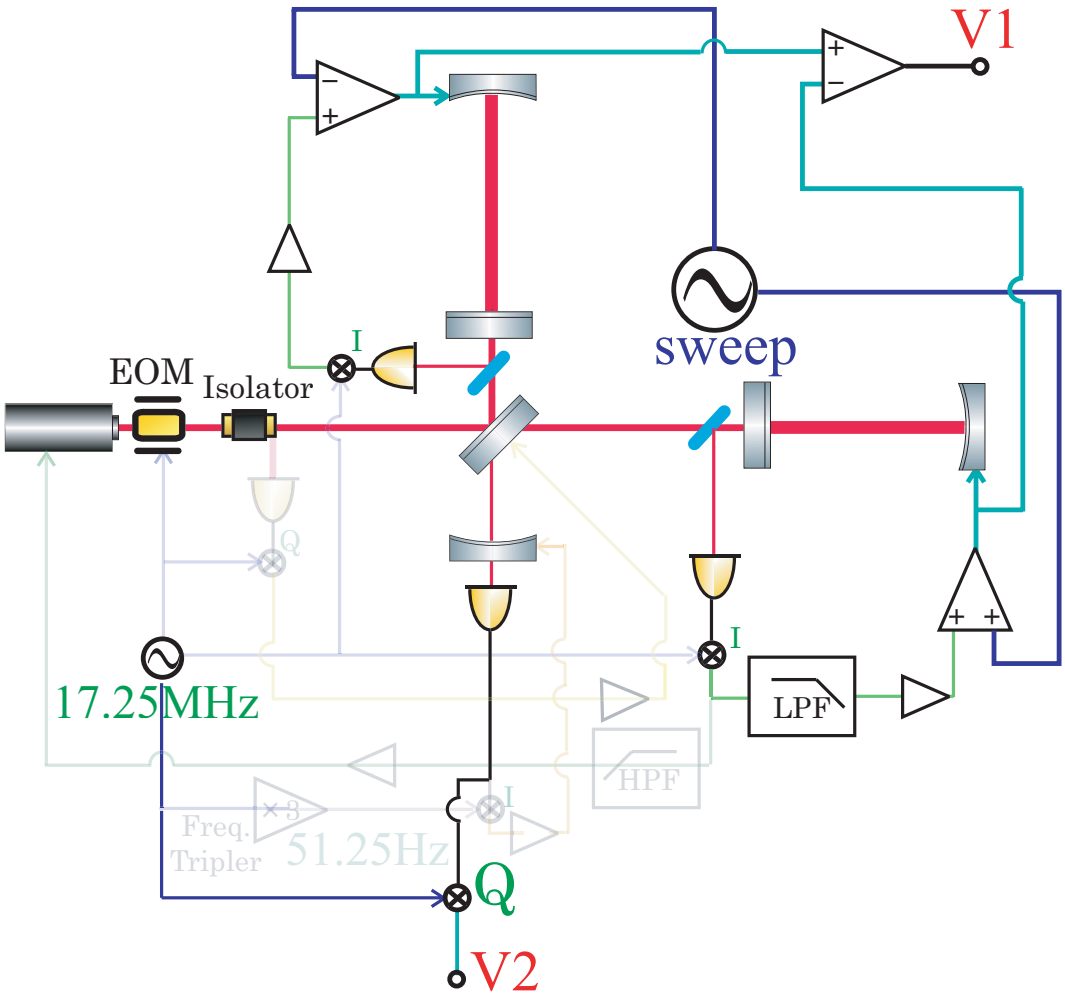

Figure 5.12: Setting for the measurement of the transfer function of the interferometer.

V_2 signal is considered as a residual motion of L_- when the interferometer is controlled. Therefore we have defined V_1 as the added signal after adding to the each feedback loop of the arm cavities because there is also residual signal. As a result of it, V_2/V_1 includes the actuator, pendulum, and optical gain of the L_- loop, so we are able to compare with each optical configuration without the effect of the control system.

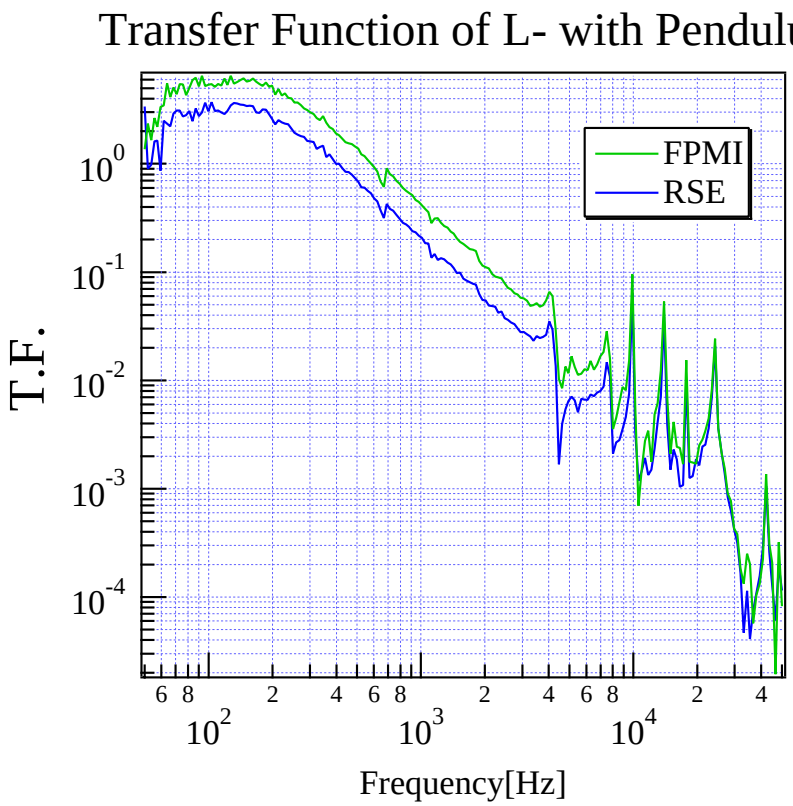

Figure 5.13: Measurement of the transfer function of the RSE and FPMI configuration.

5.3.2 Measurement

The measured transfer function of the RSE and FPMI configuration are shown in Fig. 5.15. When the response of the FPMI is measured, the SEM is miss-aligned. Raw measured data includes the slope and some resonances of the pendulum's transfer function. The FPMI response , in particular, includes the effect of the cavity pole around 16 kHz. On the other hand the RSE response has expanded bandwidth beyond the cavity pole of the FPMI but low gain around DC frequency.

The RSE effect can be seen easily in a relative transfer function which is obtained by dividing the transfer function of the RSE by the transfer function of the Fabry-Perot Michelson configuration. This cancels out the mirror actuation resonances, as well as the RF photodiode gains, mixer losses, etc. Fig. 5.14 shows the expected transfer function of he FPMI and the RSE interferometer. The calculation was performed by the simulation tool named 'FINESSE' which calculates the transfer

functions of the interferometer (See Appendix B). In fact the transfer function can not be seen directly such as Fig. 5.14, the measurement will only be the relative form as mentioned above.

The result of the relative transfer functions are shown in Fig. 5.15. Measurement is shown by solid line, and calculation by dotted line. The measurements agree with the calculations except for some resonances. The resonance may be caused by some kind of saturation. The band-width of the RSE interferometer is extended over 10 kHz compared with the FPMI configuration.

It should be measured at higher frequency over 100 kHz because the pole of the RSE interferometer will emerge around that band. However this measurement was performed by the actuating of the end mirrors suspended by the pendulum, so it could not be shaken above 50 kHz since the actuation decreases as f^{-2} for the pendulum. A good method for the measurement of transfer function of the interferometer is proposed by Australian group [38] using another laser to enter into the back of one arm cavity.

5.4 Conclusion of this chapter

We have succeeded to lock the suspended RSE interferometer using the THD method. To verify the effect of RSE locking, the relative transfer function between the FPMI and the RSE configuration have been measured. The gain of the RSE interferometer near DC is lower than the gain of the FPMI and the gain of higher frequency of the RSE interferometer is higher than the gain of the FP interferometer. It indicates that the RSE configuration varies the frequency response of the interferometer from the conventional FPMI configuration.

This result shows that the RSE configuration is available for the suspended optics. It is also a important milestone to develop a configuration of interferometers.

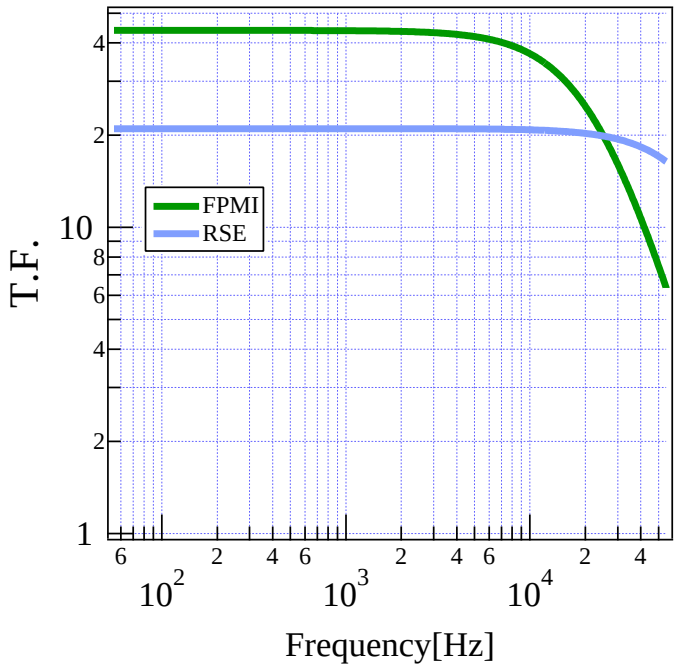

Figure 5.14: Calculation of the transfer function of the FPMI and the RSE interferometer.

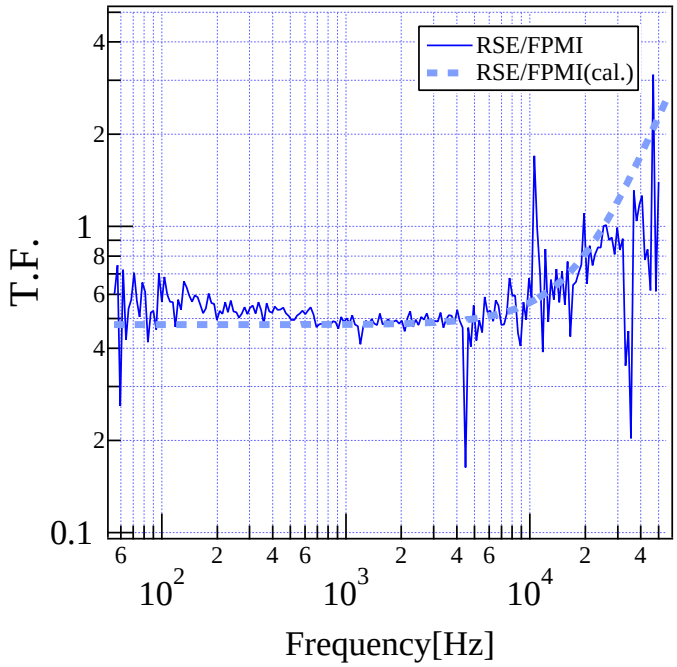

Figure 5.15: Measurement of the relative transfer function.

Chapter 6

Conclusions

6.1 Results

We aimed to control the interferometer with resonant sideband extraction using a single modulation. The interferometer was constructed to investigate the possibility to install RSE in a realistic gravitational wave detector by using a vacuum system and small suspended mirrors.

1. Comparison of various optical configurations in terms of normalized sensitivity

We compared various optical configurations of the interferometer such as ExDR, DR, PRFPMI, RSE, ExRSE. In the loss-less case, there is no difference of achievable normalized sensitivity among all the configurations. When the loss is concentrated in the substrates, however, we showed that the RSE with power recycling, whose gain distribution is optimized has the best normalized sensitivity.

Application of the third harmonic demodulation to the RSE

In the RSE prototype experiments which have been performed until now at institutions all around world, two or more modulations were used in order to extract the control signal of the SEC to reduce the cross-coupling from the arm cavity signals. The multi modulation scheme has two disadvantages: (a) the control system is complicated, and (b) all the sidebands produced by the modulations must be transmitted through the mode cleaner, thus the modulation frequencies can not be chosen freely. Our research aimed to demonstrate a control system for the SEC.

We developed a new method, that is, a control system using a single modulation with the third harmonic demodulation. The third harmonic demodulation was originally developed in the power recycling experiment of the 3m prototype interferometer. We applied this method to the control of RSE. Using this method we can extract the SEC signal with little cross-coupling. This cross-coupling can be further reduced by choosing the asymmetry of the Michelson interferometer in such a way that the third-order sidebands do not appear at the anti-symmetric port. This method is advantageous compared with the conventional multi modulation scheme: (a) the control system is simple, and (b) a single modulation can be transmitted through the mode cleaner easily. It should be emphasized that this method is valid for RSE even with the power recycling.

Experiment

In order to inspect the above idea experimentally, we constructed a prototype interferometer with suspended mirrors at the National Astronomical Observatory. The main optical components of the interferometer are built in the vacuum chamber in order to prevent from the mirrors being contaminated by the influence of the atmosphere. The main mirrors are suspended as small pendulums to reduce the influence of the ground motion. This pendulum has flexibility like a fixed mirror; for example each part of the suspension is fabricated as a module. In this way, we achieved the convenience of a table top experiment while using the vacuum and pendulums which are close to the realistic gravitational wave detector.

Using this experimental setup, we succeeded in control of the suspended-mirror RSE interferometer for the first time in the world. Moreover we locked both the RSE configuration and the SR configuration by reversing the phase of the SEC signal. The selection of these two configurations was verified by monitoring the power at the dark port. We confirmed the effect of the variable bandwidth of the interferometer by measuring the response functions of the RSE, the SR, and the FPMI, respectively.

6.2 Resonant sideband extraction for a large-scale interferometer

RSE is a required technology for realization of a future gravitational wave detector with super high sensitivity.

In this study, we succeeded in the operation of the RSE interferometer with an environment close to the realistic gravitational wave detector using the suspended mirrors in the vacuum chamber. We successfully developed a simple signal extraction method using the single modulation, and it is reasonable to say that the possibility of installing the RSE in a large-scale interferometer has increased.

The current vacuum system has a problem that the diameter of the tube is small, so the cavity length cannot be set freely. In future studies, this problem should be removed to try more flexible configurations and to optimize the optical parameters. The power recycling and the detuning should be tested in the prototype experiment to complete a deign of the optimum RSE for a large-scale interferometer. When the full RSE investigation including the power recycling and the detuning is completed, installing RSE in a large-scale interferometer will be ready.

Appendix A

Pendulum

Potential of the pitch and yaw directions by the pendulum is a restoring force, but the potential of the pitch and yaw directions by the force from the magnets is a bound force. The actual potential becomes the sum of these potentials. By relation of the position of magnets, the depth of the potential can be adjusted, and, as a result, the resonance frequency of each mode can be changed.

The resonance frequency of a pendulum f_{pend}, and the pitch f_{pitch}, and yaw f_{yaw} directions without the force by magnets is given as follows,

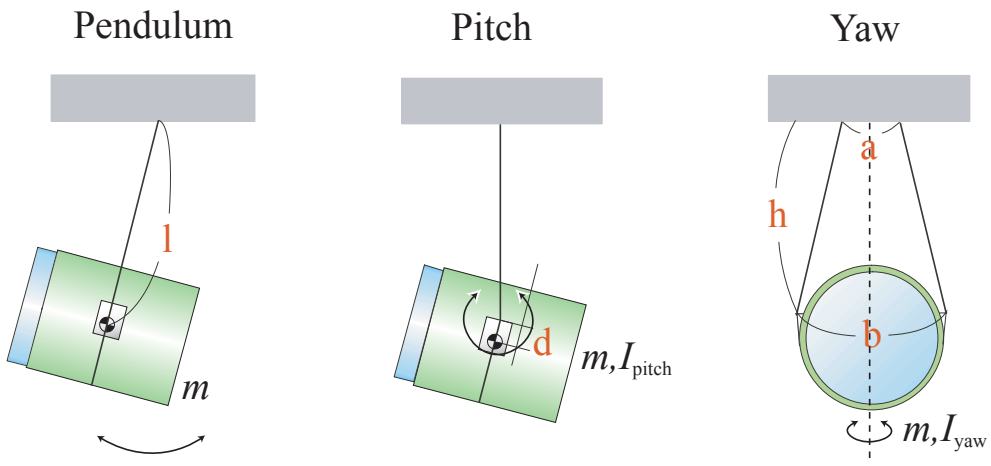

Figure A.1: Motions of pendulum, pitch, and yaw mode. 'm' denotes mass, and 'I' is inertial momentum. 'l', 'd' and 'a' can be changed independently, so the resonant frequency of each mode is adjustable.

$$f_{\mathrm{pend}} = \frac{1}{2\pi}\sqrt{\frac{l}{g}} \tag{A.1}$$

$$f_{\mathrm{pitch}} = \frac{1}{2\pi}\sqrt{\frac{mgd}{I_{\mathrm{pitc}}}} \tag{A.2}$$

$$f_{\mathrm{yaw}} = \frac{1}{2\pi}\sqrt{\frac{mgab}{4I_{\mathrm{yaw}}h}} \tag{A.3}$$

g is the gravitational acceleration, and other subscripts are shown in Fig. A.1. Because the resonance frequency of the pendulum mode can be adjusted by changing l, pitch by d, and yaw by a, this pendulum type has a variable resonance frequency type.

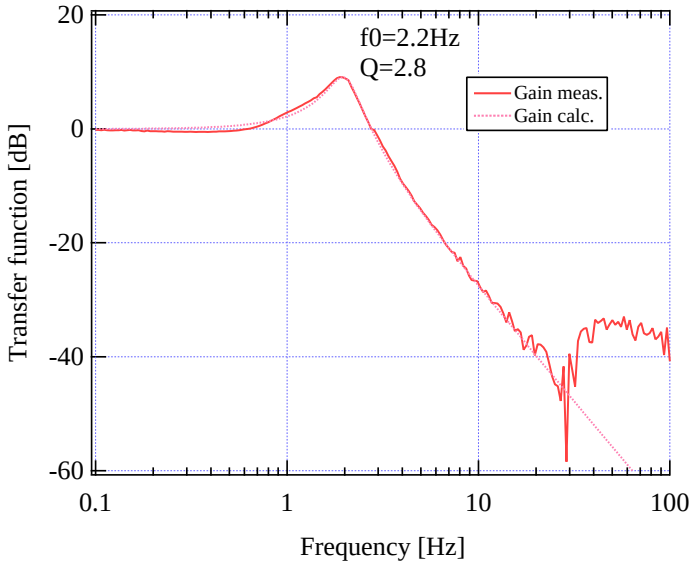

Figure A.2: Transfer function from the input voltage for the actuators to the displacement of the pendulum mode.

The effect of damping is in inversely proportion to the distance between the mass and the magnet for damping. Fig. A.3 shows the transfer function from the force to the displacement of the optical axis. The transfer function is normalized so that the DC area is 1. This graph was measured by a shadow sensor. From this figure, the resonant frequency is about 2.2 Hz and Q factor is about 2.8.

Moreover, force - displacement transfer functions of pitch and yaw are shown in Fig. A.3, and Fig. A.4.

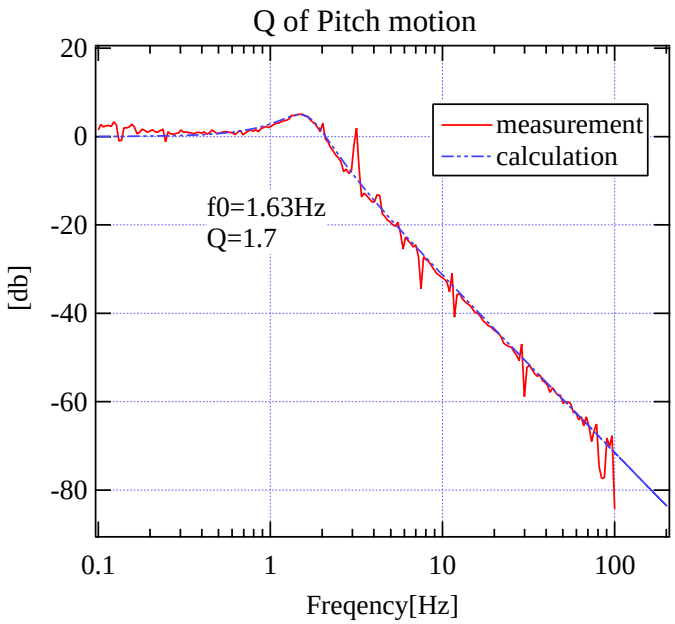

Figure A.3: Transfer function from the actuator to the pitch mode.

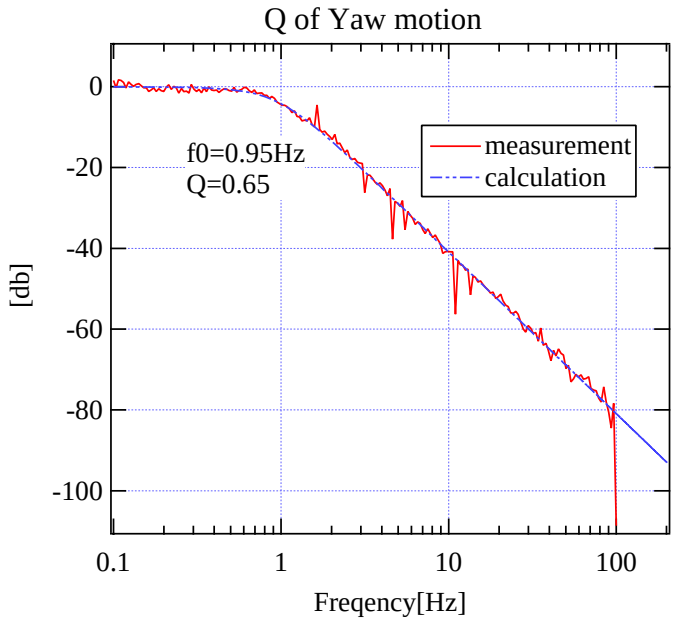

Figure A.4: Transfer function from the actuator to the yaw mode.

Appendix B

Simulation tools for calculation of the interferometer configurations

In the design of an interferometer length control system, it is necessary to know the transfer functions of the interferometer (which is sometimes called the "plant" in this context). Typically the inputs of this plant are the positions of the mirrors and the laser frequency. The plant outputs are often demodulated photocurrents, from photodiodes which measure the intensity at the optical outputs of the interferometer. A transfer function from one of the inputs to one of the outputs is then defined in the usual way: it is a function of frequency such that its amplitude and phase give the ratio of the signal at the output to the signal applied to the input.

B.1 Principle

Simulation tool works by building a set of linear equations which relate the fields incident on, and propagating away from, an arbitrary set of optics and light sources, through the propagation phases which connect the optics. The user has a set of commands with which to define the interferometer optics as well as the propagation paths. An example is shown in Fig. B.1 The fields at a mirror, for example, are related by

$$E_4 = r_1 E_3 + t_1 E_6 \tag{B.1}$$

$$E_5 = t_1 E_3 - r_1 E_6 \tag{B.2}$$

These fields are connected to the other mirrors and light sources by propagation phases, such as

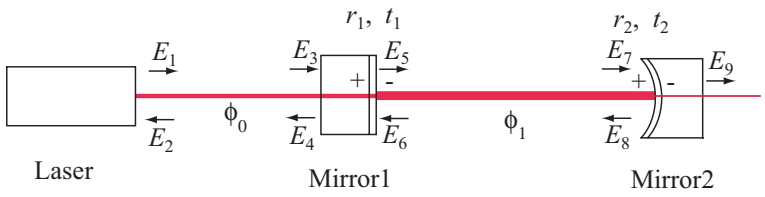

Figure B.1: Example configuration for a simulation tool in order to explain the principle.

$$E_3 = E_1 e^{-i\phi_0} \tag{B.3}$$

$$E_6 = E_8 e^{-i\phi_1} \tag{B.4}$$

The source amplitude E_{input} is set by the user.

$$E_1 = E_{\text{input}} \tag{B.5}$$

When all the fields and their connections are specified, a matrix M can be built into a matrix equation as

$$M \begin{pmatrix} E_1 \\ E_2 \\ \vdots \\ E_9 \end{pmatrix} = \begin{pmatrix} E_{\text{input}} \\ 0 \\ \vdots \\ 0 \end{pmatrix} \tag{B.6}$$

Given a user-defined input spectrum of carrier and RF sidebands, the tool solves this equation for the field amplitudes E_{1-9} of each of the input spectrum components.

The tool then simulates mirror motion via the model in Eq. (4.172) by "injecting" audio sidebands at the mirror chosen by the user to be shaken. It is assumed that this motion is much smaller than the wavelength of the light. These audio sidebands are taken to be new "sources" of light for the equations defined by the M matrix. The propagation of these audio sidebands to a specified location in the interferometer is then solved for by including the frequency dependence in the propagation phases of Eq. (B.3),(B.4). The tool solves this audio sideband equation for a user specified number of points in a frequency range also specified by the user. At each frequency point, the model in Eq. (4.175) is used to calculate the value of the transfer function at that frequency.

B.2 Twiddle

Twiddle is a Mathematica program which was originally written by Martin Regehr in order to calculate the frequency response of an interferometer to mirror motions [23].

The twiddle program was written to analyze the transfer functions between motion of optical components and output voltages, in interferometers illuminated with light which is in general made up of a carrier and one or more sets of sidebands. The output voltages are assumed to be derived by sinusoidal demodulation at specified frequencies of the light intensity at the optical outputs of the interferometer, and the motions of the optical components are assumed to occur at frequencies small compared to the modulation frequency. It is assumed throughout that only a single transverse mode of the light is present. The program analyzes only motion along the beam axis.

Twiddle consists of four Mathematica packages: twiddle.m and four subroutines called by Twiddle: operations.m, components.m, and an ifo.m notebook. The ifo notebook is to be built by the user, whereas the former two are transparent to the user. ifo contains a list of commands interpreted by twiddle as specifying the types and locations of optical components in the interferometer.

During a normal session with the program, the user will first construct or modify a notebook containing the specifications of the interferometer. This is the ifo notebook. The specifications consist of information about the reflectivity, transmission, and the relative spacing of the optical components, as well as information regarding the conditioning of the input light. In another working notebook, twiddle is run, which sets up the static interferometer. At this point, any errors in the setup of the interferometer are reported. Next the user will specify information such as frequency range, resolution, which mirrors to shake, and at which places in the interferometer the transfer function is to be measured.

Finally the transfer functions are generated, and either displayed as plots or written to files.

The version developed by Regehr is very robust, and makes very few assumptions about the interferometer in calculating the transfer function. The current state of the model has been updated, and many new features have been added by James Mason, Hiro Yamamoto, and myself. Some of the new features include support for arbitrary sets of RF sidebands, calculation of the DC matrix of discriminants, and signal

sweeps, in which a mirror is swept linearly through some arbitrary displacement, rather than dithered back and forth by a small amount.

Sample list of our experiment for twiddle .ifo file

```
loss = 10. 10^-6 0

cT0 = .5;
cT1 =0.4;
cT2 = .005;
cT3 = 10. 10^-6;
cT4 = .005;
cT5 = 10. 10^-6;;
cT6 = 1;

other[cT_] = 1. - loss - cT;
cR0 = other[cT0];
cR1 = other[cT1];
cR2 = other[cT2];
cR3 = other[cT3];
cR4 = other[cT4];
cR5 = other[cT5];
cR6 = other[cT6];

r0 = Sqrt[cR0];
r1 = Sqrt[cR1];
r2 = Sqrt[cR2];
r3 = Sqrt[cR3];
r4 = Sqrt[cR4];
r5 = Sqrt[cR5];
r6 = Sqrt[cR6];
t0 = Sqrt[cT0];
t1 = Sqrt[cT1];
t2 = Sqrt[cT2];
t3 = Sqrt[cT3];
t4 = Sqrt[cT4];
t5 = Sqrt[cT5];
t6 = Sqrt[cT6];

gamma = 0.8;
rf1 = 17.25 10^6;
rf2 = 2 rf1;
rf3 = 3 rf1;
rf4 = 4 rf1;

l0=8.6896364637681156‘/2;
l1=0.25;
asy=1.44827274396135274‘ 2;
la=4;

detu=Exp[I 0.01 0Pi];
```

```
leng1=l0-l1-asy/2;
leng2=l1;
leng3=la;
leng4=l1+asy;
leng5=la;
leng6=2 l0;

modfreq = {-rf3,-rf2,-rf1,0,rf1,rf2,rf3};
props = Transpose[{
{1.,1.,1.,1.,1.,1.,1.},
{ 0,0,0,I,0,0,0},
{ 0,0,0,-I,0,0,0},
{ 0,0,0,I,0,0,0},
{ 0,0,0,-I,0,0,0},
{ 0,0,0, I,0,0,0},
{ 0,0,0, detu,0,0,0},
{1.,1.,1.,1.,1.,1.,1.}}]

s1 = source[gamma];
m1= mirror[r1,t1];
bs1 = beamspl[r0,t0];
m2 = mirror[r2,t2];
m3 = endmirror[r3,t3];
m4 = mirror[r4,t4];
m5 = endmirror[r5,t5];
m6 = mirror[r6,t6];
bb1 = endmirror[0.,0.];

c0=connect[s1,1,m1,1,0.];
c1=connect[m1,2,bs1,1,leng1,modfreq];
c2=connect[bs1,2,m2,1,leng2,modfreq];
c3=connect[m2,2,m3,1,leng3,modfreq];
c4=connect[bs1,3,m4,1,leng4,modfreq];
c5=connect[m4,2,m5,1,leng5,modfreq];
c6=connect[bs1,4,m6,1,leng6,modfreq];
c7=connect[m6,2,bb1,1,0.];
```

B.3 Finesse

FINESSE is a simple simulation program written by A. Freise in C language [53]. It calculates light amplitudes in a user specified interferometer configuration. It can generate a number of output signals for various photo detector types. The typical output is a plot of a detector signal as a function of a number of parameters of the interferometer (e.g. arm length, mirror reflectivity, modulation frequency, . . .). The calculations are done in the frequency domain (i.e. a steady state is assumed). When the program is called, FINESSE performs the following steps:

(a) reading a text input file which describes the interferometer and the computation task

(b) generating the set of linear equations which describes the coupling of the light amplitudes

(c) solving numerically the linear equation system for each data point

(d) writing the data into an output file

(e) writing a Gnuplot batch file and starting Gnuplot to plot the data to the specified terminal (windows, X11, postscript,...)

To simulate a certain interferometer configuration, the user has to write an input text file which describes the interferometer in the form of components and connecting nodes. Furthermore, an x-axis has to be specified, i.e. which parameters are to be tuned. When starting the program this input file is read. The specifications of the interferometer (given as components, nodes, and parameters) are stored in a linear set of equations, i.e. a matrix. Then, with respect to the commands given in the input file the calculation is initialised. Finally for each data point the set of linear equations is solved , the specified output signal computed and when the given number of points has been done the data is stored in a text file (extension ‘ .out ’). Additionally another file is created (extension ’.gnu ’) which serves as a batch file for Gnuplot.

Sample list of our experiment for the FINESSE .kat file

```
#-----------------------------------------------------------------
#                          ns4
#                          --
#                          ns3
#                          ss2
#                          ns2
#                          --
#                          ns1
#                          ss1
#                          nb2
# n0 EOM n1 | n2 spr  nb1 / nb3 sp1 np1 | np2 sp2 np3 | np4
#                          nb4
#                          sse
#                          nse1
#                          --
```

```
#                          nse2
#-------------------------------------------------------------------

m mpf 0.995 0.005 0 np1 np2
m msf 0.995 0.005 90 ns1 ns2
m mpe 0.9999 0.0001 0 np3 np4
m mse 0.9998 0.0001 90 ns3 dump

## PR
#m mpr 0.6 0.4 0 n1 n2
m mpr 0 1 0 n1 n2
## SR
#m msem 0.6 0.4 0 nse1 nse2
## RSE
m msem 0.6 0.4 90 nse1 nse2

bs bs1 0.5 0.5 0 45 nb1 nb2 nb3 nb4
l i1 0.3 0 n0
mod eo1 17.25M 0.6 3 pm n0 n1

## detuning needed mkat
#run1:m msem 0.6 0.4 0 nse1 nse2
#run2:m msem 0.6 0.4 10 nse1 nse2
#run3:m msem 0.6 0.4 20 nse1 nse2
#run4:m msem 0.6 0.4 30 nse1 nse2
#run5:m msem 0.6 0.4 40 nse1 nse2
#run6:m msem 0.6 0.4 50 nse1 nse2
#run7:m msem 0.6 0.4 60 nse1 nse2
#run8:m msem 0.6 0.4 70 nse1 nse2
#run9:m msem 0.6 0.4 80 nse1 nse2
#run10:m msem 0.6 0.4 90 nse1 nse2

## 3rd sb is dark @ dark port L- min
s sp1 3.04655 nb3 np1
s sp2 4 np2 np3
s ss1 0.15 nb2 ns1
s ss2 4 ns2 ns3
s spr 7.091365 n2 nb1
#s sse 1.05 nb4 nse1
s ssel 0 nb4 nbl2
s sse 7.091365 nbl4 nse1

## motion of L+
#fsig sig1 mpe 10 0
#fsig sig1 mse 10 0

## motion of L-
fsig sig1 mpe 10 0
fsig sig1 mse 10 180

## motion of l+
#fsig sig3 mpe 10 0
#fsig sig3 mse 10 0
```

```
#fsig sig3 mpf 10 0
#fsig sig3 msf 10 0

## motion of l-
#fsig sig4 mpe 10 0
#fsig sig4 mse 10 180
#fsig sig4 mpf 10 0
#fsig sig4 msf 10 180

## motion of l+
#fsig sig1 mpr 10 0

## motion of ls
#fsig sig1 msem 10 0

## amplitude at d port
#ad adsem3 -51.75M nse2
#ad adsem2 -34.5M nse2
#ad adsem1 -17.25M nse2
#ad adse0 0 nse2
#ad adse1 17.25M nse2
#ad adse2 34.5M nse2
#ad adse3 51.75M nse2

## amplitude at b port
#ad adsem3 -51.75M nb1
#ad adsem2 -34.5M nb1
#ad adsem1 -17.25M nb1
#ad adse0 0 nb1
#ad adse1b 17.25M nb1
#ad adse2b 34.5M nb1
#ad adse3b 51.75M nb1

## RF photo detector
#pd1 pdri 17.25M 0 n1
#pd1 pdr3i 51.75M 0 n1
#pd1 pddi 17.25M 0 nse2
#pd1 pddq 17.25M 90 nse2
#pd1 pdd3i 51.75M 175 nse2

## ********RF photo detector
#pd2 pdri 17.25M 0 10 0 n1
#pd2 pdr3i 51.75M 75.5 10 0 n1
#pd2 pddq 17.25M 75 10 0 nse2
#pd2 pdd3 51.75M 175 10 0 nse2
#pd2 pddi 17.25M 165.5 10 0 nse2

## freqency response
#xaxis sig1 f log 100 100k 400
#xparam pddq f2 1 0

## tuning L+
#xaxis mpe phi lin -1 1 400
```

```
#xparam mse phi 1 90

## tuning L-
#xaxis mpe phi lin -1 1 1000
#xparam mse phi -1 90

## assymmetry dark
#xaxis sp1 L lin 2.9 3.1 50
#xparam ss1 L -1 3.19655
#x2axis sse L lin 6 8 50

## tuning l-
#xaxis mpf phi lin -90 90 1000
#xparam msf phi -1 90
#xparam mpe phi 1 0
#xparam mse phi -1 90

## tuning r of mpr
#xaxis mpr R lin 0.99 0.999 400

## tuning length of power recycling cavity
## macro
#xaxis spr L lin 0 20 50
## micro
#xaxis mpr phi lin -90 90 400

## tuning ls
## macro
#xaxis sse L lin 0 10 500
## micro
#xaxis msem phi lin 0 180 500

## tuning length of l+
## micro
#xaxis mpf phi lin -90 90 400
#xparam msf phi 1 0
#xparam mpr phi 1 0

## tuning modulation freqency
#xaxis eo1 f lin 16M 19M 50
#xparam adse1 f 1 0

yaxis lin abs
gnuterm windows
```

Appendix C

Electronic circuits

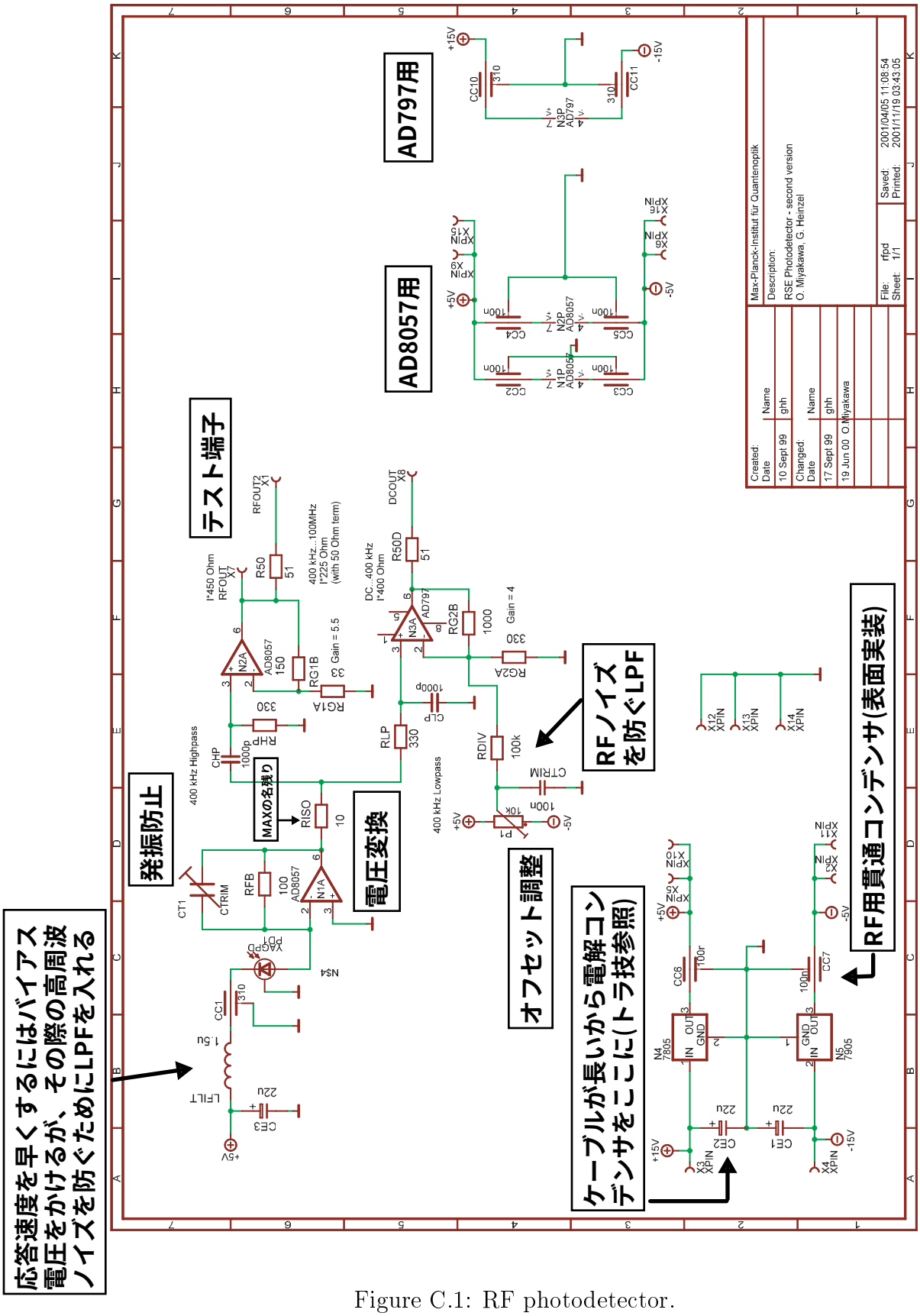

Figure C.1: RF photodetector.

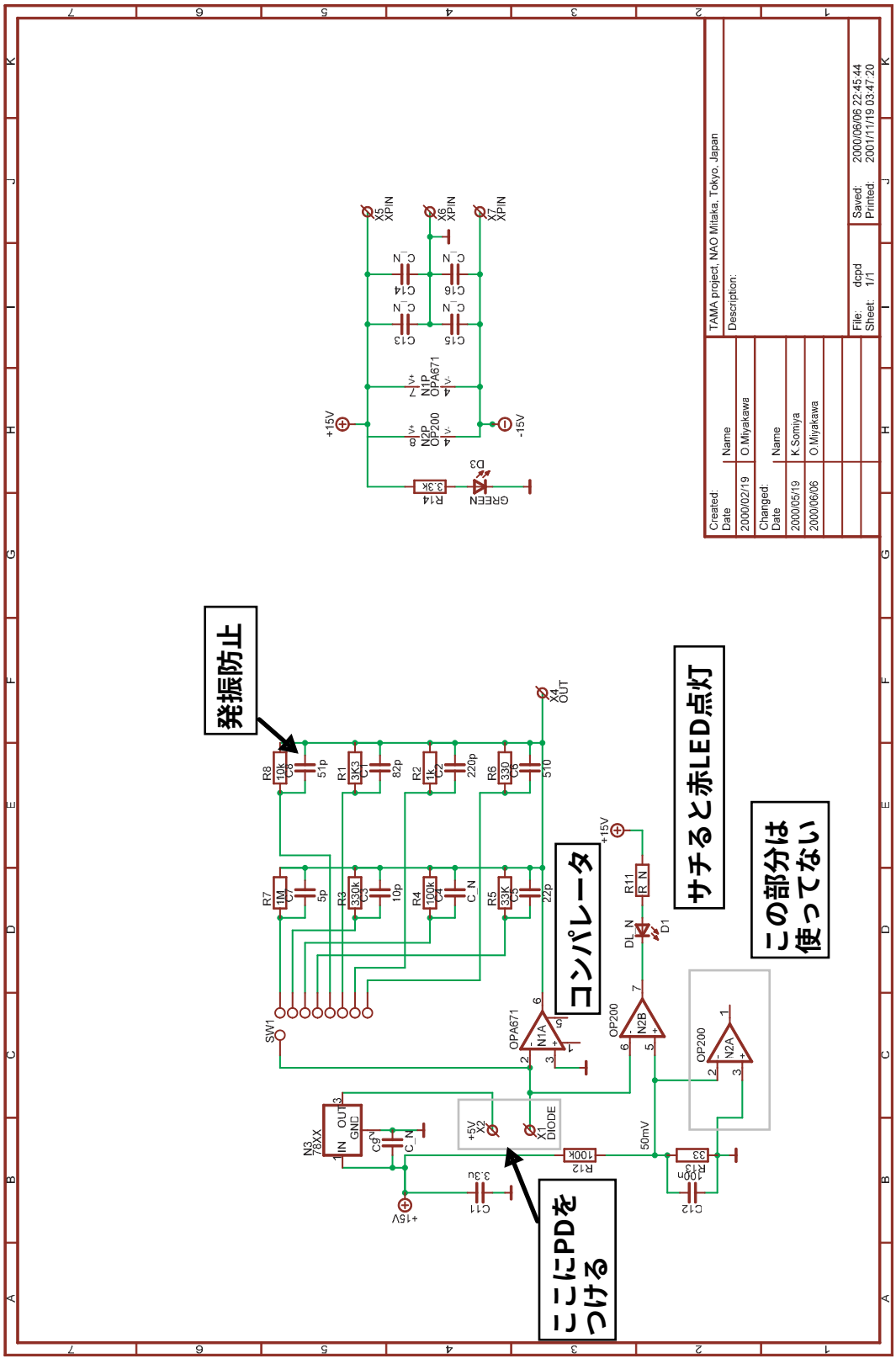

Figure C.2: DC photodetector.

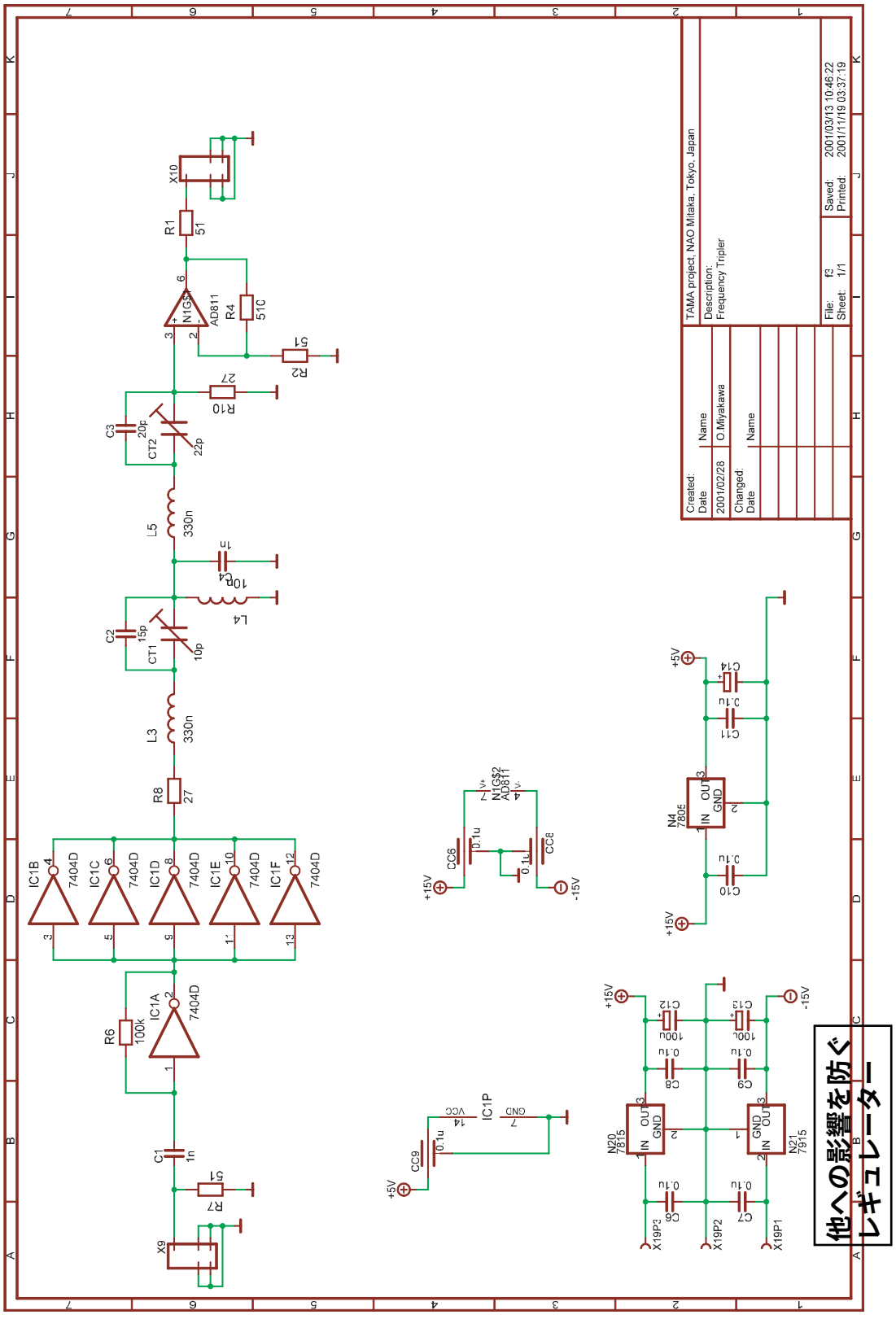

Figure C.3: Frequency tripler.

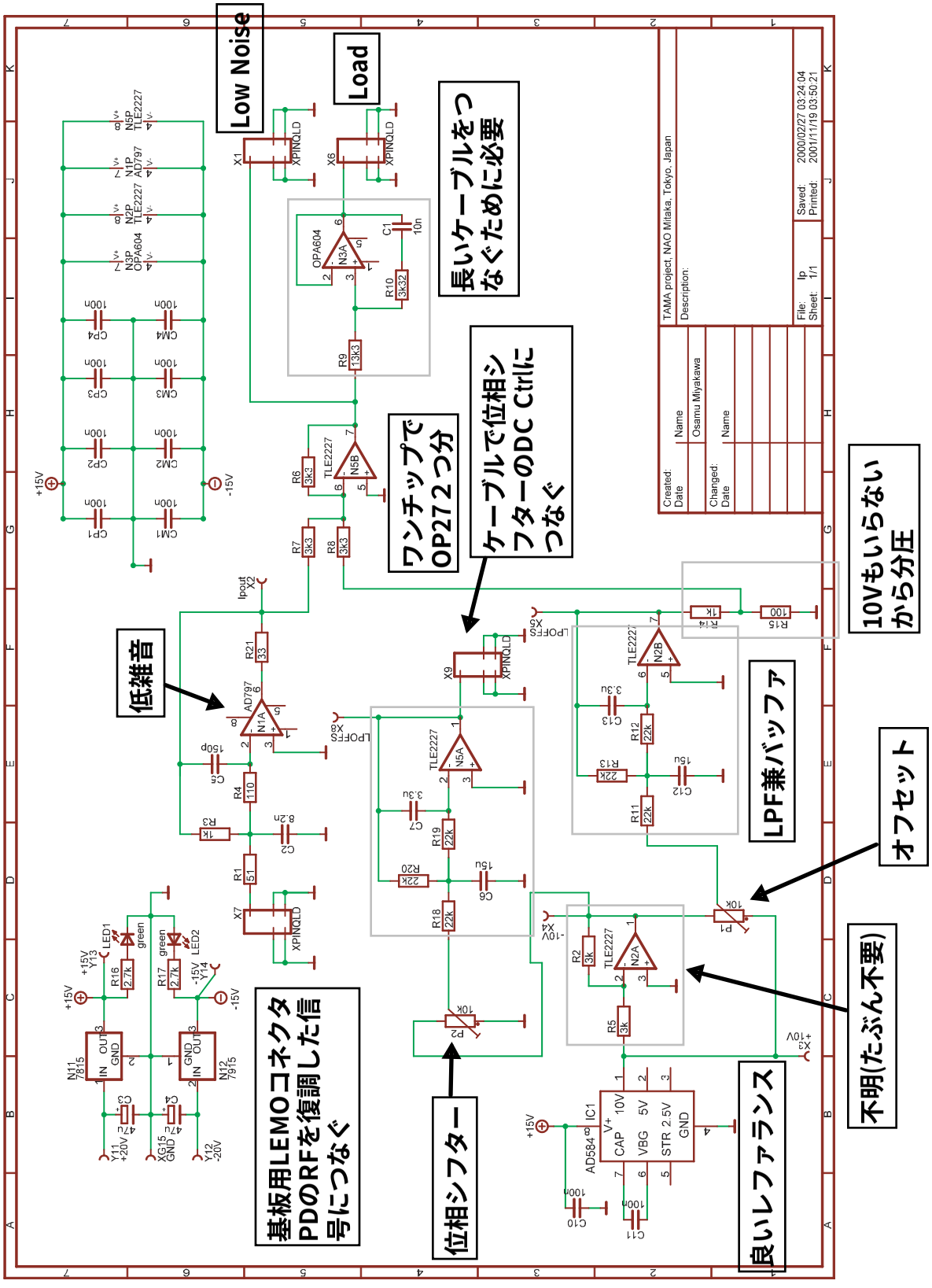

Figure C.4: Low-pass filter for the demodulator and controler of the phase-shifter.

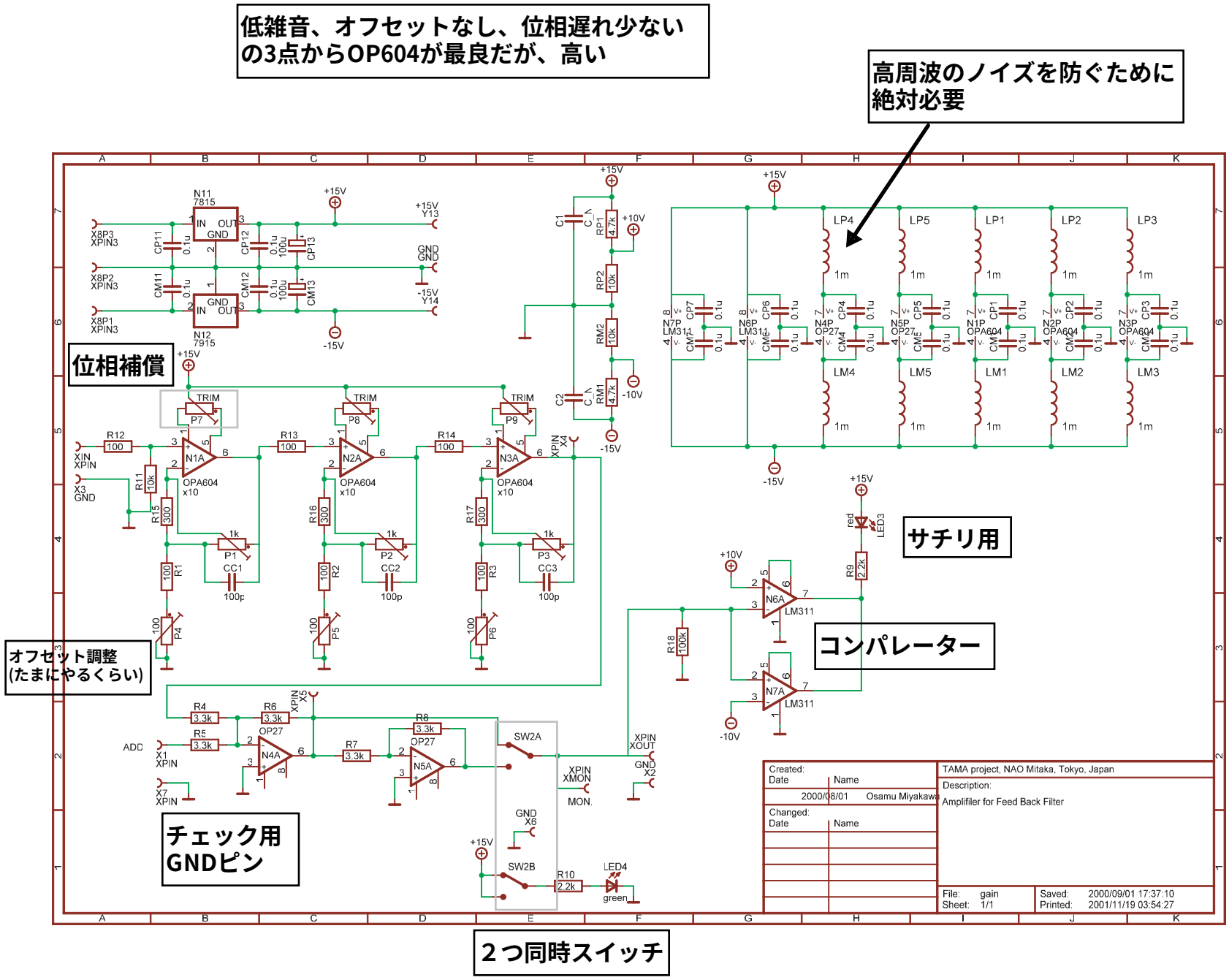

Figure C.5: DC amplifier for the feed-back filter.

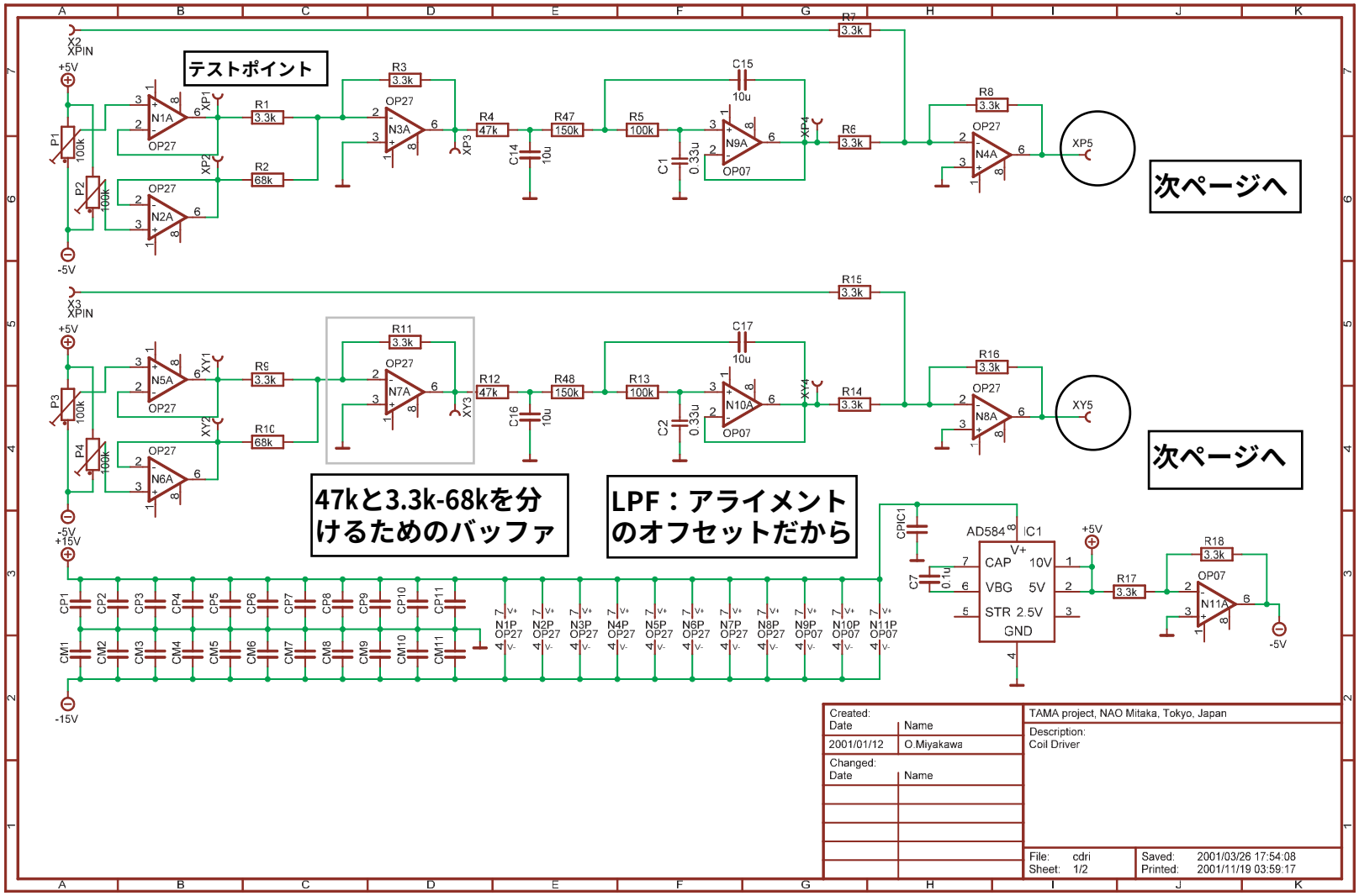

Figure C.6: Coil-driver.

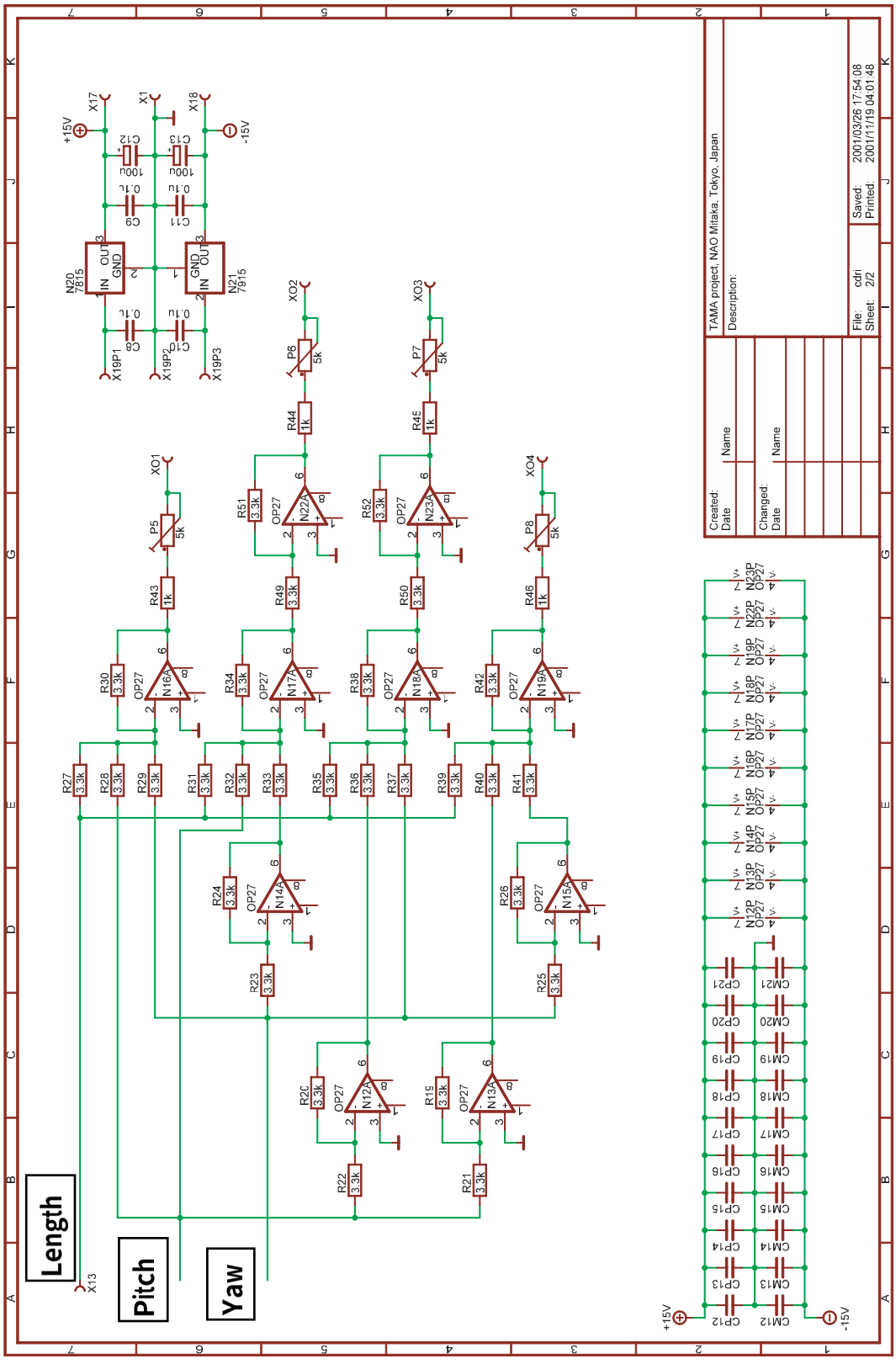

Figure C.7: Coil-driver.

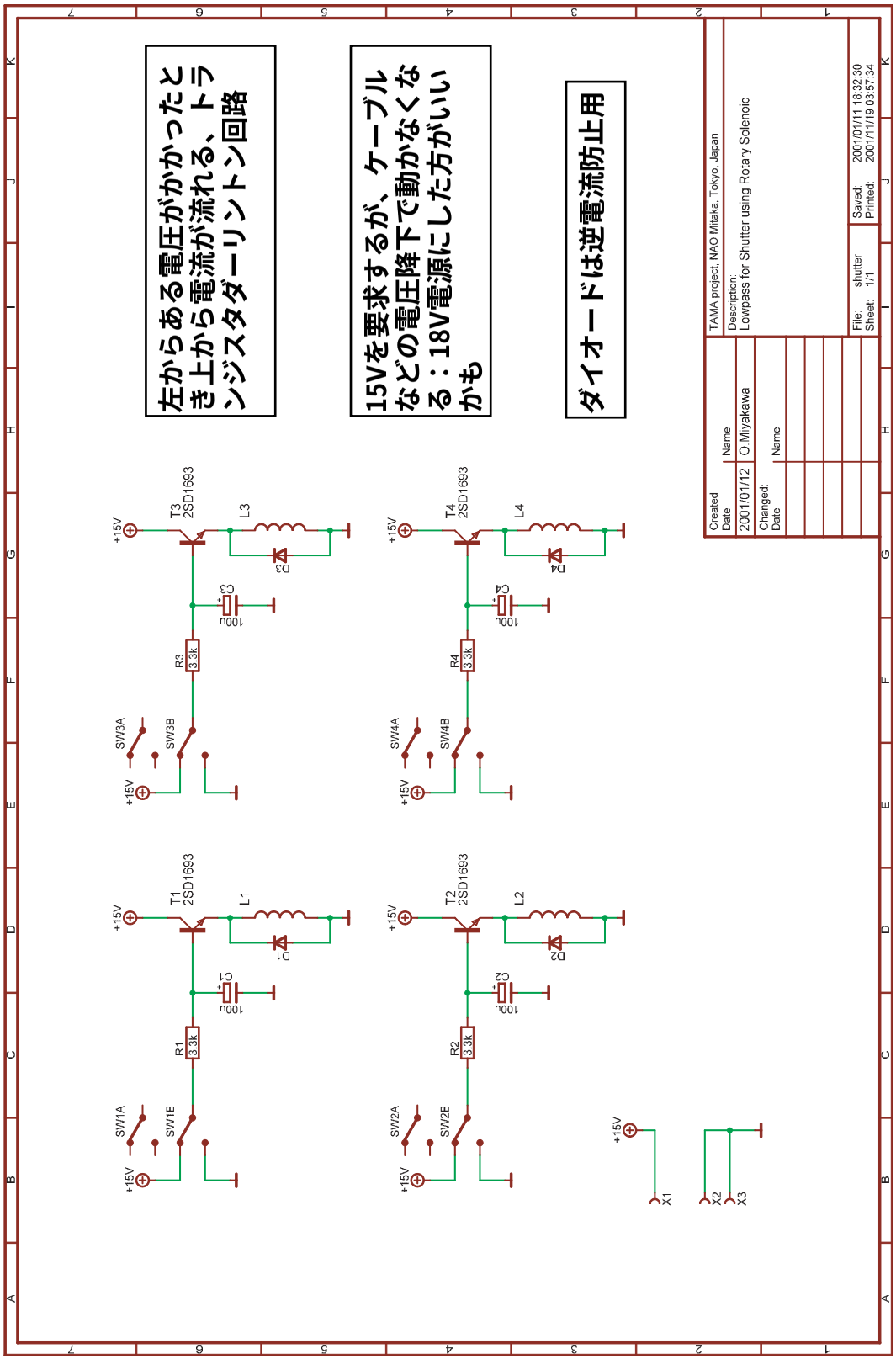

Figure C.8: Shutter for the light pass

Bibliography

[1] A. Einstein, Ann. Phys. Lpz 49, 769 (1916).

[2] A. Einstein, Preuss. Akad. Wiss. Berlin, 688 (1916)

[3] C. W. Misner, K. S. Thorne, and J. A. Wheeler, *Gravitation*, W. H. Freeman and Company (1973)

[4] K. S. Thorne, *Gravitational radiation*, in: *Three hundred years of gravitation* p. 330-458, eds: S. Hawking and W. Israel, Cambridge University Press (1985)

[5] R. A. Hulse and J. H. Taylor, Astrophysical Journal 195 (1975) L51.

[6] J. H. Taylor and J. M. Weisberg. Astrophysical Journal 345 (1989) 434.

[7] J . H. Taylor, *Testing relativistic gravity with binary and millisecond pulsars* in: *General relativity and gravitation* p. 287-294, eds: R. J. Gleiser, C. N. Kozameh, and O. M. Moreschi, Institute of Physics (1993).

[8] A. Abramovici, W. E. Althouse, R. W. P. Drever, Y. Gürsel, S. Kawamura, F. J. Raab; D. Shoemaker, L. Sievers, R. E. Spero, K. S. Thorne, R. E. Vogt, R. Weiss, S. E. Whitcomb and M. E. Zucker, Science 256 (1992) 325.

[9] The VIRGO collaboration, VIRGO Final Design Report (1997).

[10] K. Danzmann, H. Lück, A. Rüdiger, R. Schilling, M. Schrempel, W. Win-kler, J. Hough, G. P. Newton, N. A. Robertson, H. Ward, A. M. Campbell, J. E. Logan, D. I. Robertson, K. A. Strain, J. R. J. Bennett, V. Kose, M. Kühne, B. F. Schutz, D. Nicholson, J. Shuttleworth, H. Welling, P. Aufmuth, R. Rinkleff, A. Tünnermann and B. Willke, Proposal for a 600m Laser-Interferometric Gravitational Wave Antenna, Max-Planck-Institut für Quantenoptik Report 190, Garching (Germany) (1994).

[11] K. Tsubono, 300-m Laser Interferometer Gravitational Wave Detector (TAMA300) in Japan, in: *Gravitational Wave Experiments* p. 112-114, eds: E. Coccia, G. Pizzella, and F. Ronga, World Scientific (1995).

[12] M. Ando *et al*, Physical Review Letters, 86 (2001) 3950.

[13] M.E. Gertsenshtein and V.I. Pustovoit. *On the detection of low-frequency gravitational waves*. Soviet Physics - JETP, 16:433, 1963.

[14] G. E. Moss, L. R. Miller, and R. L. Forward, *Photon-noise-limited laser transducer for gravitational antenna*. Applied Optics 10 (1971) 2495.

[15] R. Weiss, *Electromagnetically coupled broadband gravitational antenna*, Quarterly Progress Report of the Research Laboratory of Electronics of the Massachusetts Institute of Technology 105 (1972) 54.

[16] D. Herriott, H. Kogelnik, and R. Kompfner, Applied Optics 3 (1964) p.523.

[17] D. R. Herriott and H. J. Schulte, Applied Optics 4 (1965) 883.

[18] D. Shoemaker, R. Schilling, L. Schnupp, W. Winkler, K. Maischberger, and A. Rüdiger, Phys. Rev. D38 (1988) 423.

[19] R. W. P. Drever, J. Hough, A.J. Munley, S. -A. Lee, R. Spero, S. E. Whitcomb, H. Ward, G. M. Ford, M. Hereld, N. A. Robertson, I. Kerr, J. R. Pugh, G. P. Newton, B. Meers, E. D. Brook III, and Y. Gürsel, in *Quantum Optics, Experimental Gravitation, and Measurement Theory*, eds: P. Meystre and M. O. Scully (Plenum Press, New York, 1983) 503.

[20] R. W. P. Drever, in *Gravitational Radiation*, eds: N. Deruelle and T. Piran (North-Holland, Amsterdam, 1983) 321.

[21] R. Schilling, L. Schnupp, W. Winkler, K. Maischberger, and A. Rüdiger, J. Phys. E: Sci. Instrum. 14 (1981) 65.

[22] P. Fritschel, D. Shoemaker and R. Weiss, Applied Optics 31 (1992) 1412.

[23] M. W. Regehr, *Signal Extraction and Control for an Interferometric Gravitational Wave Detector*, Ph. D thesis, California Institute of Technology (1995).

[24] M. W. Regehr, F. J. Raab and S. E. Whitcomb, Optics Letters 20 (1995) 1507.

[25] J. A. Giaime, *Studies of Laser Interferometer Design and a Vibration Isolation System for Interferometric Gravitational Wave Detectors*, Ph. D thesis, Massachusetts Institute of Technology (1995).

[26] D. Sigg, N. Mavalvala, J. Giaime, P. Fritschel, and D Shoemaker Applied Optics 37 (1998) 5687.

[27] M. Ando, *Power recycling for an interferometric gravitational wave detector*, Ph. D thesis, Tokyo University (1998).

[28] M. Ando, K. Kawabe and K. Tsubono, Physics Letters A 237 (1997) 13.

[29] S. Sato, Ph. D thesis, The Graduate University for Advanced Studies (1998)

[30] B.J. Meers, Phys. Rev. D38 (1986) 2317.

[31] J. Mizuno, K. Strain, P.G. Nelson, J.M. Chen, R. Schilling, A. Rdiger, W. Winkler, K. Danzmann: *Resonant sideband extraction: A new configuration for interferometric gravitational wave detectors*, Physics Letters A 175 (1993) 273.

[32] J. Mizuno: *Comparison of optical configurations for laser interferometric gravitational wave detectors*, Ph.D. Thesis, University of Hannover, 1995. Also available as MPQ Report 203 (July 1995).

[33] W. Winkler, K. Danzmann, A. Rüdiger, and R. Schilling, Phys. Rev. A44 (1991) 7022.

[34] P. Hello and J.-Y. Vinet, Phys. Lett. A178 (1993) 351.

[35] K. A. Strain, K. Danzmann, J. Mizuno, P. G. Nelson, A. Rüdiger, R. Schilling, and W. Winkler, Phys. Lett. A194 (1994) 124.

[36] G. Heinzel, J. Mizuno, R. Schilling, W. Winkler, A. Rüdiger, K. Danzmann: *An experimental demonstration of resonant sideband extraction for laser-interferometric gravitational wave detectors*, Phys. Lett. A 217 (1996) 305.

[37] J. E. Mason: Ph.D. Thesis, California Institute of Technology, 2001

[38] D. Shaddock: Ph.D. Thesis, Australian National University, 2001.

[39] K. Kuroda *et al.*, Int. J. Mod. Phys. D 8 (1999) 557.

[40] LIGO II Conceptual Project Book, LIGO M990208-A-M (1999).

[41] T. Nakamura, in: *Detection of gravitational waves* (in Japanese), p. 1-166, eds: T. Nakamura, N. Mio, M. Ohashi, Kyoto University Academy Press (1998).

[42] J. Weber, Physical Review 117 (1960) 306.

[43] J. Weber, Physical Review Letters 22 (1969) 1320.

[44] P. Astone, M. Bassan, P. Bonifazi, P.Carelli, M. G. Castellano, G. Cavallari, E. Coccia, C. Cosmelli, V. Fafone, S. Frasca, E. Majorana, I. Modena, G. V. Pallottino, G. Pizzella, P. Rapagnani, F. Ricci, and M. Visco, Physical Review D 47 (1993) 362.

[45] E. Mauceli, Z. K. Geng, W. O. Hamilton, W. W. Johnson, S. Merkowitz, A. Morse, B. Price, and N. Solomonson, Physical Review D 54 (1996) 1264.

[46] M. Cerdonio, L. Franceschini, G. Fontana, R. Mezzena, S. Paoli, G. A. Prodi, S. Vitale, J. P. Zendri, M. Biasotto, M. Lollo, F. Bronzini, R. Macchietto, G. Maron, A. Ortolan, M. Strollo, G. Vedovato, M. Bonaldi, P. Falferi, E. Cavallini, P. L. Fortini, E. Montanari, L. Taffarello, A. Colombo, D. Pas- coli, B. Tiveron, in: *Gravitational Wave Experiments* p. 176-194, eds: E. Coccia, G. Pizzella, and F. Ronga, World Scientific (1995).

[47] P. Astone, M. Bassan. P. Bonifazi, F. Bronzini, M. G. Castellano, E. Coccia, C. Cosmelli, V. Fafone, S. Frasca, E. Majorana, I. Modena, G. V. Pallottino, G. Pizzella, P. Rapagnani, F. Ricci, and M. Visco, Europhysics Letters 16 (1991) 231.

[48] G. Frossati *et al. A Gravitational Radiation Antenna in The Netherlands* (1995).

[49] W. W. Johnson and S. M. Merkowitz, Physical Review Letters 70 (1993) 2367.

[50] S. M. Merkowitz and W. W. Johnson, Physical Review D 53 (1996) 5377.

[51] P. Bender, A. Brillet, I. Ciufolini, A. M. Cruise, C. Cutler, K. Danzmann, F. Fidecaro, W. M. Folkner, J. Hough, P. McNamara, M. Peterseim, D. Robertson, M. Rodrigues, A. Rüdiger, M. Sandford, G. Schafer, R. Schilling, B. Schutz, C. Speake, R. T. Stebbins, T. Sumner, P. Touboul, J.-Y. Vinet, S. Vitale, H. Ward, W. Winkler, *LISA Pre-Phase A Report Second Edition*, (1998).

[52] K. Arai, M. Ando, S. Moriwaki, K. Kawabe, K. Tsubono, Physics Letters A 273 (2000) 15.

[53] A. Freise, :*Frequency domain INterferomEter Simulation SoftwarE*, MPQ Hannover, 2000

Acknowledgement

I feel very fortunate to have been able to do my graduate studies at the NAO. I would especially like to thank the following people (more or less in chronological order, and far from complete): Prof. Kawamura for introducing me to the subject and for his continuous support, and for being the best adviser. G. Heinzel for teaching me many of the things presented in this work. K. Somiya discussing interesting idea with me. Prof. Kuroda as my boss for permitting me to do my work at the NAO and Prof Fujimoto for receiving me. I would like to thank K. Arai, R. Takahashi, D. Tatsumi, P, Beyersdorf, M. Ando for very useful discussion. P, Beyersdrf also helped correcting many mistakes of English of this thesis. I appreciated T. Yamazaki, M. Fukushima, and secretaries for their support.

This work is a combination and contribution of many people. I thank again all of support members and my families.